

INVESTIGATION OF SHOCK PRESSURES IN HIGH
CURRENT SPARK GAP ELECTRODES

by

MICHELE WOFFORD, B.S.E.E., M.S.E.E.

A DISSERTATION

IN

ELECTRICAL ENGINEERING

Submitted to the Graduate Faculty
of Texas Tech University in
Partial Fulfillment of
the Requirements for
the Degree of

DOCTOR OF PHILOSOPHY

Approved

-

-

-

-

-

/

-

August, 1995

001
T3
1995
No. 102
cop. 2

FET
0572

ACKNOWLEDGMENTS

I would like to thank my committee members, Dr. Baker, Dr. Kristiansen, Dr. Hatfield, Dr. Giesselmann, and Tom Naff, for their advice and support. I would especially like to thank Tom Naff at Physics International for providing financial support and experimental supplies. I cannot thank Dr. Baker enough for offering me the Department of Education fellowship, which kept me in graduate school. I owe Dr. Greg Engel a debt of gratitude for always taking the time to help me, especially in the laboratory. I appreciate all of the help of the Pulsed Power staff, which includes Lonnie Stephenson, John Bridges, Kim Zinsmeyer, Donna Srader, and Marie Byrd, whom I will miss dearly. Although they have graduated, I want to thank Gordon Masten and Frank Hegeler, not only for being my officemates and colleagues, but also my friends. I aspire to have Gordon's patience and Frank's ability to do anything "in five minutes." Last but not least, I would like to thank my husband, Rick Caldwell, for his support and sense of humor during the entire summer that I spent at the lab finishing this work.

TABLE OF CONTENTS

ACKNOWLEDGEMENTS	ii
ABSTRACT	iv
LIST OF TABLES	v
LIST OF FIGURES	vi
CHAPTER	
1. INTRODUCTION.....	1
2. BACKGROUND AND THEORY	3
2.1 High Power Switch Pressures	3
2.2 Impulse Loading of Materials.....	9
2.3 Propagation of an Impulse Through a Material.....	11
2.4 Fracture Mechanisms	18
2.5 Hypotheses of Electrode Failure.....	18
3. EXPERIMENTAL SETUP AND DATA MEASUREMENT	20
3.1 Experimental Circuit	20
3.2 Electrical Diagnostics.....	22
3.3 Pressure Diagnostics	23
3.4 Data Acquisition	28
3.5 Data Interpretation	28
3.6 Experimental Measurements	32
4. ANALYSIS AND THEORETICAL MODELING.....	58
4.1 Analysis of Switch Pressures.....	58
4.2 Stress Wave Propagation in the Electrodes	62
4.3 PSPICE Analysis of Acoustic Transmission Lines	69
5. CONCLUSIONS.....	73
REFERENCES.....	77
APPENDIX.....	80

ABSTRACT

Generally, the limiting component in a pulsed power system is the switch. This is due to the fact at some point, the switch transfers all of the energy in the system. High voltage and current create a rough environment for switch electrodes and insulators. In previous studies of switch reliability and lifetime, electrode erosion has received much attention. This investigation deals with the mechanisms behind electrode fracture, which presents an immediate problem, rather than erosion, which has long-term effects on switch performance.

The switches under study are spark gaps with graphite electrodes. The spark gap closes when an electric arc forms between the electrodes, and current conduction begins. Strong mechanical forces are generated as the arc forms and impact the electrodes. The purpose of this research is to determine the dominant pressure mechanism of electrode fracture, and the propagation of the pressure wavefront through the electrode.

Energy is stored in a 5 kJ, 60 kV capacitor, and shorted through the spark gap. This is done to duplicate prior experimental work at Physics International Company. Operating parameters, such as gap spacing, air pressure, charging voltage, inductance, and magnetic pulse shaping, are varied, and mechanical pressure is measured using a strain gage mounted on a ceramic bar. Experimental data from the strain gage is compared to theoretical modeling done in Mathcad and PSPICE.

LIST OF TABLES

2.1	Dual Electrical and Acoustical Properties	14
2.2	Mechanical and Acoustical Properties of Kidney Stone Composites and ACF-10Q Graphite	17
3.1	Mechanical Characteristics of Delay Line Material.....	27
3.2	Summary of Gap Spacings versus Operating Parameters.....	33
3.3	Variations in Operating Parameters	33
3.4	Maximum Shock Amplitude versus Increasing Breakdown Voltage and Input Energy.....	37
3.5	Maximum Shock Amplitude versus Constant Breakdown Voltage and Input Energy.....	40
3.6	Maximum Shock Amplitude versus Increasing Energy and Increasing Air Pressure.....	43
3.7	Estimated Time Delays versus Measured Time Delays.....	52
4.1	Peak Shock Pressure versus Charging Voltage	62
4.2	List of Variables in Figures 4.6 and 4.7.....	65

LIST OF FIGURES

2.1	Stress-Strain Curve for Aluminum.....	10
2.2	Incident, Reflected, and Refracted Waves Between Two Media.....	12
3.1	Modified MJB Switch	21
3.2	Integrator for B-Dot Probe	23
3.3	Wheatstone Bridge.....	25
3.4	Pressure Measurement Setup.....	27
3.5	Strain Gage Measurements with a Time Base of (a) 10 ms/div, (b) 50 ms/div, and (c) 200 ms/div.....	30
3.6	Noise Level of Experiment	31
3.7	Gap Spacing Adjustment	34
3.8	Measured Shock Pressure for Increasing Energy and Gap Spacings of (a) 0.25", (b) 0.3", (c) 0.4", and (d) 0.5".....	35
3.9	Initial Shock Pressures as a Function of Increasing Gap Spacing and Increasing Energy	36
3.10	Measured Shock Pressure for Constant Energy and Gap Spacings of (a) 0.25", (b) 0.3", (c) 0.4", and (d) 0.5".....	38
3.11	Initial Shock Pressures as a Function of Increasing Gap Spacing and Constant Energy	39
3.12	Measured Shock Pressure for Increasing Energy and Air Pressures of (a) 0 psi, (b) 6 psi (c) 10 psi, and (d) 14 psi	41
3.13	Initial Shock Pressures as a Function of Increasing Energy and Increasing Air Pressure	42
3.14	Maximum Output Currents for (a) 69 nH and (b) 92 nH Inductance Circuits	44
3.15	Measured Shock Pressure for Inductances of (a) 69 nH and (b) 92 nH	45

Initial Shock Pressure as a Function of Inductance	46
3.17 Pressure Reflections of Initial Pulses	46
3.18 MJB Switch Modified to Incorporate the Magnetic Delay	48
3.19 B-Dot Measurements (a) without Magnetic Delay and (b) with Magnetic Delay.....	49
3.20 Comparison of Initial B-Dot Measurements for Similar Shots.....	50
3.21 Initial B-Dot Measurements with and without Magnetic Delay for Air Pressures of (a) 0 psi, (b) 6 psi, (c) 10 psi, and (d) 14 psi	50
3.22 Measured Shock Pressure with Magnetic Delay and Air Pressures of (a) 0 psi, (b) 6 psi, (c) 10 psi, and (d) 14 psi.....	52
3.23 Initial Shock Pressure with and without Magnetic Delay with Air Pressures of (a) 0 psi, (b) 6 psi, (c) 10 psi, and (d) 14 psi.....	54
3.24 Measured Shock Pressure for (a) Graphite Electrode and (b) Stainless Steel Electrode	55
3.25 Initial Shock Pressures for Graphite and Stainless Steel.....	56
4.1 $J \times B$ Force at Electrode Tip.....	59
4.2 Maximum Arc Radius	61
4.3 Maximum Arc Expansion Velocity.....	61
4.4 Maximum Shock Pressure.....	61
4.5 Geometry of Spherical Pressure Wave/Spherical Electrode Interaction	63
4.6 Propagation of Spherical Wavefront in Graphite Electrode for Gap Spacings of (a) 0.25", (b) 0.3", (c) 0.4", and (d) 0.5"	65
4.7 Propagation of Spherical Wavefront in Stainless Steel Electrode for Gap Spacing of 0.5"	67
4.8 Geometry of Cylindrical Pressure Wave/Spherical Electrode Interaction.....	68

4.9 Propagation of a Cylindrical Shock Wavefront Through a Graphite Electrode for a Gap Spacing of 0.5"	69
4.10 PSPICE Simulation Circuit.....	70
4.11 PSPICE Simulation of Pressure Input and Strain Gage Output	71
4.12 Comparative Experimental Shot	71

CHAPTER 1

INTRODUCTION

In many state-of-the-art pulsed power machines, the limiting component is the switch. Frequently, the switch requires the most maintenance or replacement after a short time. In large, repetitively operated systems, this quickly becomes a problem. Replacing and repairing switches in a complicated circuit is time consuming and costly. For this reason, electrode erosion has been studied in great detail and has provided much information on the usage of electrode materials and switch configurations. However, this study focuses on a specific case of electrode damage rather than erosion. Although this phenomenon is uncommon, it presents an immediate, debilitating problem when it occurs.

This research focuses almost exclusively on graphite as an electrode material. Graphite is useful for pulsed power applications for the following reasons: it exhibits smooth surface erosion when exposed to an arc; it has a very low erosion rate at high coulomb transfers (above 25 Coulomb); and erosion by-products that degrade switch insulators are minimal [1]. In a related field, it has been experimentally shown that insulator degradation rates in vacuum surface discharge switches increases with the atomic weight of the electrodes. Graphite, a form of carbon, has a low atomic weight compared to other metals such as aluminum, stainless steel, and copper. The disadvantages are a high erosion rate at low Coulomb transfer (below 5 Coulomb) and a relatively high resistivity [2].

An unexpected failure mechanism in graphite electrodes during tests at Physics International Company (PI) prompted this investigation. Graphite is an attractive high-power switch electrode material for PI, mainly because it erodes very smoothly compared to other metals and does not leave a metallic coating on switch insulator materials. For a large, pulsed power system with multiple switches, this means higher reliability and less switch maintenance. However, preliminary tests at PI revealed a fatal flaw. Regardless of the maximum current, if the peak current divided by the quarter time period of a ringing pulse exceeded 350 A/ns just once, the electrode would sustain major spalling damage at the tip. Although not mathematically rigorous, this quantity will be referred to as the current derivative, current rate of rise, or di/dt for simplicity. As the current rate of rise increased, the damage became more pronounced. The failure that occurred for a fast, 100 kA pulse was not present in a slower, 800 kA pulse.

To reproduce the event of electrode failure, a circuit that exceeds the di/dt limit of 350 A/ns is required. To achieve a high rate of current rise, a low system inductance is

necessary. Since di/dt is proportional to circuit voltage and inversely proportional to inductance, increasing the voltage will also improve the di/dt . Taking this into consideration, a compact Marx bank was constructed. The output voltage could be increased with an increase in the number of stages, and the inductance kept to a minimum by the compact structure. The bank had three stages, with a maximum output voltage of 120 kV. The circuit was reconfigured several times to reduce the inductance, and peaking capacitors were added to sharpen the risetime. After all of this, the circuit performance reached the di/dt limit but did not exceed it.

At this point, a decision was made to use a system similar to the one at PI. Using a spark gap from PI's Mega Joule Bank, a low inductance setup was devised. In this way, the current, di/dt , and energy was increased, and the output voltage lowered.

The original intent of the research was to vary operating parameters until the electrodes broke. During the investigation, it was concluded that the failure was not due exclusively to high di/dt . No graphite electrode fracture occurred even under the conditions in which it was expected. However, measurements of the pressure created during the spark gap breakdown phase were taken for various operating parameters. The analysis of the pressure measurements and the subsequent propagation through the electrode in Chapter 3 and the conclusions in Chapter 5 will hopefully give some insight into the dominant failure mechanism.

This dissertation is divided into four main sections. The background and theory of the pressures generated in a high current switch and the subsequent transmission through the electrode is presented in Chapter 2. Chapter 3 is a discussion of the experimental setup, diagnostics, and measurements. The measured data includes comparisons of pressure values versus charging voltage, electrode gap spacing, gas pressure, inductance, electrode material, and the use of magnetic delay. Chapter 4 is divided into three sections. The first section contains a Mathcad analysis of the magnetic and shock pressures generated by a high current arc, which is based on the theory in Chapter 2. The second section includes a Mathcad analysis of the pressure propagation through the electrode tip. The last section is a PSPICE analysis of the signal propagation through the acoustic transmission line that transmits the pressure signal. Chapter 5 concludes with a discussion on the similarities between the models and the measured data, and also the effect of varying the operating parameters on the pressure.

CHAPTER 2

BACKGROUND AND THEORY

Material fracture results when an applied mechanical stress exceeds the strength of the material. The reaction of the material depends on the nature of the stress, whether it is static, dynamic, or impact pressure. When static stress is applied to an object, stress and strain are uniformly distributed throughout the material. If the material fails due to excess loading, the failure propagates through the entire object. When a dynamic load is applied to an object, stress and strain are localized and may not have a chance to distribute. A special case of dynamic pressure is impact or impulse loading, which is marked by an almost instantaneous rise in pressure and is over in several microseconds. In this case, the object may suffer a local deformation that does not have time to propagate before the impulse passes.

A high current arc creates large transient pressures in a spark gap, which impact the electrodes. This chapter will explain the pressures generated in the switch, and the correlation to the operating parameters. The discussion will continue to the effect of impact loading on a material, specifically graphite. Finally, some theories will be presented regarding the cause of the electrode failure.

2.1 High Power Switch Pressures

There are several forces created in a high power switch that result in pressure on the electrode surface. High currents produce a strong $J \times B$ force normal to the surface of the electrode, which acts to compress the electrode. Generation of an arc creates a strong shock wave, whose magnitude and velocity have been correlated to energy and di/dt [3], [4]. As the shock wave diverges, it impacts the electrodes. Separate from the shock wave, a cloud of debris caused by the arc, the plasma jet, follows the shock wave and impinges on the electrodes [5]. Lastly, the high temperatures induced by the shock wave and plasma jet create thermal stresses on the surface of the electrode.

2.1.1 High Magnetic Field Forces

If a point charge is in the vicinity of an electric or magnetic field, there is motion involved. For a current moving in a conductor there is no component of electric field and the differential force is

$$d\vec{F}=dQ(\vec{v}\times\vec{B}), \quad [2.1]$$

where dQ = differential charge element, v = particle velocity, and B = magnetic flux density. Expressed as a volume quantity, the differential charge element may be defined as

$$dQ=\rho dV, \quad [2.2]$$

where ρ = volume charge density and dV = volume element. The current density is defined as

$$\vec{J}=\rho\vec{v}, \quad [2.3]$$

and Equation [2.1] becomes

$$d\vec{F}=dV(\vec{J}\times\vec{B}). \quad [2.4]$$

Integrating Equation [2.4] over a volume, the total force is

$$\vec{F}=\int_{vol}(\vec{J}\times\vec{B})dV. \quad [2.5]$$

Since the arc is transient, it has high frequency characteristics. Because of this, most of the current in the electrodes flow on or near the surface due to the skin effect. The depth of current flow into the material is called the skin depth, and may be calculated from

$$\delta=\frac{1}{\sqrt{f\pi\sigma\mu}}, \quad [2.6]$$

where f = pulse frequency, σ = conductivity, and μ = permeability.

Calculating the magnetic pressure on the surface of the electrode in the vicinity of the arc is not a trivial problem. To simplify calculations, the arc is usually assumed to be cylindrical, with constant parameters. In reality, the arc is time dependent and also does not attach to the surface of the electrode in a perfectly cylindrical manner. In the electrode, the current density is not uniform throughout the skin depth, but decays exponentially. Subsequently, the magnetic field also decays in the electrode until there is no current flow. Also, calculating the magnetic field at the discontinuity between the arc and the electrode is not a trivial problem, especially depending on the geometry of electrode.

Determining the magnetic pressure on the electrode surface in the region of the arc is an almost intractable problem unless it is simplified. By assuming ideal conditions and simplifying the geometry, the magnetic pressure is calculated in Chapter 4.

2.1.2 Shock Pressure

Shock waves are a special case of acoustic waves. Acoustic waves produce compression and rarefaction of a medium as they propagate; however, shock waves are characterized by a discontinuity in density, velocity, and pressure as they travel through a medium. Shock wave mechanics are governed by the following conservation equations of mass, momentum, and energy:

$$\rho_1 u_1 = \rho_0 u_0 \quad [2.7]$$

$$p_1 + \rho_1 u_1^2 = p_0 + \rho_0 u_0^2 \quad [2.8]$$

$$E_1 + \frac{p_1}{\rho_1} + \frac{u_1^2}{2} = E_0 + \frac{p_0}{\rho_0} + \frac{u_0^2}{2} \quad [2.9]$$

Density, velocity, pressure, and internal energy are represented respectively by ρ , u , p , and E . Subscript 1 denotes the area following the shock wave, and subscript 0 denotes the undisturbed region. The density ratio in a gas with a constant specific heat across a very strong shock wave does not increase infinitely, but has a maximum ratio of

$$\frac{\rho_1}{\rho_0} = \frac{\gamma + 1}{\gamma - 1} \quad [2.10]$$

where γ = the ratio of specific heats of gases.

Although the conservation equations hold for all media, shock propagation through solids and liquids is quite different from that in gases. In a gas, pressures of tens to hundreds of atmospheres constitute a strong shock wave. However, to compress a metal, even by a small percentage, requires pressures greater than 10^6 atmospheres.

2.1.3 Arc Induced Shock Parameters

Shock waves may be generated several different ways. They are usually produced by an explosion or by a severe impact of two objects. In this case, they are the result of an arc formation. As the arc column forms between two electrodes, the surrounding air expands very rapidly, creating immense pressure. As the radial distance of the shock exceeds the length, the wave becomes spherical [6, 7].

A theoretical calculation of the arc channel radius as a function of current is presented by Engel, Kristiansen, and Krompholz [4]. Experimentally obtained values of the arc radius due to an oscillating current validate the theoretical calculation. The arc radius calculation is not significantly altered if the conductivity is considered to be constant as opposed to temperature-dependent. The arc expansion velocity and arc pressure may be calculated from the arc radius. The following equations are based on two assumptions. The shock pressure must be much greater than the ambient pressure, and the magnetic pressure must be negligible compared to the shock pressure. The shock wave separates from the expanding plasma channel when the arc expansion velocity falls below the speed of sound in the gas [8].

Assuming the shock front expands with the same velocity as the arc channel, the pressure behind the front is

$$p_1 = K_1 \rho_0 u_1^2, \quad [2.11]$$

where ρ_0 = initial gas density, K_1 = resistance coefficient, and u_1 = expansion velocity of the channel. The resistance coefficient is calculated as

$$K_1 = \frac{2(\gamma + 1)}{(\gamma - 1)^2}. \quad [2.12]$$

The arc radius for an oscillating current is

$$r(t) = \left(\frac{9}{\pi^2 \rho_0 K_1 \sigma} \right)^{\frac{1}{6}} \left[\int_0^t \left(\int_0^{\tau'} i(t)^2 d\Gamma \right)^5 d\Gamma' \right]^{.333}, \quad [2.13]$$

where σ = conductivity, which is accurate into the second period of oscillation. The channel expansion velocity is simply the first derivative of $r(t)$,

$$u_1(t) = \frac{dr(t)}{dt}. \quad [2.14]$$

Equation [2.14] can be substituted in Equation [2.11] to determine the shock pressure as a function of time. However, Equation [2.11] does not take into account the effect of temperature on the shock pressure. When the air surrounding the arc column dissociates and ionizes, the density ratio of the shock discontinuity increases [6, p. 209]. Since the resistance coefficient K_1 is dependent on γ , it increases significantly, as well as the pressure in Equation [2.11]. Although the equation for the arc radius has been experimentally verified, the effect of the temperature on the pressure calculation has not been.

Berge and Manthy [4] related the initial arc expansion velocity to the di/dt of the system

$$u_1 = \alpha \left(\frac{V_{br}}{L} \right)^4, \quad [2.15]$$

where α = gas constant, V_{br} = breakdown voltage, and L = circuit inductance. The voltage over inductance term is equivalent to the current derivative of the system. Equation [2.15] only predicts the initial velocity, whereas Equation [2.14] gives the velocity as a function of time. Equation [2.15] yields a lower initial value for u_1 than Equation [2.14]; however, the values are on the same order of magnitude. Either may be substituted into Equation [2.11] to find the initial arc pressure.

2.1.4 Plasma Jet

During conduction in high current spark gaps, a cloud of ionized electrode vapor forms near the electrode surface. This cloud streams toward the opposite electrode at supersonic speeds. As it passes through the cathode and anode fall regions of the arc, it becomes superheated. The stream of vapor is called the plasma jet, and is thought to be a mechanism for electrode erosion. The mechanism behind the existence and acceleration of the jets are not well understood. However, a literature review of the subject in 1978 concluded that the energy in the jet is proportional to the arc current multiplied by the arc voltage minus the cathode voltage [9]. Experiments have shown the following correlation between the plasma jet and electrode erosion: the plasma jet is a major source of electrode heating, erosion decreases significantly as gap spacing is increased, and lowering the atomic weight of electrodes reduces erosion [10].

2.1.5 Thermal Pressure

Materials expand and contract when subjected to heating and cooling. A change in length is directly proportional to a change in the temperature of a body. The linear expansion may be calculated by

$$\Delta l = \alpha l_o \Delta T, \quad [2.16]$$

where α = coefficient of linear expansion, l_o = original length, and ΔT = temperature differential. A large thermal gradient can cause a substantial change in length, and stresses may be generated. The larger the value of α , the higher the stress. Thermal pressure may be calculated from

$$P_{thermal} = Y\alpha\Delta T, \quad [2.17]$$

where Y = Young's modulus, a measure of strength of materials. If the thermal energy is known, the temperature difference may be calculated from

$$\Delta T = \frac{E_{thermal}}{mc_v}, \quad [2.18]$$

where m = mass and c_v = specific heat at a constant volume. Equation [2.18] may be substituted into [2.17] to calculate the thermal stress on the electrode.

Calculating the thermal energy deposited in the electrode is not a trivial problem. The conservation of energy equation for general heat conduction problems is [11]

$$\rho c_v \frac{\delta T}{\delta t} = \nabla \cdot k \nabla T + \frac{dQ}{dt}, \quad [2.19]$$

where ρ = mass density of the material, c_v = specific heat at a constant volume, k = thermal conductivity, T = temperature, and Q = heat. For an electrode, the term dQ/dt is the Joule heating, which is negligible compared to the heating by the arc [5]. Ignoring the Joule heating term, Equation [2.19] may now be reduced to

$$\rho c_v \frac{\delta T}{\delta t} = k \nabla^2 T. \quad [2.20]$$

The boundary condition for the electrode surface receiving the heat from the arc is

$$k \nabla T = -q, \quad [2.21]$$

where q = heat flux density from the arc. The difficulty comes in defining the dominant mechanism of heat flux density. It has been attributed to radiation from the arc to the electrode, the impact of the plasma jet on the electrode, and has been approximated as a function of arc current density and electrode voltage potential [9, 10].

The problem may be simplified by assuming that the graphite electrode reaches sublimation temperature (3400 °C). Since arc temperatures typically reach up to 60,000 °C [5], this is a reasonable assumption. Since the heating is due to a transient phenomenon, only localized heating occurs. The distance that the heat flux travels in a given length of time is [12]

$$l_{char} = \sqrt{\gamma t}, \quad [2.22]$$

where

$$\gamma = \frac{k}{\rho c_v}. \quad [2.23]$$

2.2 Impulse Loading of Materials

The reaction of a material to stress is different under static and impulsive loads. An impulse, or impact, stress is defined by a pressure increase in a fraction of microseconds, followed by a rapid decrease, with an overall pulse duration of several microseconds [13]. All dynamic loads should not be characterized as impulsive. However, the conditions of this experiment produce transient, extreme stresses; therefore, the discussion will be limited to impact loading.

2.2.1 Stress-Strain Relationship

Strain is induced in a material when stress is applied. Strain is defined as

$$\varepsilon = \frac{\Delta l}{l_o}, \quad [2.24]$$

where Δl = change in length and l_o = original length. The relationship between stress and strain is nonlinear and different for every material. Stress-strain curves, like the one shown in Figure 2.1 are obtained experimentally by gradually increasing a tensile load on a bar. The increase in pressure is slow enough to be considered static.

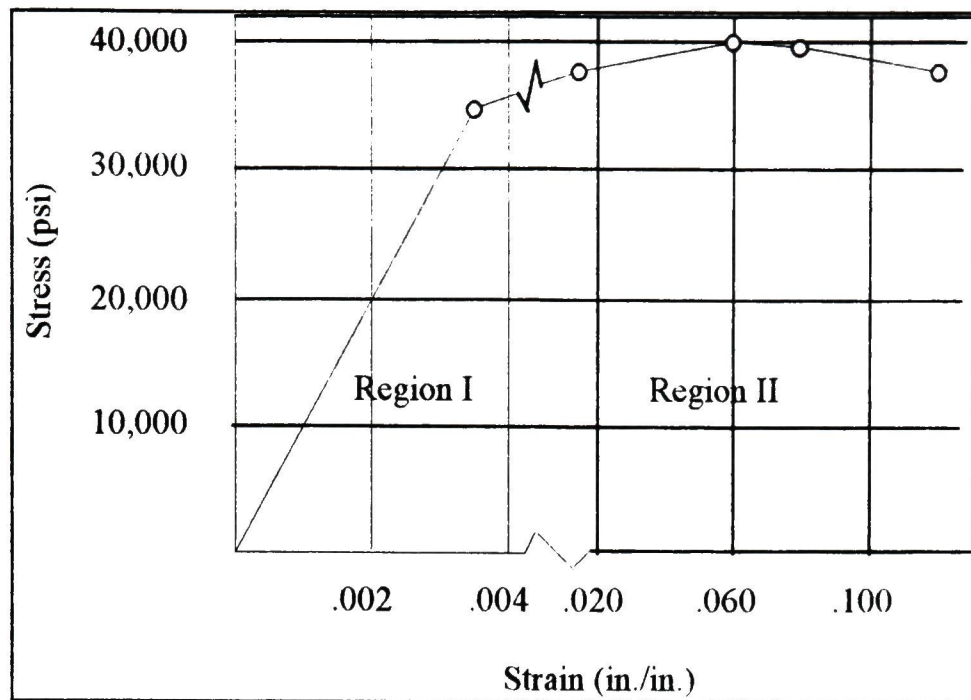


Figure 2.1 Stress - Strain Curve for Aluminum

Region I denotes the elastic behavior of the material, wherein the aluminum returns to its original state after the load has been removed. The elastic limit is the highest stress that can be applied without permanently altering the material. Generally, the elastic limit is slightly higher than the proportional limit, or the highest stress that is linearly proportional to strain. Region II contains the region where the material suffers plastic deformation and failure. At the yield point, the aluminum begins to deform with no increase in stress. Finally, the ultimate strength is the maximum load the aluminum can handle before fracture occurs. Although aluminum is used as an example, each material has a unique stress-strain diagram.

Region I is usually, but not always, the linear region of the curve, and it is the most useful for material studies. Past the proportional limit, the stress - strain relationship becomes nonlinear and difficult to interpret. Below the elastic limit, longitudinal stress is defined as

$$\sigma_l = Y \epsilon_l, \quad [2.25]$$

where σ_l = longitudinal stress, Y = Young's modulus, and ϵ_l = longitudinal strain. Shear, or transverse, stress is defined as

$$\sigma_s = G \epsilon_s, \quad [2.26]$$

where σ_s = shear stress, G = shear modulus, and ϵ_s = shear strain.

Metals react differently under static and dynamic loading conditions. In general, materials can sustain substantially higher transient stresses than static stresses. Usually an

increase in strain rate raises the entire stress level of the flow curve of a material, including the yield strength and the ultimate strength [13, pp. 21 -27]. High temperatures also affect the stress-strain curve of a material. Increasing the temperature of a metal tends to decrease the ultimate strength, and influences the type of plastic failure. In a study of strength of molybdenum, high temperatures reduced the elastic limit of molybdenum by one-third of the room temperature value [14].

2.3 Propagation of an Impulse Through a Material

As mentioned previously, pressures must approach 10^6 atmospheres before they are considered strong shocks in a solid. In most cases, including this one, a shock wave may be treated as a strong acoustic wave traveling through a solid. The propagation of an acoustic pulse through a solid object depends on several factors. Refraction, as well as the geometry of the object, affect the direction of propagation. Reflections affect the direction and magnitude of a pressure pulse. The velocity of propagation is dependent on whether the wavefront is longitudinal or shear, or whether the material is in an elastic or plastic state. The magnitude and waveshape of a pressure pulse is somewhat dependent on the material properties of a solid.

In this experiment, a spherically diverging shock wave impacts the spherical tip of the graphite electrode. The resulting refraction and propagation through the electrode will be discussed. As the pressure propagates, it encounters a material mismatch between the graphite electrode and a long ceramic bar. The reflections due to the material discontinuity will be discussed, as well as the dispersion in the ceramic bar. This section will conclude with a general discussion of acoustic propagation through a solid, and the effect of the material properties of graphite on the propagation.

2.3.1 Refraction

When a traveling wave intercepts a boundary between two different media, the wave will reflect and refract. In the case of normal incidence, the wave will be partially reflected and partially transmitted, which will be discussed later in this section. In the case of oblique incidence, the wave strikes the boundary at an angle that is not normal to the surface. There will be reflected and transmitted component; however, the transmitted wave is refracted. The relationship between the incident, reflected, and refracted waves is

$$\frac{1}{c_1} \sin \Theta_i = \frac{1}{c_1} \sin \Theta_r = \frac{1}{c_2} \sin \Theta_t, \quad [2.27]$$

where c_1 = propagation speed in medium 1, c_2 = propagation speed in medium 2, Θ_i = angle of incidence, Θ_r = angle of reflection, and Θ_t = angle of refraction. The first term in Equation [2.29] represents the incident wave, where the second and third terms represent the reflected and refracted waves, respectively. A diagram of the wave reflection and refraction may be seen in Figure 2.2. Since the incident and reflected waves are in the same medium, the angle of reflection equals the angle of incidence. If the two mediums have different propagation velocities, the angle of refraction differs from the incident angle.

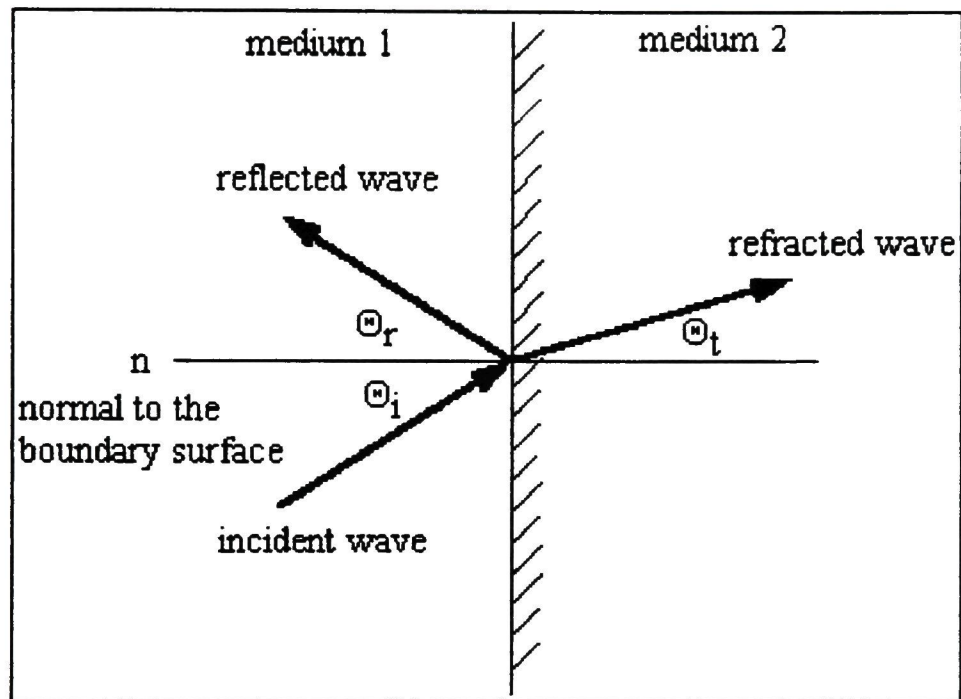


Figure 2.2 Incident, Reflected, and Refracted Waves Between Two Media

The arc-induced shock wave diverges and eventually strikes the convex surface of the switch electrode. Initially, the incident wave will refract at the electrode boundary, creating longitudinal and shear components that travel at different speeds. Each time the wavefront reaches a material boundary, the wave will reflect or refract, changing the magnitude and direction. Every time the propagation direction changes, new longitudinal and shear components are created.

2.3.2 Reflection

When a traveling wave encounters a sharp discontinuity in a medium at normal incidence ($\Theta_i = 0$), the incident wave is split into reflected and transmitted waves. Since the incident wave strikes perpendicular to the boundary, the angle of propagation of the transmitted wave is unchanged, unlike the refracted wave. This is evident from Equation

[2.27]. Assuming the propagation velocities, c_1 and c_2 , are nonzero, $\Theta_r = 0$ and $\Theta_t = 0$ if $\Theta_i = 0$.

The boundary condition for a plane wave, $P_1(x,t)$, at an interface is

$$P_1(x,t) = P_2(x,t) \quad [2.28]$$

where

$$P_1(x,t) = P_i(x,t) + P_r(x,t) \quad [2.29]$$

and

$$P_2(x,t) = P_t(x,t) \quad [2.30]$$

where $P_i(x,t)$ = incident wave, $P_r(x,t)$ = reflected wave, and $P_t(x,t)$ = transmitted wave.

The reflected wave undergoes a phase shift, thereby changing directions. The ratio of the reflected to incident amplitude is

$$\frac{P_r}{P_i} = \frac{(R_2 - R_1)}{(R_2 + R_1)} \quad [2.31]$$

The transmitted wave travels in the same direction as the incident wave, and the ratio of the transmitted to incident amplitude is

$$\frac{P_t}{P_i} = \frac{2R_2}{(R_2 + R_1)} \quad [2.32]$$

Equations [2.28] through [2.32] may be applied to the propagation of any type of wave, whether it is optical, acoustical, or electrical. The ratios of reflected and transmitted waves can also be extended to transmission lines. A sudden discontinuity in resistance gives rise to reflections in voltage signals of electrical transmission lines and pressure signals in acoustical transmission lines. Acoustic resistance, or impedance, is defined by

$$R_a = \rho c, \quad [2.33]$$

where ρ = material density and c = acoustic velocity.

Acoustical transmission lines may be treated and analyzed much the same as electrical transmission lines. This duality is a key element in the acoustical transmission line modeling in Chapter 4. The graphite electrode and ceramic bar from the experiment are treated as acoustical transmission lines to determine the propagation through the ceramic bar. Table 2.1 lists the dual electrical and acoustical properties.

Table 2.1 Dual Electrical and Acoustical Properties [15]

Electrical		Acoustical	
Quantity	Symbol	Quantity	Symbol
Voltage	$V = L di/dt$	Pressure	$p = M dx/dt$
Current	$I = dQ/dt$	Volume Current	$x = dX/dt$
Charge	Q	Volume Displacement	X
Resistance	$R_e = V/I$	Resistance	$R_a = p/x$
Inductance	L	Moment (Inertia)	M
Electrical Capacitance	C_e	Acoustical Capacitance	C_a

If a pressure pulse is applied to a freely suspended cylindrical bar and the pulse time is shorter than the transit time of the bar, the wave will reflect back and forth between the free ends. The pulse passes through the midpoint of the rod twice as often as it passes the ends. When a traveling wave reaches the free end of the bar, it is completely reflected. The shape of the reflected pulse is the same as the incident pulse but of opposite polarity; therefore, a compression pulse will be reflected as a tension pulse. Dispersion and losses in the bar will eventually lengthen and smooth the pulse shape. If the pulse length becomes longer than twice the transit time of the bar, the nature of the problem is changed. The bar may be considered as moving with a constant velocity, oscillating about its center of gravity.

2.3.3 Propagation of Shock Waves Through Solids

The shock pressures generated in this experiment are calculated in Chapter 4 to be much less than 10^6 atmospheres; therefore, the wavefront propagation will be treated with acoustical wave physics. The equation of motion of an elastic medium is [16]

$$\rho \frac{\delta^2 u}{\delta t^2} = (\lambda + \mu) \frac{\delta \Delta}{\delta x} + \mu \nabla^2 u, \quad [2.34]$$

where u = displacement, ρ = density, Δ = change in volume. The constants λ and μ are Lamé's constants which are inherent properties of a material. Equation [2.34] corresponds to two types of motion, dilatational (longitudinal) and rotational (shear). If there is no shear component to the motion, Equation [2.34] becomes

$$\rho \frac{\delta^2 u}{\delta t^2} = (\lambda + 2\mu) \nabla^2 u. \quad [2.35]$$

The corresponding dilatational velocity is

$$v_l = \sqrt{\frac{(\lambda + 2\mu)}{\rho}}. \quad [2.36]$$

If there is no longitudinal displacement, Equation [2.34] becomes

$$\rho \frac{\delta^2 u}{\delta t^2} = \mu \nabla^2 u. \quad [2.37]$$

The corresponding shear velocity is

$$v_s = \sqrt{\frac{\mu}{\rho}}. \quad [2.38]$$

In effect, the dilatational and rotational motion may be separated. For this experiment, the longitudinal propagation is the only one of interest.

When a medium is bounded, it affects the wave propagation. In a long cylindrical rod, the longitudinal propagation velocity is

$$v_c = \sqrt{\frac{Y}{\rho}}, \quad [2.39]$$

which is different than Equation [2.36].

As mentioned, dispersion distorts a pulse that propagates down a long cylinder. Dispersion occurs at high frequencies, as well as if the pulse wavelength is comparable to the cylinder radius. At high frequencies, the propagation velocity of a disturbance is dependent on the wavelength. Not only will dispersion lengthen the pulse and round off sharp gradients, it will also introduce oscillations in the pulse.

To model the propagation of a shock wave through an object, several researchers have used ray tracing techniques. This has become especially useful in the study of extracorporeal shock wave lithotripsy (ESWL), the medical procedure of fragmenting and removing kidney stones without invasive surgery. Shock waves are generated extracorporeally and focused on kidney stones, in vitro. Although the procedure is

preferable to other methods of kidney stone removal, there can be painful side effects and tissue damage due to the large number of shock waves that are used. In light of this, quite a bit of research has been done in order to make the procedure as efficient as possible.

To contribute to this research, Zhong and Chuong modeled the impact pressure of a spherical water jet on a planar elastic solid and the subsequent propagation through the solid [17]. They discovered that the impact pressure on the surface of the solid increased as the contact angle of the jet to the surface increased. As the jet velocity increased, the impact pressure on the solid surface could become significantly greater than the water jet pressure. Also, the shear stress varied from zero at the normal incidence to its maximum value at the outer edge of jet impact on the surface.

Gracewski, Dahake, and Ding also modeled the spherical shock propagation due to a ESWL pulse through a spherical solid, which corresponds to the conditions in this experiment [18]. Therefore, their model is incorporated in Chapter 4 to determine the refraction and propagation of the acoustic pulse through the electrode.

The difference between the ESWL procedure and this experiment is that the shock wave travels through liquid to reach the kidney stone but it travels through air before it impacts the electrode surface. However, this does not change the geometry of the system. A typical ESWL shock pulse has a lower magnitude than the shock produced by an arc, but the waveforms should be quite similar. Also, the consistency and material strength of the kidney stones are very similar to graphite. The similarities will be noted in the next section.

2.3.4 Propagation Through Graphite

For reasons mentioned in Chapter 1, graphite is a very good electrode material. However, the quality of graphite is highly dependent on the manufacturer and grade of the material. For this experiment, POCO graphite ACF-10Q is used exclusively. In one experiment, the same grade of graphite exhibited less erosion for a given charge transfer than any other electrode material tested [19]. It was theorized that the graphite erosion was low for the following reasons: Carbon does not melt, it sublimates at 3400 °C [20], and it has the highest sublimation energy per unit volume among the elements [19]. Also, at high temperatures, the strength of graphite exceeds that of other materials.

Graphite is one of the four naturally occurring forms of carbon. The other three are amorphous carbon, diamond, and buckminsterfullerene, or C₆₀. Amorphous carbon has no distinct structure, while graphite has hexagonally bonded layers, and diamond have tetrahedrally bonded layers. Graphite is one of the softest known materials, while

diamonds are one of the hardest. In C_{60} form, carbon is arranged in a truncated icosahedron and is one of the “slickest” materials known to man. Naturally occurring graphite is highly anisotropic, and it is mined and sold as a powder. Synthetic graphite is polycrystalline and has a high degree of isotropy; therefore, it is uniform in all directions [21].

Graphite has two properties that affect the failure of the material. First, it can stand little plastic deformation before it breaks. Unlike a ductile material, graphite cannot stretch, and it will not give noticeably before a fracture begins to propagate. Secondly, graphite is much weaker in tension than compression therefore it is susceptible to reflected tensile waves.

Zhong and Chuong compared the mechanical properties of different compositions of kidney stones to their susceptibility to fracture. They found that the stones with the higher wave speeds, impedances, and Young’s modulus were more difficult to fragment. The mechanical and acoustical properties of the ACF-10Q graphite are remarkably similar to those of the tested stones, which can be seen in Table 2.2. The tested stones, COM, Cystine, CA/MOD, and MAPH/CA, are calcium or magnesium compounds. They also found that surface erosion was due mainly to compressive and shear forces, while spalling at the back surface of the stones were due to reflected tensile waves.

Table 2.2 Mechanical and Acoustical Properties of Kidney Stone Composites and ACF-10Q Graphite

Material	Density (kg/m^3)	Velocity (m/s)	Impedance ($10^6 kg/m^2s$)	Young’ Mod. (GPa)
ACF-10Q	1800	3240	5.84	11
COM	1823	4476	8.16	24.5
Cystine	1624	4651	7.55	20
CA/COD	1732	2724	4.72	8
MAPH/CA	1587	2798	4.44	10.5

2.4 Fracture Mechanisms

Static and impact loads create a different stress environment in a body of material. Under a static load, the stresses and strains are distributed through the entire body. With an impulse load, localized stresses change very quickly. Transient stresses may lead to several types of failures [22]. Volume expansion results from a sudden release of high compression. Spalling and corner fractures derive from an intense concentration of stress. Radial fractures may be attributed to the lateral, or shear, motion due to diverging spherical or cylindrical waves.

For failure due to volume expansion to occur, all sides of the body must be compressed. It is unlikely that this is the failure mode in this experiment, and will not be discussed. The constructive interference of longitudinal waves, transverse waves, and their reflections results in corner fracturing. The location of wave interference is highly geometry dependent.

Generally, spalling is due to reflected tensile waves. At an unbounded surface, a compression pulse is completely reflected as a tensile pulse. The sudden removal of a compressive force on an object creates unloading waves, which are also tensile in nature. If the material cannot support the tension, a piece of the material, or the spall, will fly off.

Diverging pressure fronts cause radial stress fractures. Shear tension is created on the surface of the material as the stress front expands, and fractures appear like the spokes of a wheel. The number of spokes may be calculated from

$$n = \frac{2\pi v}{v_{crit}}, \quad [2.40]$$

where v = the particle velocity in the radial direction, and v_{crit} = critical impact velocity [22, p. 255].

2.5 Hypotheses of Electrode Failure

Physics International Company (PI) discovered a limitation of graphite electrodes when they tried to upgrade their high voltage, high energy MJB spark gaps. The MJB switches were regapped and the charging cable modified to handle 100 kV instead of 50 kV. A single switch test setup was devised for the tests, using either a 1.3 μ F, 100 kV capacitor or a 4 μ F, 100 kV capacitor. The total switch gap spacing was set to 0.3". Three grades of POCO graphite were used, with POCO ACF-10Q being the best grade. The test electrodes were either solid, hollow, or hollow with a tightly fit metal plug.

With this setup, the current rang at 60% to 75% reversal with time periods ranging from 2.5 μs to 8 μs . The switch electrodes survived a 250 kA, 8 μs pulse, but not a 250 kA, 2.5 μs pulse. The hollow and metal-plug reinforced electrodes performed as well as the solid ones as long as the shell thickness was at least 0.25" [23].

In similar tests, the solid graphite electrodes were separated from the mid-plane trigger by 0.3", instead of the total gap spacing being 0.3". The electrodes did not survive a single 310 kA pulse with a risetime of .9 μs . However, when the total gap distance was increased to 0.7", the electrodes survived 30 shots [24].

The graphite failure is in the form of spalling damage at the tip of the electrode. It has been observed that the amount of damage is proportional to the peak current, but the occurrence of the damage is dependent on the circuit di/dt . Graphite electrode failure is predicted if the peak current divided by one-quarter of the ringing time period exceeds 350 A/ns. Also, electrodes with a flat surface broke more readily than hemispherical electrodes [25].

Several pieces of information about the occurrence of the graphite failure stand out. First, the graphite survives multiple shots when the gap distance is increased. Secondly, the occurrence of damage is dependent on di/dt , but the severity of damage is dependent on peak current. Also, the location and occurrence of the damage depends on the profile of the electrode (flat or hemispherical), but not if it is hollow or not. This suggests that the damage is due to the constructive interference of stress waves and probably not to tensile waves reflected from the back surface of the electrode.

Experimental measurements in Chapter 3 compare pressure measurements in the switch as the gap spacing, current, and energy are varied, as well as other parameters. The effect of gap spacing and electrode geometry on pressure propagation in the electrode is analyzed in Chapter 4.

CHAPTER 3 EXPERIMENTAL SETUP AND DATA MEASUREMENT

Physics International's MJB switch handled a 250 kA oscillating current without electrode failure until the ringing time period was reduced to 3 μ s or less. It also switched over 300 kA with a slightly longer time period. The maximum di/dt that the electrodes could sustain was 350 A/ns. (Di/dt refers to the peak current divided by the quarter time period of the ringing pulse, and not the peak value of the current derivative. The true maximum derivative value is quite a bit higher than the peak current divided by quarter time period.) To create graphite electrode failure, these levels of current and risetime must be reproduced. PI provided an MJB switch with graphite electrodes, which was used in a low inductance, underdamped test circuit.

It will be shown in the measurements section of this chapter that the di/dt limit of 350 A/ns was exceeded without fracturing the electrodes. Although high di/dt levels may contribute to graphite electrode failure, they are not the sole cause. After it became evident that the electrodes would not fracture in this test setup, the focus shifted to measurements of the pressure that impacts the electrode surface. Relative pressure measurements were taken as the energy, current, gap spacing, gas pressure, and inductance were varied. Magnetic delay was added to the circuit to see if the delay in current affected the pressure magnitude or waveform. It will be shown in Chapter 4 that the shock pressure dominates the magnetic pressure on the surface of the electrode; therefore, the pressure measurements are assumed to be of the shock wave.

This chapter is divided into three sections. The first covers the experimental setup, with an emphasis on the low inductance design. The second section includes a discussion of the electrical and pressure diagnostics. The last section presents the experimental data, which includes measurements of the switch current and shock pressure.

3.1 Experimental Circuit

To achieve large, underdamped currents, a high energy storage capacitor is short circuited by the spark gap. The current is of the form

$$I = \sqrt{\frac{C}{L}} V_{br} e^{-\frac{R}{2L}t} \sin\left(\frac{1}{\sqrt{LC}}t\right), \quad [3.1]$$

where C = capacitance, L = inductance, R = resistance, and V_{br} = breakdown voltage. The resistance and inductance in the system are due only to the components, connections,

and, since this is a low impedance system, the arc. The resistance and inductance are determined experimentally to be 30 mΩ and 69 nH, respectively. To achieve di/dt values greater than 350 A/ns with a maximum charging voltage of 50 kV, the inductance must be less than

$$L = \frac{V}{di/dt} < 142.86 \text{ nH}. \quad [3.2]$$

The experimental inductance is well below the limit imposed by the di/dt requirement in Equation [3.2].

Not only do the storage capacitors have the advantage of having low inductance, and being adaptable to the switch, but they are manufactured to handle a large percentage of voltage reversal without adverse effects. They are rated for a maximum of 60 kV, and are operated up to a maximum of 50 kV for safety.

A diagram of the system is shown in Figure 3.1. The original switch has been modified slightly. The trigger plane was removed because it was unreliable. By removing the trigger and shortening the connections from the cathode plate to the top of the switch, the entire switch length was reduced considerably. A B-dot probe is built into the top of the switch, allowing current derivative measurements. The gap spacing between the electrodes may be varied by raising or lowering the nylon bolts that separate the anode plate from the cathode plate. Due to the removal of the electrical trigger, the switch self breaks and the breakdown voltage is governed by the gap spacing and the gas pressure.

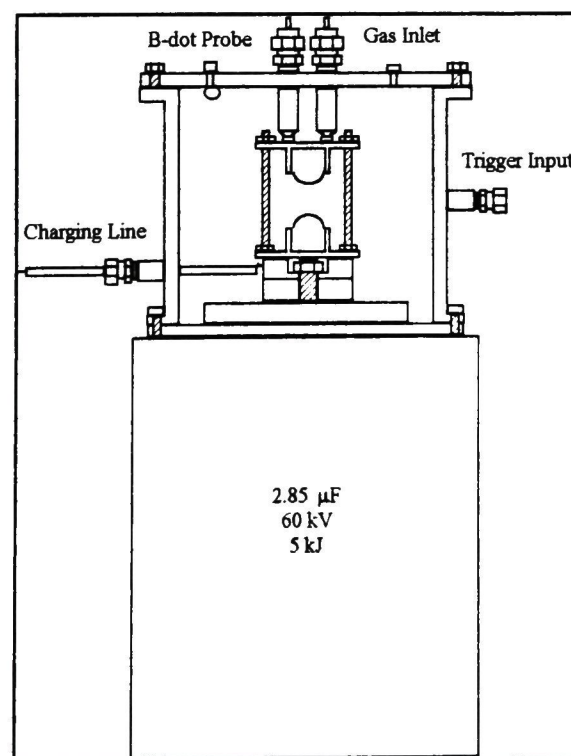


Figure 3.1 Modified MJB Switch

A Hipotronics 100 kV D.C. power supply has been modified to use as the charging power supply. The capacitor charging voltage is monitored by a resistive divider. A safety energy dump comprised of a vacuum relay and resistor is activated when the power supply is turned off. When the high voltage of the power supply is activated, the switch chamber is pressurized. As a safety precaution, the chamber pressure is released when the high voltage is disengaged.

3.2 Electrical Diagnostics

As mentioned, a B-dot probe is built into the top of the switch chamber. The relationship between the output voltage of the probe and the circuit current is [26]

$$V_{b\dot{d}ot} = NA \frac{dB}{dt} = NA \frac{\mu_0}{2\pi r} \frac{dI_{arc}}{dt}, \quad [3.3]$$

where N = number of turns of probe, A = cross-sectional area of probe, μ_0 = permeability of free space, and r = distance from conductor to probe. Equation [3.3] can be rewritten as

$$V_{b\dot{d}ot} = K \frac{dI_{arc}}{dt}, \quad [3.4]$$

where K = probe sensitivity. A current signal is obtained simply by integrating the B-dot signal. The integrator shown in Figure 3.2 has an output voltage of

$$V_{int} = \frac{1}{C} \int_0^t i dt, \quad [3.5]$$

where C = integrator capacitance and I = integrator current. If the time constant, RC, is much greater than the b-dot signal time period, the signal will be correctly integrated, and the integrator current is

$$i = \frac{1}{R} V_{b\dot{d}ot}, \quad [3.6]$$

where R = integrator resistance. Therefore the output of the integrator is

$$V_{int} = \frac{1}{RC} \int_0^t V_{b\dot{d}ot} dt. \quad [3.7]$$

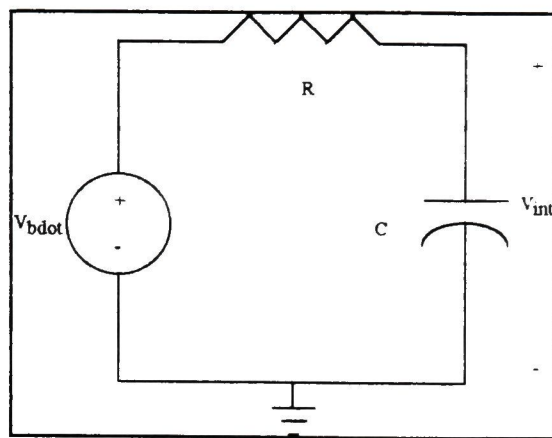


Figure 3.2 Integrator for B-Dot Probe

3.3 Pressure Diagnostics

3.3.1 Background

Determining the pressure on the electrode surface during a current pulse is not a trivial measurement. A pressure sensor cannot be placed directly on the electrodes for several reasons. First, although the cathode is ground to d.c. signals, this is not necessarily the case for a pulse. Any large voltage jump on the cathode could not only arc over to the sensor, but possibly damage any instrumentation to which it is connected. Likewise, shielding the sensor output against the surrounding electrical fields would be very difficult. If the sensor is too close to the area being measured, it can be destroyed by the shock wave it is trying to measure, high temperatures, or the high electrical and magnetic fields surrounding the electrodes. Any direct measurement, unless it is optical, is almost impossible.

Optical measurements of the displacement caused by the impinging pressure on the electrodes would eliminate any electrical interference, and deliver precise measurements of the strain rate and strain on the system. Interferometers called velocimeters measure the Doppler shift due to velocity changes instead of the fringe shifts due to displacement [27]. These systems have been used successfully in determining strain rates and strains in impact load studies of materials [28, 14]. Although this system would be ideal, the setup is difficult, the instrumentation is expensive and the diagnostic software is not available.

Accelerometers are a type of strain gage that measure quick accelerations due to velocity changes, and can be used to measure strain rate if placed at a point of velocity discontinuity. However, accelerometers have a natural oscillation frequency that limits the usable bandwidth to 15 kHz [29].

The frequency response of a strain gage is limited by the gage length, wavelength of incident pulse, and amplifier bandwidth. If the wavelength of the pressure is longer than

the effective gage length, the change in gage resistance is proportional to the average strain along the length of the gage [18]. The pressure peak and risetime will not be accurately represented, but relative measurements can be made. Since the output voltage is very small, on the order of 10^{-6} to 10^{-3} V, an amplifier is usually used to boost the signal. Unfortunately, the high gain required by the amplifier seriously restricts the frequency response of the gage. To eliminate the need for an amplifier, semiconductor strain gages are chosen over conventional metal foil gages. Semiconductor gages generally have gage factors that are two orders of magnitude larger than foil gages. The magnitude of the output signal is proportional to the gage factor; therefore, the semiconductor gages have a much larger output. This allows them to be used without amplifiers; however, the output is still on the order of millivolts.

To measure pressure exerted on an object, strain gages are mounted on the object in the axis that the force is applied. For this experiment, the compressive forces produced inside the switch will be measured; therefore, the gage will be mounted in the longitudinal direction. It is very important that the strain gage comes into intimate contact with the object that is being impacted. If the contact is not good, the pressure being exerted on the object will not translate to the strain gage. Reliable contact may be achieved by following the gage mounting instructions very precisely.

As pressure is exerted on the object being measured, the acoustic delay line in this case, the gage length changes slightly. The change in length creates a proportional change in the inherent resistance of the gage. The two terms are related through the gage factor, GF, by

$$\frac{\Delta R}{R} = GF \frac{\Delta l}{l}, \quad [3.8]$$

where R = initial gage resistance, ΔR = change in resistance due to pressure variation, l = initial gage length, and Δl = change in length due to pressure variation. Since the gage is mounted on the longitudinal axis, the longitudinal strain will be measured.

Measured strains are usually on the order of 10^{-6} in/in or m/m. Semiconductor gage factors are typically in the range of 100 - 150. Using these values in Equation [3.8], the ratio of $\Delta R/R$ will be approximately 10^{-4} . Generally, small changes in resistance values are difficult to detect; however, Wheatstone bridge circuits are ideal for this case. The Wheatstone circuit is shown in Figure 3.3.

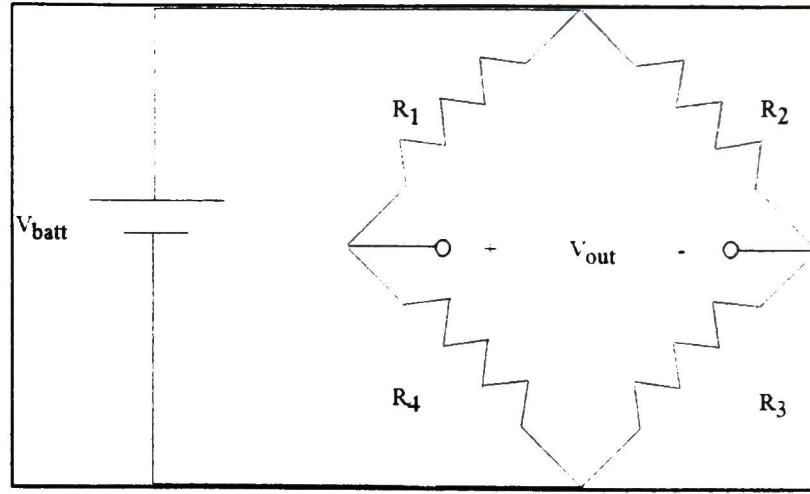


Figure 3.3 Wheatstone Bridge

The output voltage of the bridge is

$$V_{out} = V_{batt} \frac{R_1}{R_1 + R_4} + V_{batt} \frac{R_2}{R_2 + R_3} \quad [3.9]$$

The bridge is balanced when V_{out} is zero, which occurs when

$$\frac{R_1}{R_4} = \frac{R_2}{R_3} \quad [3.10]$$

If the bridge is balanced, a static strain is recorded as a d.c. offset. Dynamic strain is recorded as a time varying output voltage. If the gage measures static and dynamic strain simultaneously, it is recorded as a time varying signal with a d.c. bias. In this case, only the dynamic strain is of interest and any static strain will be filtered out. To understand the correlation between the output voltage of the bridge and the strain that is being measured, the differential voltage must be determined. If the strain gage is R_1 , then the differential of the output voltage with respect to R_1 is

$$\frac{dV_{out}}{dR_1} = V_{in} \frac{R_4}{(R_1 + R_4)^2} \quad [3.11]$$

By substituting ΔR from Equation [3.8] for dR_1 , and letting $R_1 = R_4$, now

$$dV_{out} = \frac{1}{4} GF \cdot V_{in} \cdot \frac{\Delta l}{l} \quad [3.12]$$

Since the input voltage and gage factor are constants, the differential output voltage is linearly proportional to the strain measured by the gage. If the strain gage is in position R_4 instead of R_1 , the output has the same amplitude, but opposite sign.

3.3.2 Setup

As mentioned, placing any sensitive diagnostics directly on the electrodes is impossible. Offsetting the diagnostics from the electrode but remaining inside the switch housing would reduce the possibility of damage. However, the electrical interference in the chamber would overcome any sensor output in the milliVolt range. This is the main reason the strain gages are placed outside of the housing. To further reduce noise from the system interfering with the pressure signal, an acoustic delay line is used. The delay is 50 μ s, long enough for the electrical pulse to damp out.

It is necessary to use an insulator for the delay line to prevent any high transient voltages from destroying the sensor. Ceramic, particularly alumina, has a high mechanical strength with a much larger elastic limit than Lexan or quartz. The elasticity is important because if the large pressure signal causes plastic deformation in the delay line, the sensor output will be highly distorted. Because ceramic has a large elastic modulus, the acoustic velocity is quite fast. Table 3.1 compares the mechanical strengths and acoustic velocities of alumina, quartz, and Lexan.

The length of the delay line is governed by the acoustic velocity of the ceramic and the amount of signal delay. To create a delay of 50 μ s, the gage must be offset from the electrode by a distance of

$$l_{delay} = v_{acoustic} t_{delay} = .47m = 18.5" \quad [3.13]$$

To prevent pressure wave reflections from the open end of the delay line interfering with the initial pressure signal, the sensor is placed in the middle of a 3 foot long ceramic rod. It takes 50 μ s for the signal to reach the gage, and 100 μ s for the signal to reach the end of the bar and be reflected back.

A hole was drilled in the brass cathode plate so the delay line could directly contact the electrode. This was done to prevent any reflections from the graphite/brass boundary and the brass/ceramic boundary from further complicating the results and attenuating the signal. Acoustic transmission gel was used to ensure a good, but not permanent, contact between the graphite and ceramic. The delay line extends out of the switch housing. Clamping the delay bar will distort the gage signal, but the air pressure must be maintained in the switch. An o-ring is used in the top switch plate to maintain switch pressure integrity and hold the bar into place without substantially distorting the pressure measurement. The setup is shown in Figure 3.4.

Table 3.1 Mechanical Characteristics of Delay Line Material [30], [20, p. 12-139], [31]

Material	Elastic Modulus (GPa)	Elastic Limit (GPa)	Acoustic Velocity (m/s)
Al ₂ O ₃ ceramic	345	2.07	9400
quartz	71.8	1.1	5900
Lexan	2.4	.086	1414

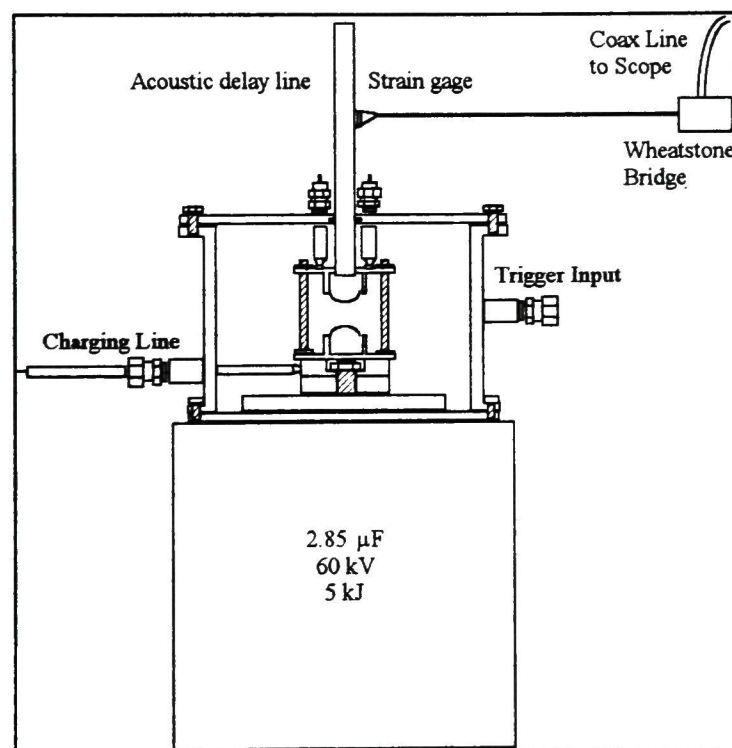


Figure 3.4 Pressure Measurement Setup

Since the strain gage output has such a small magnitude, shielding is very important. To reduce noise, the strain gage and the output wires are shielded. The output is sent to an enclosed box containing the Wheatstone bridge and a 9 V battery. A shielded coax cable transmits the output signal of the bridge to the oscilloscope inside the screen room.

The strain gage, Entran model #ESB-160-1000, has a resistance of 1000 Ω and can handle 25 mW power dissipation. A 9 V battery is used for a bridge power supply for simplicity, and because it does not exceed the power rating of the gage. The bridge is completed with fixed 1000 Ω resistors. Because the resistors and gage are not exactly

1000 Ω , there is a small d.c. offset, but it is negligible compared to the battery voltage. Since only the dynamic measurement is of interest, the small offset does not affect the measurement.

3.4 Data Acquisition

Electrical and pressure measurements are acquired and saved on a Tektronix 2440 digital oscilloscope. The scope has a maximum sampling rate of 500 Megasamples per second and a maximum bandwidth of 200 MHz, which is fast enough to record the signals in this project. A measurement is saved in one of the four reference files on the scope, and then sent to an IBM personal computer for permanent storage. Data may be exchanged back and forth between the scope and computer via an IEEE 488 Bus and GPIB card installed in the computer. However, for this experiment, the computer acts only as long term data storage, not as a controller. The data may be viewed graphically and also is converted into an ASCII file that contains the waveform information.

Generally the waveform of interest is imported into an EXCEL worksheet, where the data may be graphed and compared. For more mathematically rigorous calculations, the data are transferred to Mathcad. For these calculations, it is important to know two things about the ASCII files. First, they are in a single column containing 1000 points. Secondly, each time division of the oscilloscope contains 50 discrete points of information. Therefore, if the time base of the scope is set to 200 μ s, there will be a data point every 4 μ s, and the data string will end at 4 ms.

3.5 Data Interpretation

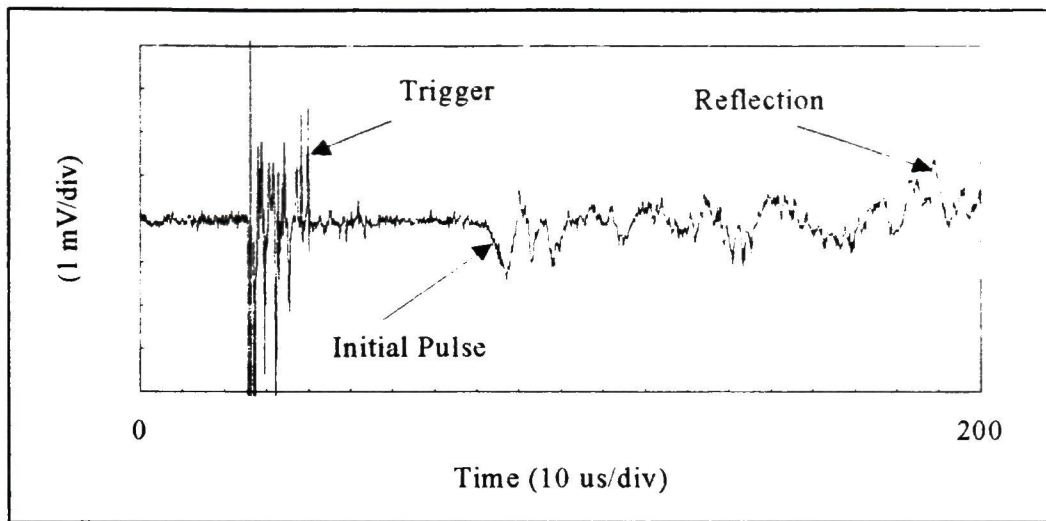
Several things should be explained before the data are shown. First, the initial pressure wave through the bar is the primary information of interest. This is captured on a relatively fast time base. At longer times, the vibrations of the delay bar and switch overwhelm the initial signal. The signal will be shown on a fast and slow time scale to point out the differences between the shock pulse and system vibrations. Secondly, if the wave were traveling through the ceramic bar only, the initial pulse followed by a reflection 100 μ s later would be expected. However, the electrode/ceramic boundary creates reflections in the signal before it travels to the end of the ceramic bar and back. Therefore, there will be information between the initial pulse and its reflection from the free end of the ceramic. Next, it will be shown that the pressure signal is not contaminated by excess noise. The strain gage data will only be used for relative measurements since the peak

pressure values and risetimes cannot be accurately represented. Therefore the results in the following sections will be left in the units of mV.

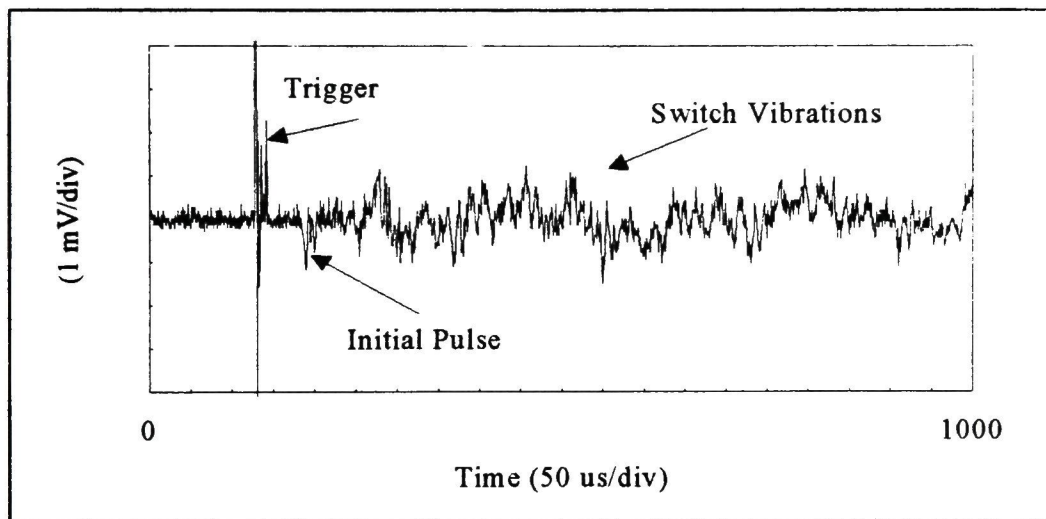
3.5.1 Time Scaling

The overall system reacts more slowly than the initial pressure wave. While the pulse width of the impulse signal from the shock wave is less than 10 μs , the vibrations from the switch chamber and ceramic bar are much slower. Figure 3.5 shows similar shots taken at three different time division settings on the oscilloscope. With a setting of 10 $\mu\text{s}/\text{div}$, the data resolution is one point per 200 ns. At this resolution, the initial pulse and subsequent reflections can be seen in Figure 3.5a. At 50 $\mu\text{s}/\text{div}$, there is one data point per 1 μs . Since the initial wavefront is only several microseconds long, the initial wavefronts can be recognized but not seen in detail in Figure 3.5b. At the end of the data, a slower resonance begins to show up, and this is the system vibration. At 200 $\mu\text{s}/\text{div}$, or one point per 4 μs , the original pulse is lost, but the vibrations can be seen. The two way transit time of the ceramic delay line is 200 μs , which corresponds to the resonance shown in Figure 3.5c.

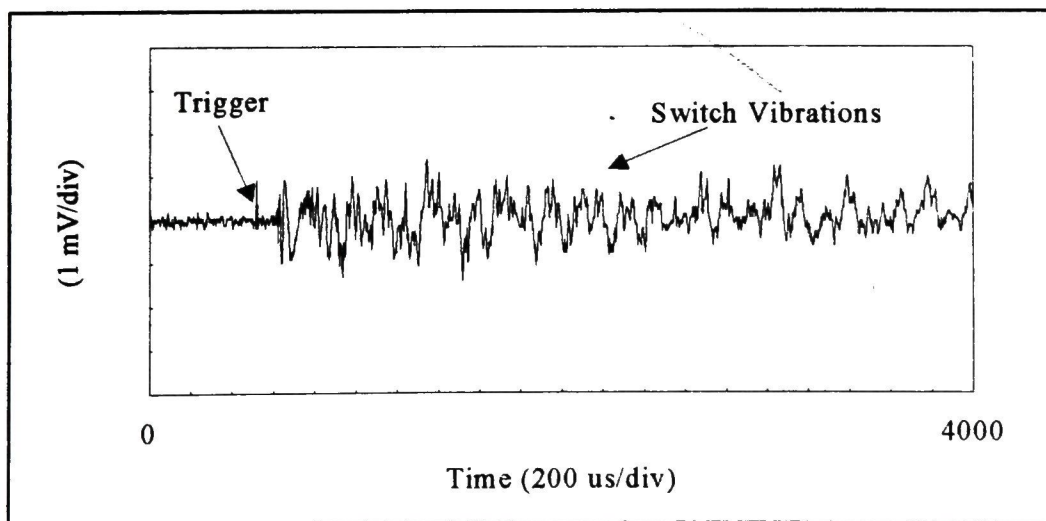
The signal from the B-dot probe was used to externally trigger the scope to take strain gage measurements for two reasons. First, the trigger level had to be set so low to catch the gage signal, that the scope would often trigger prematurely. Secondly, the time delay between the high current pulse and the onset of the acoustic pulse could be measured. The high frequency noise at the very beginning of each shot in Figure 3.5 is the electrical noise that the gage picks up; however, it dies out before the pressure signal begins. The time delay between the electrical noise and the pressure pulse is slightly over 50 μs , which is expected. As the time resolution of the scope becomes slower, the trigger pulse is filtered out.



(a)



(b)



(c)

Figure 3.5 Strain Gage Measurements with a Time Base of (a) 10 $\mu\text{s}/\text{div}$, (b) 50 $\mu\text{s}/\text{div}$, and (c) 200 $\mu\text{s}/\text{div}$

3.5.2 Signal Reflections

Since the electrode materials, graphite and stainless steel, and the ceramic have different acoustic impedances, there will be signal reflections at the interface of the two materials. Graphite has a much smaller impedance than ceramic, so the magnitude of the reflections will be significant. The impedance of stainless steel is almost identical to ceramic, so the reflections are negligible.

The spherical geometry of the pressure wavefront and electrode tip complicates the propagation. The original wave is nonplanar, and it does not strike the electrode tip at normal incidence, which can cause numerous reflections to show up after the initial pressure pulse. Therefore, the data in between the initial pulse and its reflection 100 μ s later can be attributed to the multiple reflections and dispersion of the acoustic wave due to the spherical electrode surface.

3.5.3 Noise Measurement

The output of the strain gage never exceeds 10 mV. Since the signal is so small, the signal to noise ratio is very important. If the amplitude of the noise is approximately the same as the signal, the measurements are not reliable. To check the noise level, the battery to the Wheatstone bridge was shorted to remove any external power sources, and a shot was fired. The results are shown in Figure 3.6. This was done periodically throughout the experiment. The noise level is at least a factor of five lower than the signal strength. A frequency analysis showed that the noise has no particular frequency component, which is as expected.

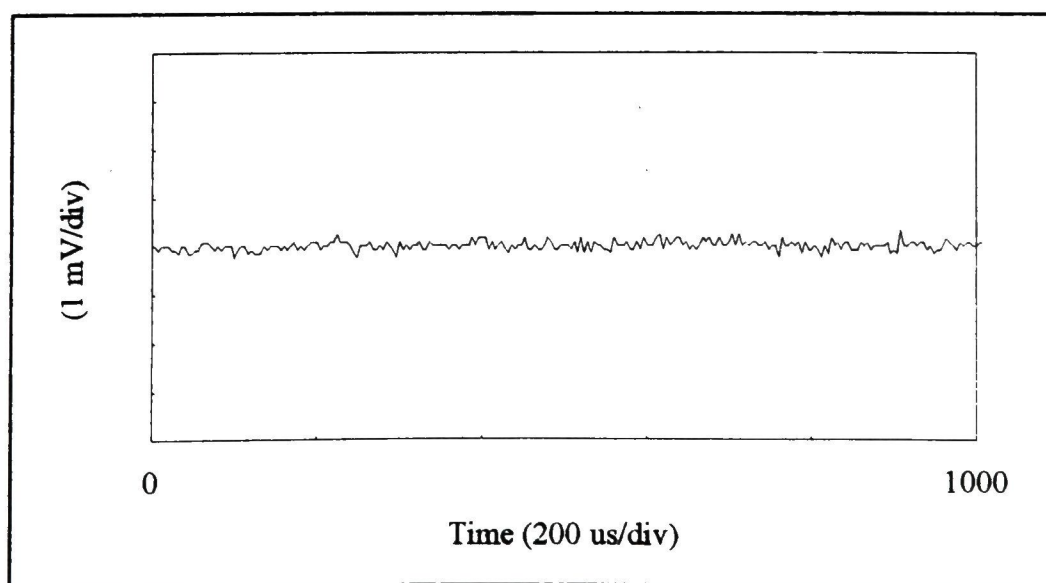


Figure 3.6 Noise Level of Experiment

3.6 Experimental Measurements

One goal of this project is to document how the shock pressure in the gap or its subsequent propagation through the electrodes is affected when certain parameters are varied. Differences in the electrical circuit include changing the charging voltage, changing the inductance, and by adding magnetic delay. Physical changes are made to the system by altering electrode gap spacing and electrode material. The effect of each individual variation is documented in the following sections.

It can be seen from Figure 3.5 that the trigger pulse and initial delay time is a substantial part of the data when the time base is set to 10 $\mu\text{s}/\text{div}$. The oscilloscope also has a preset delay before it triggers, which leaves an initial trailer with no data. For the measurements shown in this section, the trailer, trigger pulse, and initial time delay are omitted so that more of the strain gage signal may be seen. The measurements are shown from 70 μs , instead of the very beginning. These measurements are then expanded between 70 μs and 110 μs and overlapped to compare the magnitude and waveform of the initial shock pulses. The initial and final time of the measurements are shown on the horizontal axis, as well as the time per division.

Two shots were taken for each measurement to establish consistency. This was quite helpful in determining whether there was a problem with the experiment or diagnostics. For most of the measurements, the breakdown voltage was varied for four different gap spacings. During the experiment, it was discovered that if the air pressure in the switch exceeded 14 psi, the ceramic bar was forced out of the top of the switch. This could have been remedied by supergluing the ceramic to the back of the electrode. This was not done for two reasons. First, if the glue dried before good contact was made, it would be very difficult to saw the ceramic off and rebores the hole in the brass. Secondly, the switch had to be disassembled every time the gap spacing was changed, and gluing the ceramic to the electrode would have made assembly and disassembly very difficult. In all likelihood, the ceramic bar would have broken in the process.

Therefore, the air pressure was varied between 0 psi and 14 psi, and the gap spacing was varied from 0.25" - 0.5". When the electrode material and inductance was changed, and when the magnetic pulse shaping was added, pressure measurements were taken by leaving the gap spacing at 0.3", and varying the pressure. Table 3.2 lists the gap spacings used for the various operating parameters, and Table 3.3 summarizes the variations in the operating parameters.

Table 3.2 Summary of Gap Spacings versus Operating Parameters

Parameter	Gap Spacing			
	0.25"	0.3"	0.4"	0.5"
Gap Spacing, Constant Energy	x	x	x	x
Gap Spacing, Increasing Energy	x	x	x	x
Air Pressure	x	x	x	x
Inductance		x		
Magnetic Delay		x		
Electrode Material		x		

Table 3.3 Variations in Operating Parameters

Parameter	Variation	
Gap Spacing, Constant Energy	air pressure (0 psi, 6 psi, 10 psi, and 14 psi)	
Gap Spacing, Increasing Energy	gap spacing (0.25", 0.3", 0.4", and 0.5")	
Air Pressure	air pressure (0 psi, 6 psi, 10 psi, and 14 psi)	
Inductance	low (69 nH)	high (92 nH)
Magnetic Delay	without	with (25 ferrites)
Electrode Material	POCO graphite	stainless steel

3.6.1 Gap Spacing

The gap spacing is governed by raising or lowering the nylon bolts that separate the electrode plates inside the switch. The spacing is set by inserting a piece of metal of known thickness between the electrodes, and adjusting the nylon bolts, as shown in Figure 3.7. Measurements are taken for gap spacings of 0.25", 0.3", 0.4", and 0.5". The smallest spacing is chosen to be 0.25" because the electrode failure at PI occurred when the electrodes were spaced 0.3" apart. The largest gap spacing was limited to 0.5" so that the self breakdown voltage at atmospheric pressure would never be greater than 50 kV. Two sets of measurements are taken as the gap spacing is increased. In the first set, the energy is increased as the gap distance is increased. In the second set, the energy is kept constant as the gap distance is increased. By comparing the two sets of data, it can be seen if the energy or gap spacing, or a combination of both, affects the shock pressure.

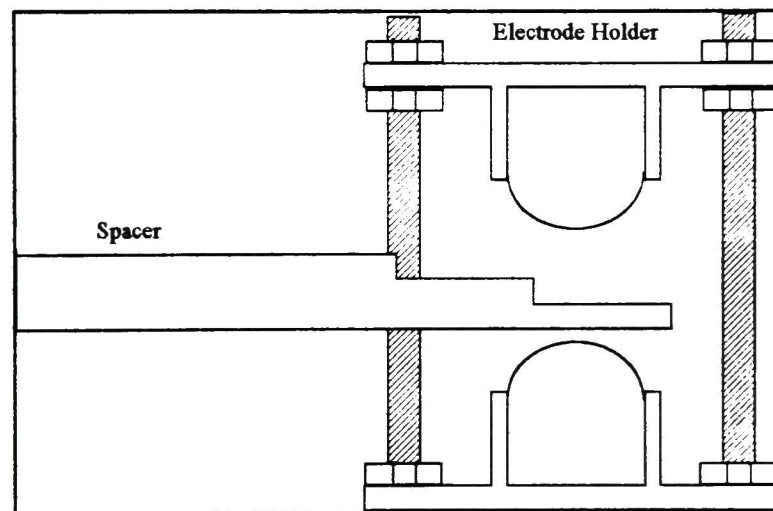
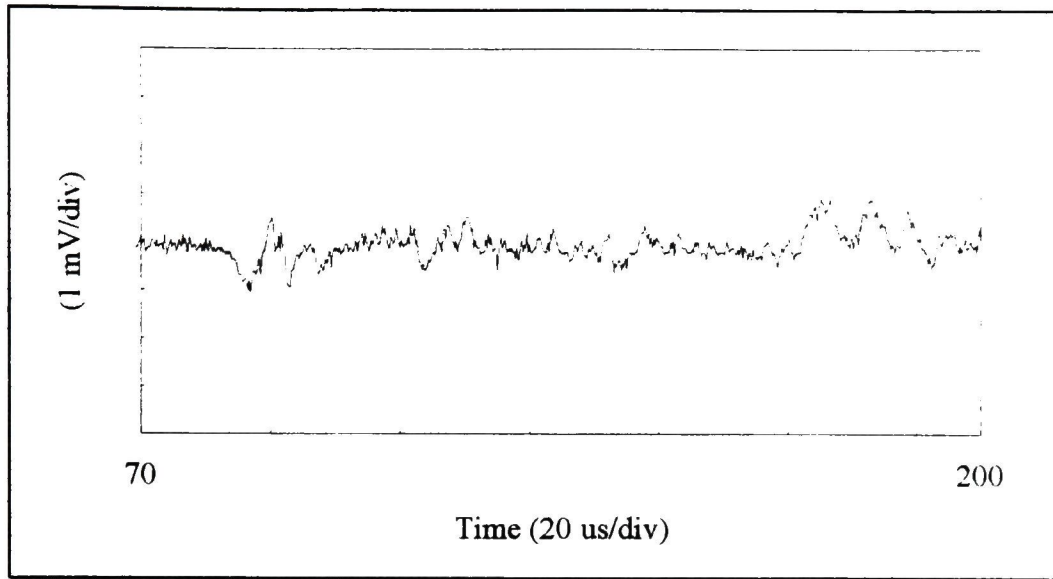
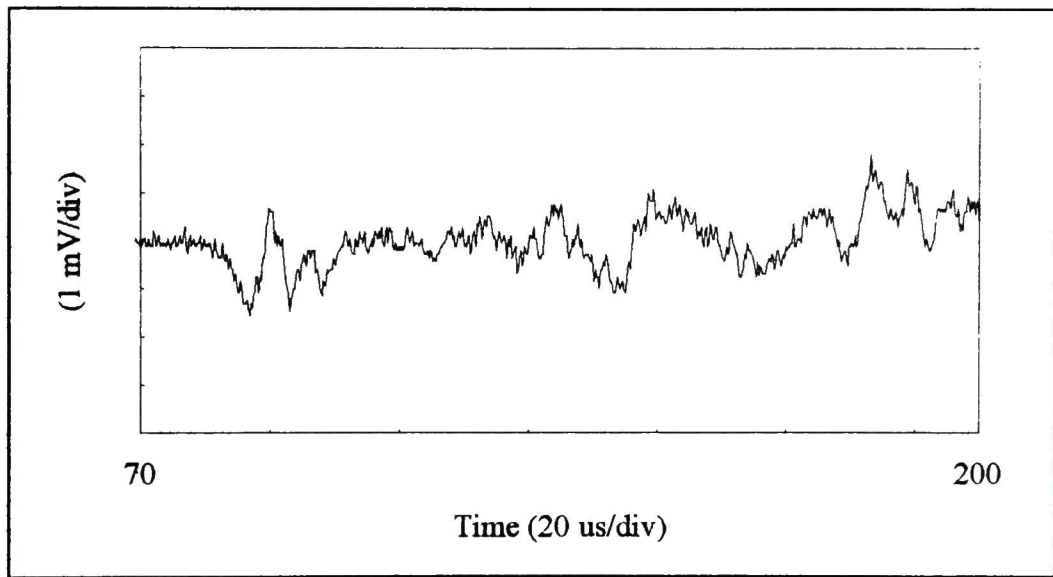


Figure 3.7 Gap Spacing Adjustment

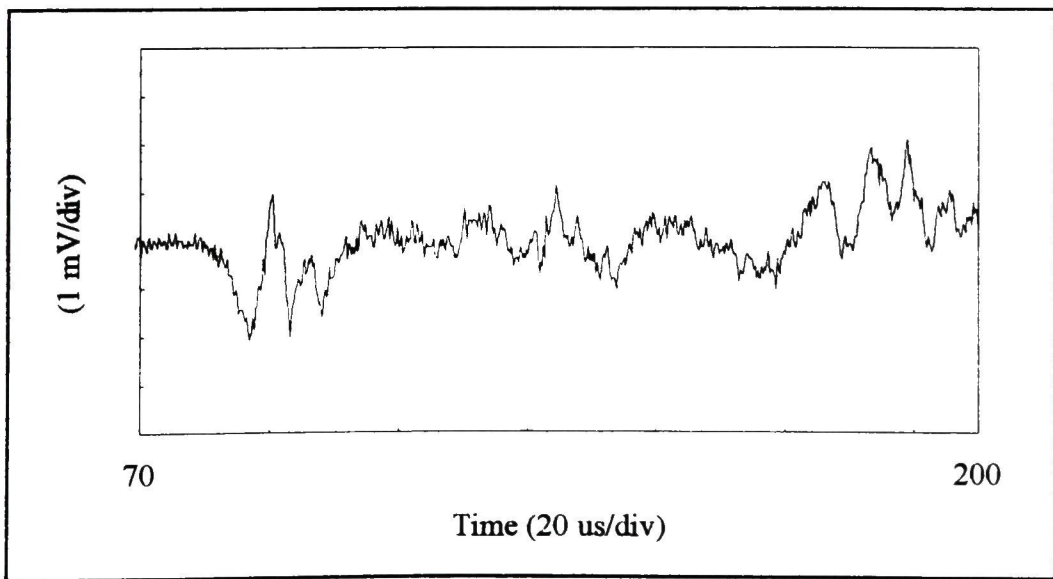
If the air pressure in the switch chamber is held constant, the switch breakdown voltage increases as the gap spacing increases. Figure 3.8 shows the measured shock pressure signals for each gap spacing with an air pressure of 6 psi. As the gap spacing is doubled from 0.25" to 0.5", the amplitude of the shock pulse quadruples. The initial pressure pulses from Figure 3.8 are compared in Figure 3.9. It will be seen in the second set of data that the shock amplitude remains fairly constant as the gap spacing is doubled and the energy is held constant. Table 3.4 shows the maximum measured shock amplitude as the gap spacing and breakdown voltage is increased. It can be seen from Table 3.4 that the increase in shock pressure magnitude corresponds more closely to the change in energy than the change in voltage. Although the magnitude is affected, the shape of the pressure pulse is not.



(a)

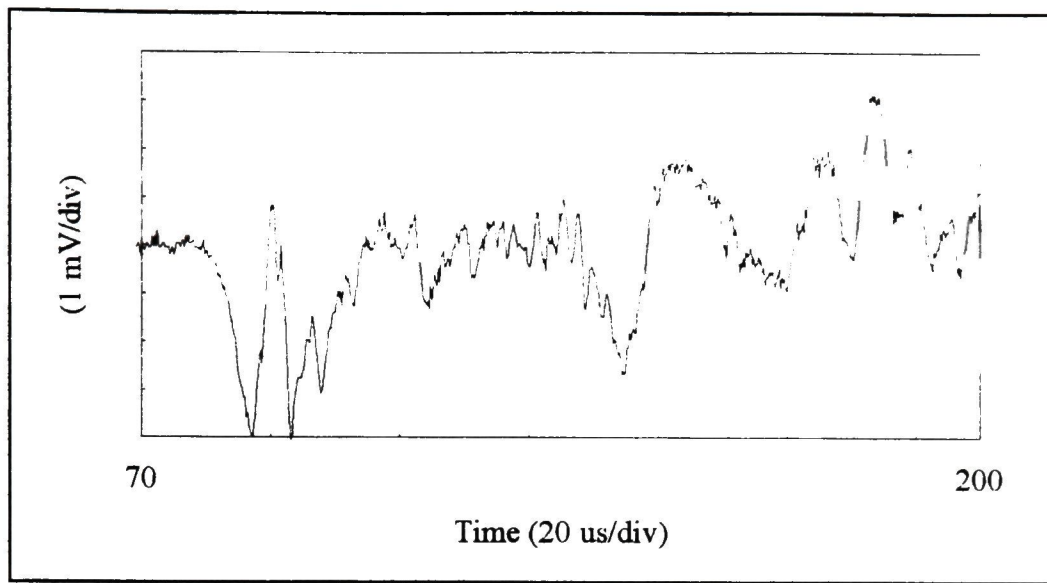


(b)



(c)

Figure 3.8 Measured Shock Pressure for Increasing Energy and Gap Spacings of (a) 0.25", (b) 0.3", and (c) 0.4"



(d)

Figure 3.8 continued. Measured Shock Pressure for Increasing Energy and Gap Spacing of (d) 0.5"

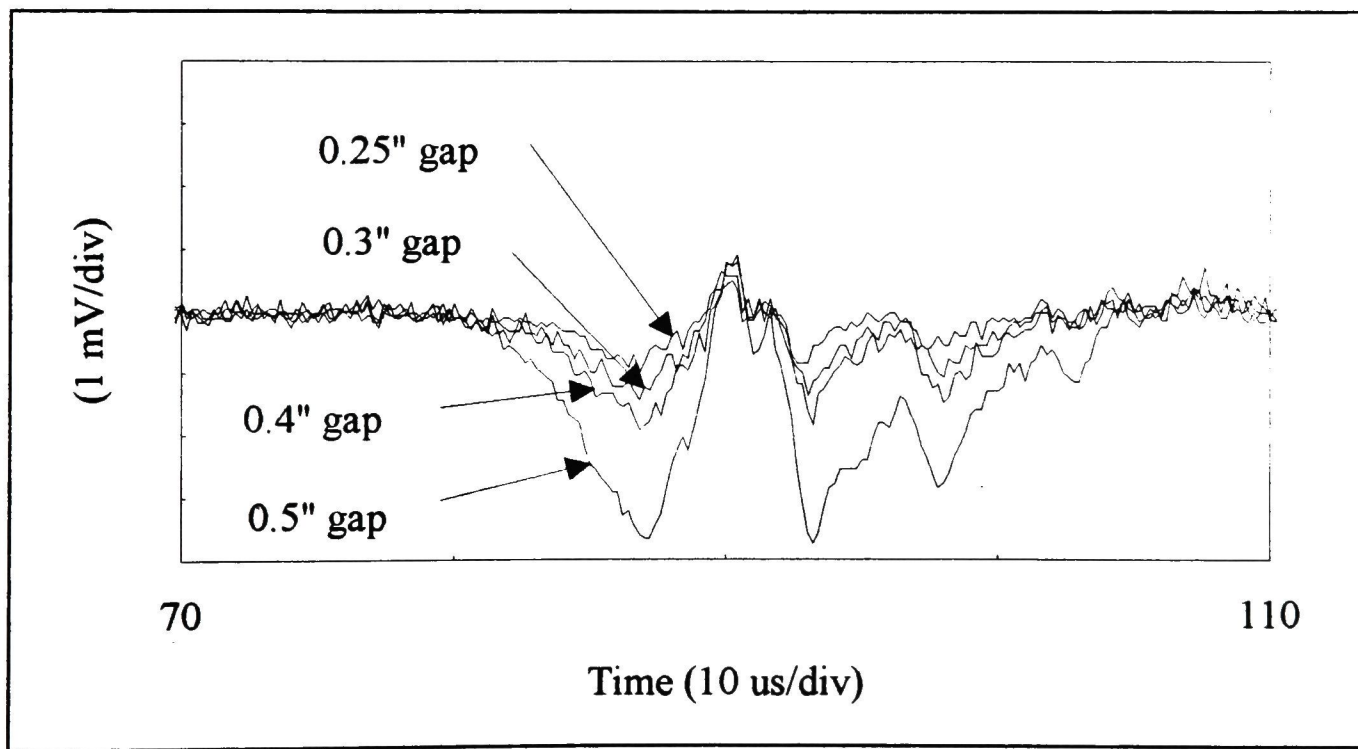
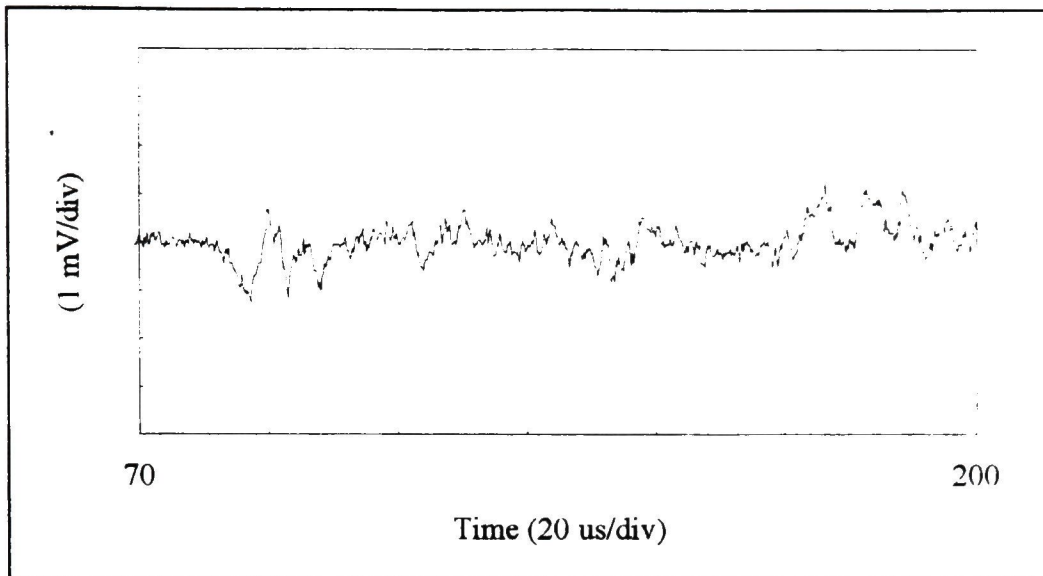


Figure 3.9 Initial Shock Pressures as a Function of Increasing Gap Spacing and Increasing Energy

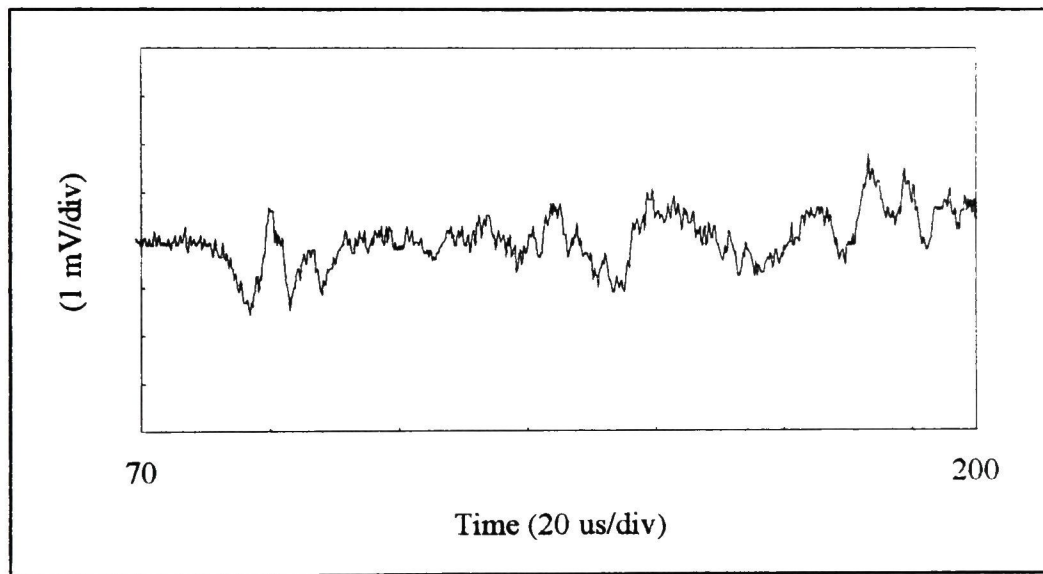
Table 3.4 Maximum Shock Amplitude versus Increasing Breakdown Voltage and Input Energy

Gap Spacing (in)	Shock Amplitude (mV)	Breakdown Voltage (kV)	Input Energy (kJ)
0.25"	1	28.2	1.12
0.3"	1.5	33.4	1.59
0.4"	2	41.4	2.44
0.5"	4	51.6	3.79

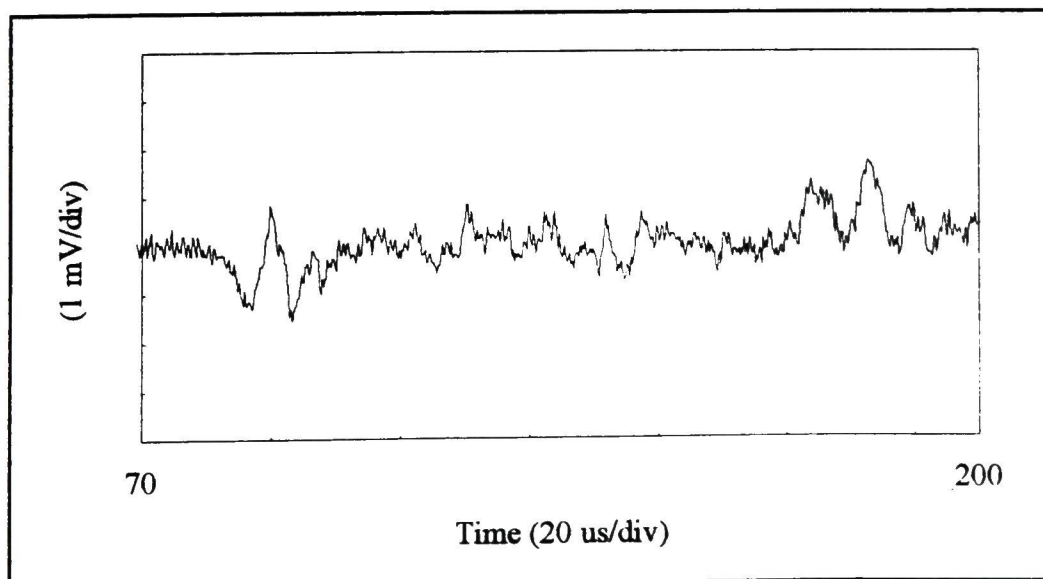
For the second set of gap spacing measurements, the ambient gas pressure was changed to keep the breakdown voltage relatively constant. The average breakdown voltage is 32.7 kV, with a maximum variation of 14% in breakdown voltage. The subsequent variation in energy is 26%, with an average of 1.52 kJ. Table 3.5 lists the maximum shock amplitude versus gap distance with constant energy. Figure 3.10 shows the measured shock pressures versus gap spacing for the shots listed in Table 3.5. Figure 3.11 compares the initial wavefronts from Figure 3.10, and there is no significant change in amplitude or waveform due to gap spacing with constant voltage or energy. The slight differences in magnitude in Figure 3.11 can be attributed to the fluctuations in breakdown voltage.



(a)

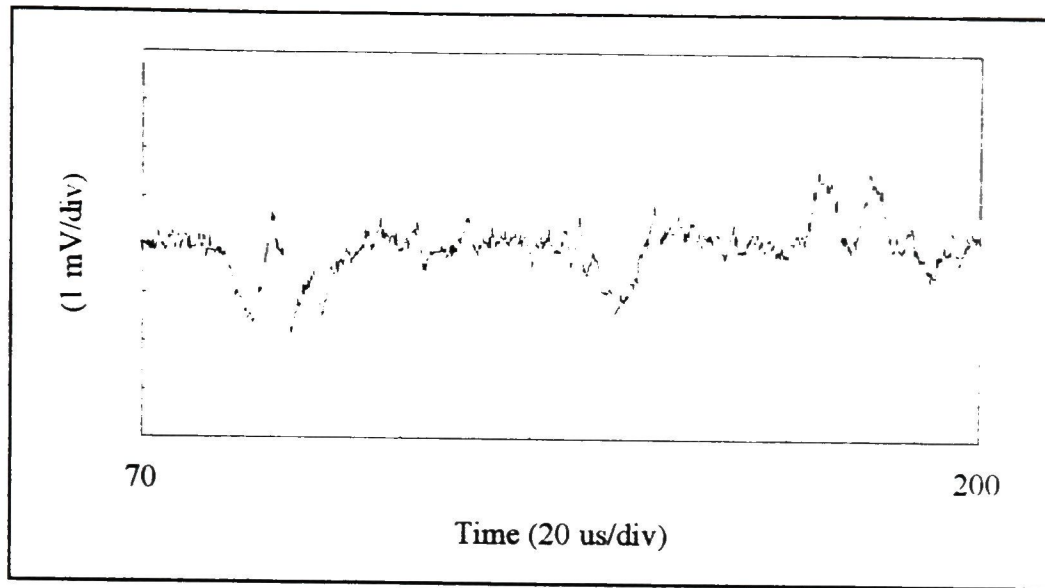


(b)



(c)

Figure 3.10 Measured Shock Pressure for Constant Energy and Gap Spacings of (a) 0.25", (b) 0.3", and (c) 0.4"



(d)

Figure 3.10 continued. Measured Shock Pressure for Constant Energy and Gap Spacing of (d) 0.5"

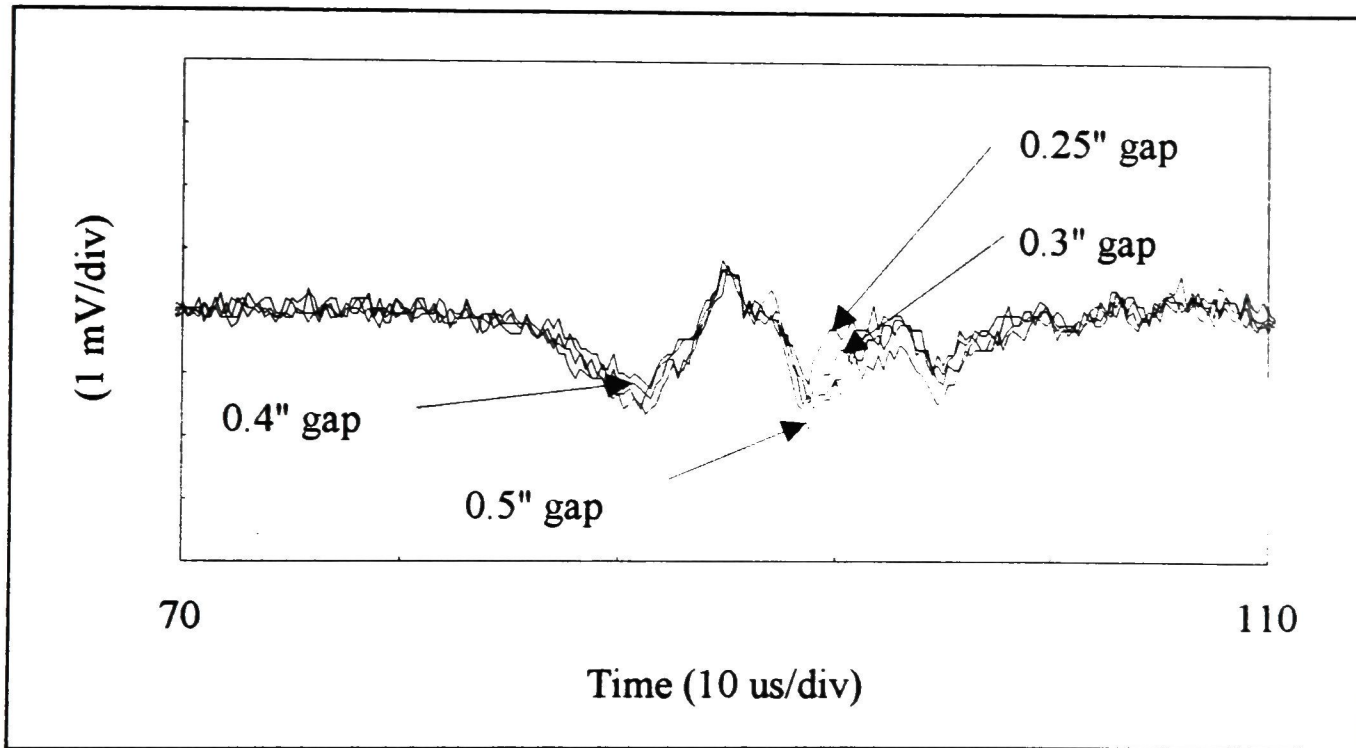


Figure 3.11 Initial Shock Pressures as a Function of Increasing Gap Spacing and Constant Energy

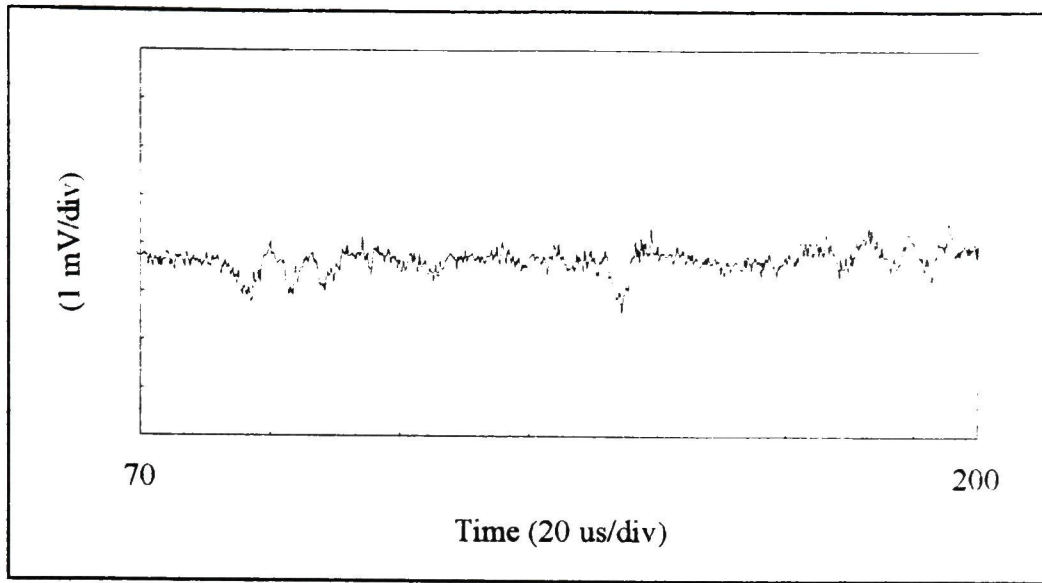
Table 3.5 Maximum Shock Amplitude versus Constant Breakdown Voltage and Input Energy

Gap Spacing (in)	Shock Amplitude (mV)	Breakdown Voltage (kV)	Input Energy (kJ)
0.25"	1.24	32.3	1.49
0.3"	1.40	33.4	1.59
0.4"	1.16	30	1.28
0.5"	1.56	34.9	1.74

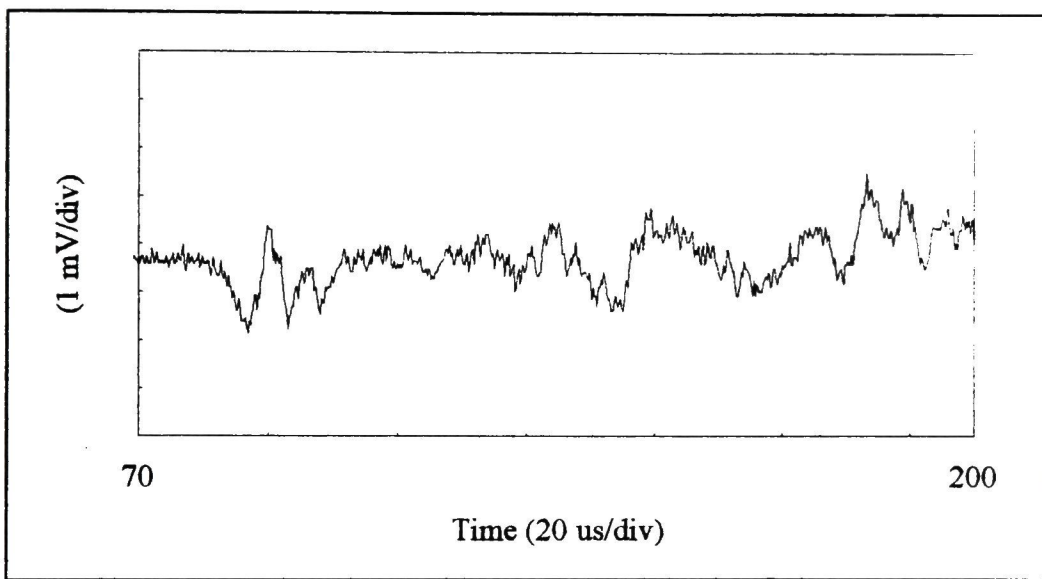
Comparing both sets of gap spacing measurements, it may be concluded that the increase in shock magnitude is due to the increase in energy and not gap spacing. The pressure amplitude was not shown to be inversely proportional to the gap distance, which supports the idea that the measured pressure is not primarily due to the plasma jet effect.

3.6.2 Gas Pressure

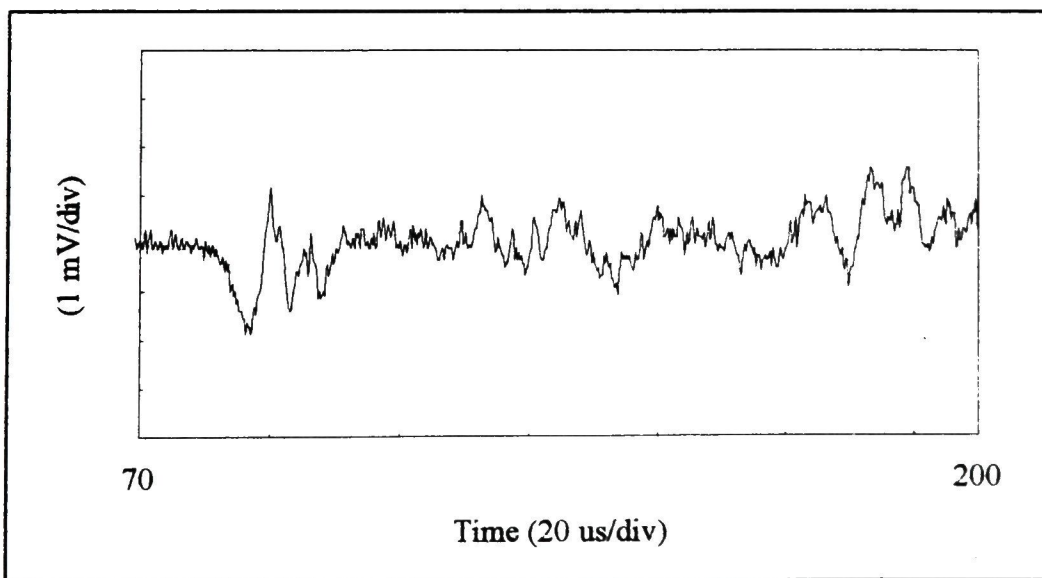
For this part of the experiment, gas pressure was varied and the gap spacing was kept constant to increase the holdoff voltage. Figure 3.12 shows the pressure signals for a constant gap spacing of 0.3" and increasing air pressure. Figure 3.13 compares the initial shock pressure wavefronts from Figure 3.12. Table 3.6 shows the maximum shock amplitude versus breakdown voltage and energy for these shots. There is not as significant of a difference in the pressure amplitudes in Figure 3.13 as there is in Figure 3.9. The change in energy in both sets of shots is approximately the same; however, the peak energy in Figure 3.9 is greater. The conclusion is that the peak energy has a greater impact on the pressure magnitude than the change in energy. Since the shock pressure is much greater than the undisturbed air pressure in the switch chamber, small changes in the ambient air pressure do not affect the shock.



(a)

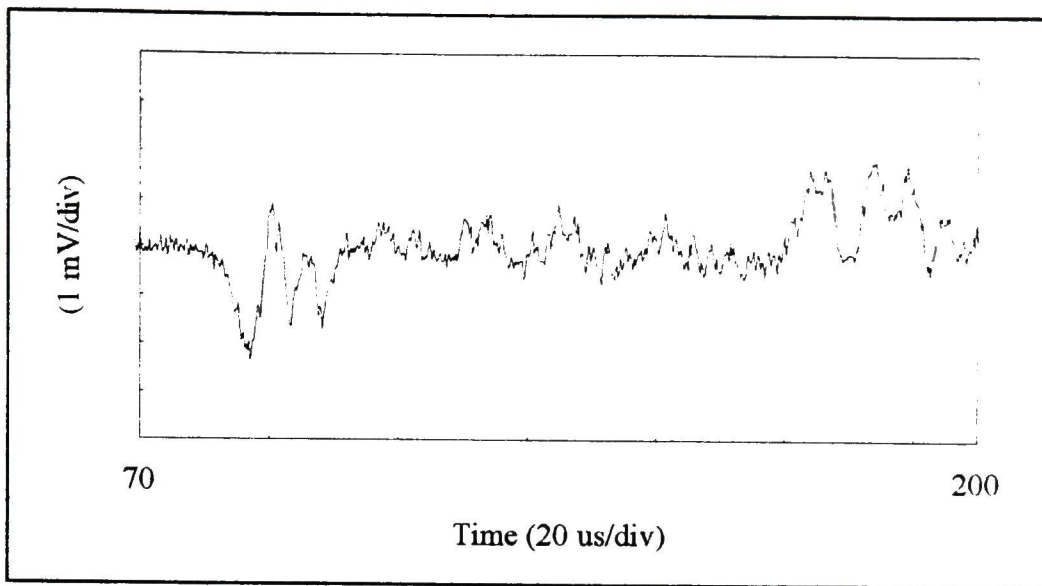


(b)



(c)

Figure 3.12 Measured Shock Pressure For Increasing Energy and Air Pressures of (a) 0 psi, (b) 6 psi, and (c) 10 psi



(d)

Figure 3.12 continued. Measured Shock Pressure for Increasing Energy and Air Pressure of (d) 14 psi

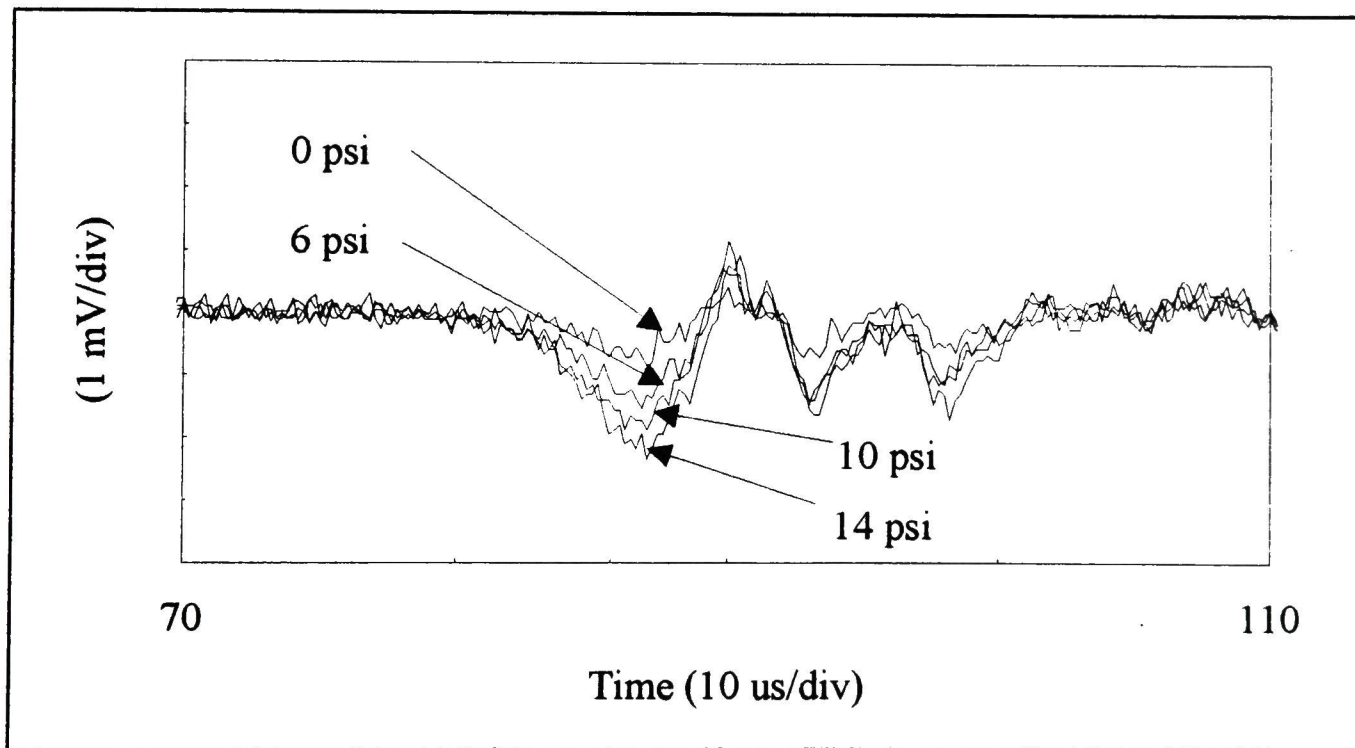


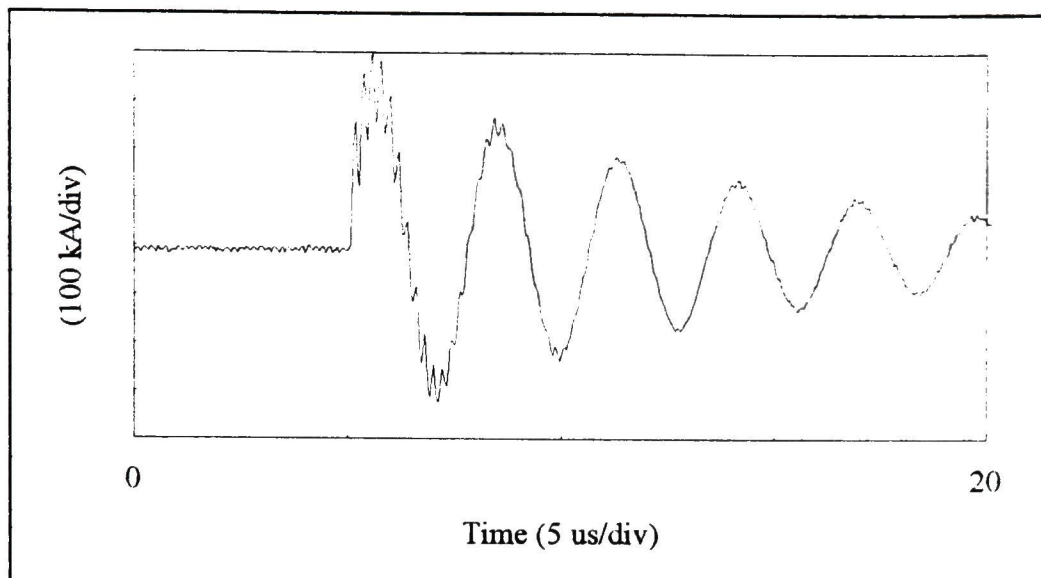
Figure 3.13 Initial Shock Pressures as a Function of Increasing Energy and Increasing Air Pressure

Table 3.6 Maximum Shock Amplitude versus Increasing Energy and Increasing Air Pressure

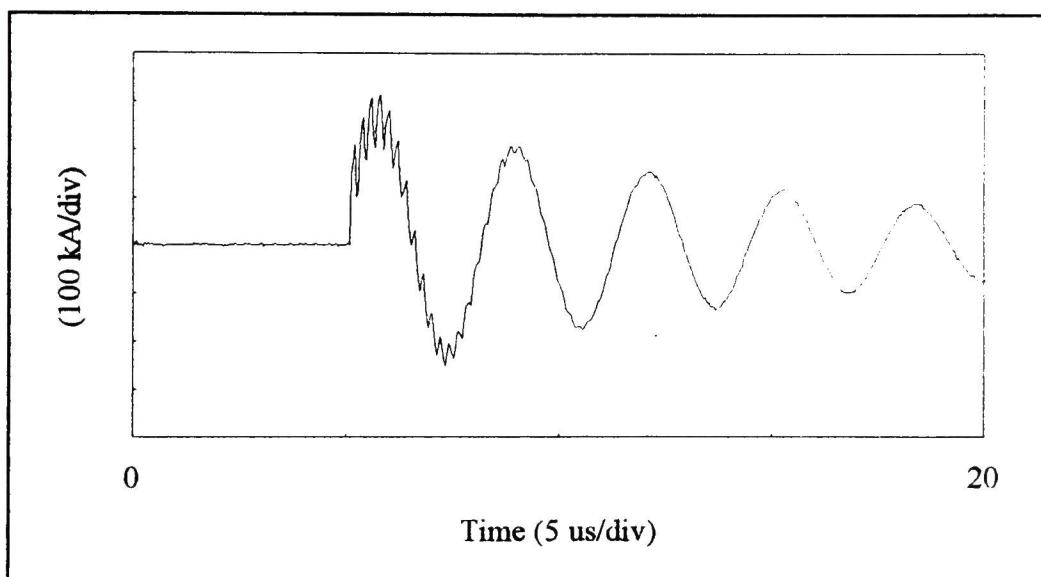
Air Pressure (psi)	Shock Amplitude (mV)	Breakdown Voltage (kV)	Input Energy (kJ)
0	.87	23	.75
6	1.3	33	1.55
10	1.88	39	2.17
14	2.35	44	2.71

3.6.3 Inductance

Pressure measurements were made on the system with two different inductance levels. Increasing the inductance decreases both the peak current and di/dt . The inductance levels are 69 nH for the shortened MJB switch and 92 nH for the original MJB switch. The measurements shown in this section were taken with the stainless steel electrode due to difficulty in aligning the ceramic delay bar in the graphite in the high inductance setup. Since both sets of data use the stainless steel electrode, the relative measurements are not affected. The maximum output current for each setup is shown in Figure 3.14. It can be seen that higher inductance increases the pulse time period and lowers the peak current. Shock pressure measurements are shown in Figure 3.15, with the gap spacing set to .3” and the air pressure set to 10 psi. Figure 3.16 is a comparison of the initial pressure waveforms from Figure 3.15. The initial wavefronts are almost identical; however, they begin to diverge at the tail end of the pulse. This effect is seen through the rest of the pulse. The reflections that occurs 100 μ s later, seen in Figure 3.17, are not as closely matched as their counterparts in Figure 3.16.



(a)

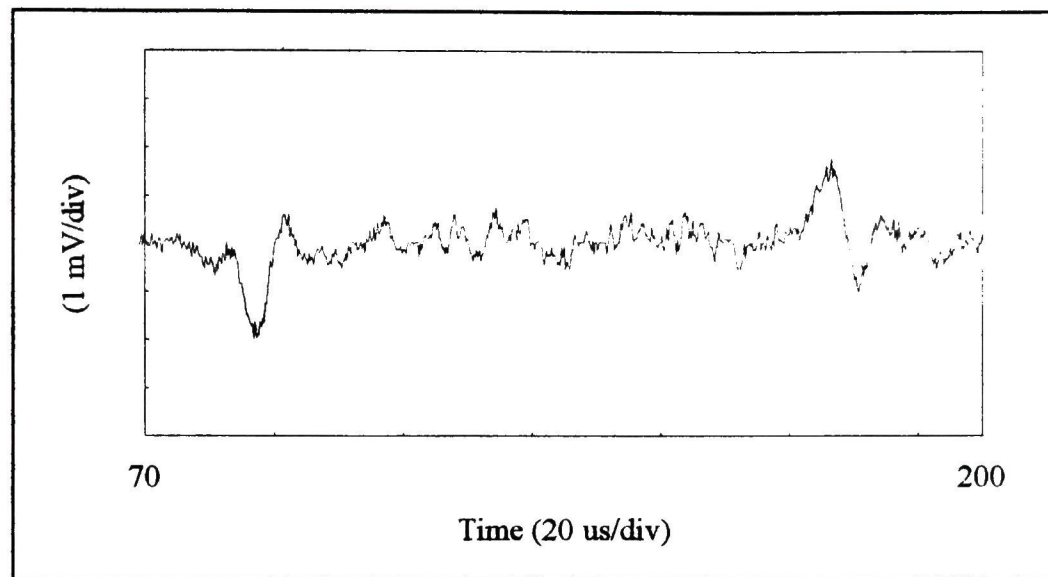


(b)

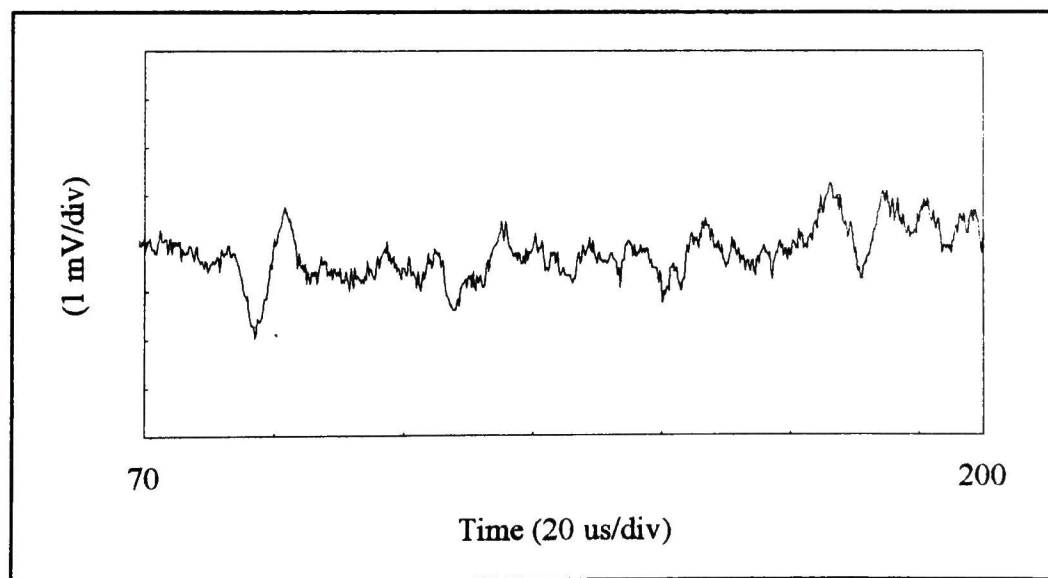
Figure 3.14 Maximum Output Current for (a) 69 nH and (b) 92 nH Inductance Circuits

The peak current of the lower inductance shot is 15% larger than that of the higher inductance shot, but it does not create a discernible difference in the initial pressure amplitudes shown in Figure 3.16. However, a 14% increase in voltage in Figure 3.11 produced a small, but noticeable change in pressure magnitude. It can be concluded that the peak voltage, or energy, affects the shock pressure while the peak current does not

The initial pressure waveforms are very similar. The slope of the lower inductance shot appears to be slightly steeper than the slope of the higher inductance shot, but this could be attributed to the noise in the signals. It is intuitive that since the lower inductance shot produced the faster current risetime, the shock wavefront would be faster as well. However, there is not enough of a difference to conclusively state that inductance is a factor.



(a)



(b)

Figure 3.15 Measured Shock Pressures for Inductances of (a) 69 nH and (b) 92 nH

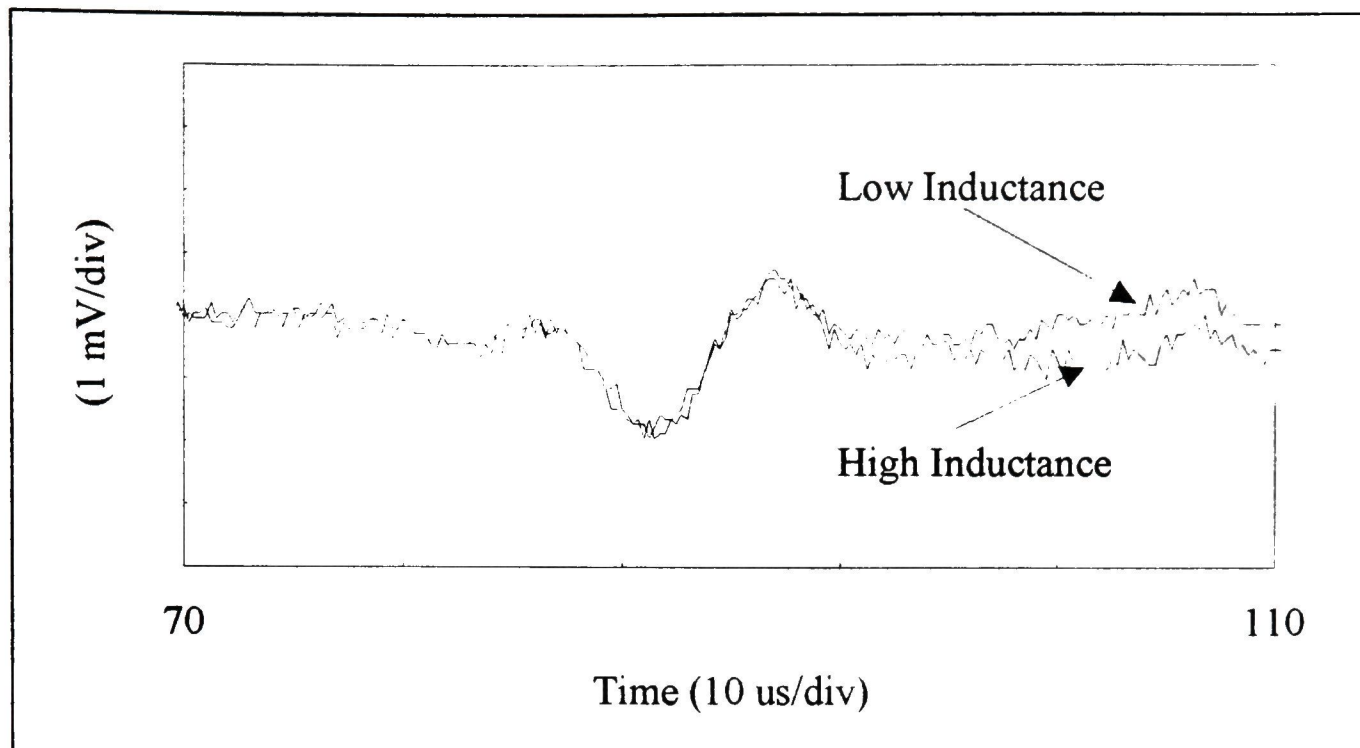


Figure 3.16 Initial Shock Pressures as a Function of Inductance

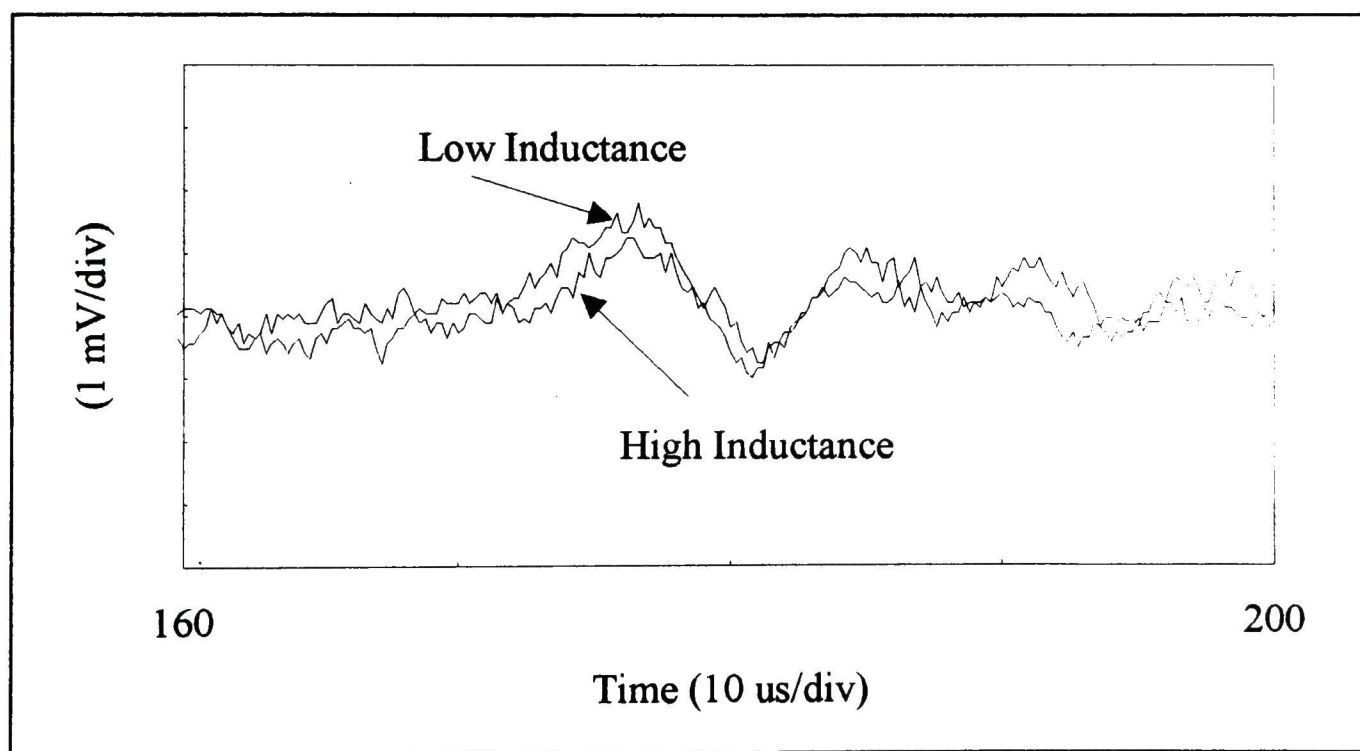


Figure 3.17 Pressure Reflections of Initial Pulses

3.6.4 Magnetic Pulse Shaping

The principle of magnetic pulse shaping, or magnetic delay, with saturable inductors has found various applications. Saturable inductors can be used as primary switches, if a small amount of leakage current can be tolerated [32]. Studies have shown that using magnetic delay in tandem with spark gaps have significantly reduced electrode erosion [33]. It has also been paired with vacuum tubes and thyratrons to improve the jitter and

initial turn-on characteristics of the devices [34, 35]. These improvements enhance the reliability and increase the lifetime of these switches. Magnetic delay lines can also be used for pulse sharpening or in stages for pulse compression [36]. For this experiment, a saturable inductor is used to delay the full conduction current through the switch for a preset amount of time.

There can be several effects on the shock pressure created by the delay in the current. First, the shock pressure wavefront can be delayed by the same amount of time as the current, with the amplitude unaffected. The amplitude can be drastically reduced by the low initial current. The shock wavefront slope can be increased since the magnetic delay produces pulse sharpening after the initial delay.

For this experiment, a saturable inductor (an inductor with magnetic material) is placed in series with the spark gap. The nonlinearity of the magnetic material is utilized to create a switching action from a high impedance to a low impedance when the core saturates. The change to a low impedance can be predicted if switch holdoff voltage is known, along with the type and geometry of the magnetic material. Therefore, a saturable inductor may be tailored for an individual circuit to limit the current flow until a preset delay time.

The delay time is the amount of time it takes for the magnetic material to saturate. It is determined from Faraday's law to be

$$t_{\text{delay}} = N \frac{A \Delta B}{V_{\text{inductor}}}, \quad [3.14]$$

where N = number of turns of the inductor, A = inductor cross-sectional area, ΔB = maximum flux density of the core, and V_{inductor} = inductor voltage. The cross sectional area can be increased by stacking cores in a series arrangement. The flux density swing is dependent on the type of material. Ferrites have a lower overall flux swing than ferromagnetic materials, so a larger cross-sectional area is required. This experiment does not have a volume constraint, so using available ferrites is not a problem. The high current is only passed through the center of the ferrites once, so the number of turns is one.

Figure 3.18 shows how the magnetic delay is incorporated into the existing setup. The saturable inductor is created by extending two of the four cable connectors out of the switch, placing a stack of ferrites around each, and returning the current on the outside of the ferrites. The other two returns are not used because of limited space at the top of the switch housing.

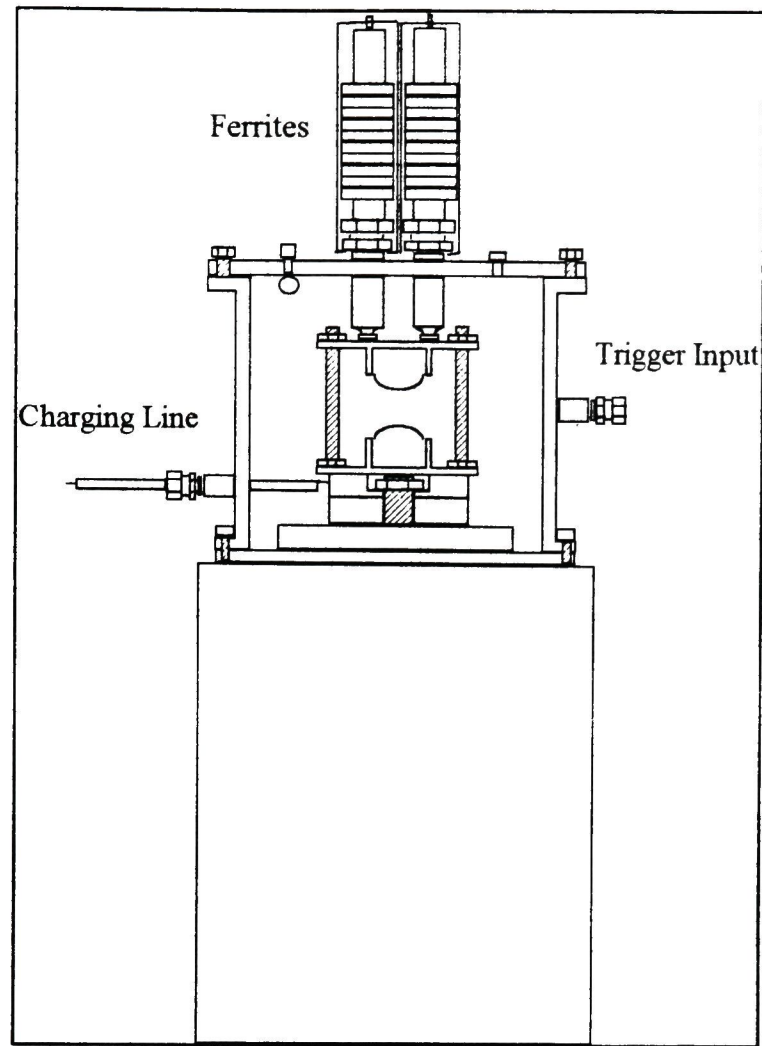
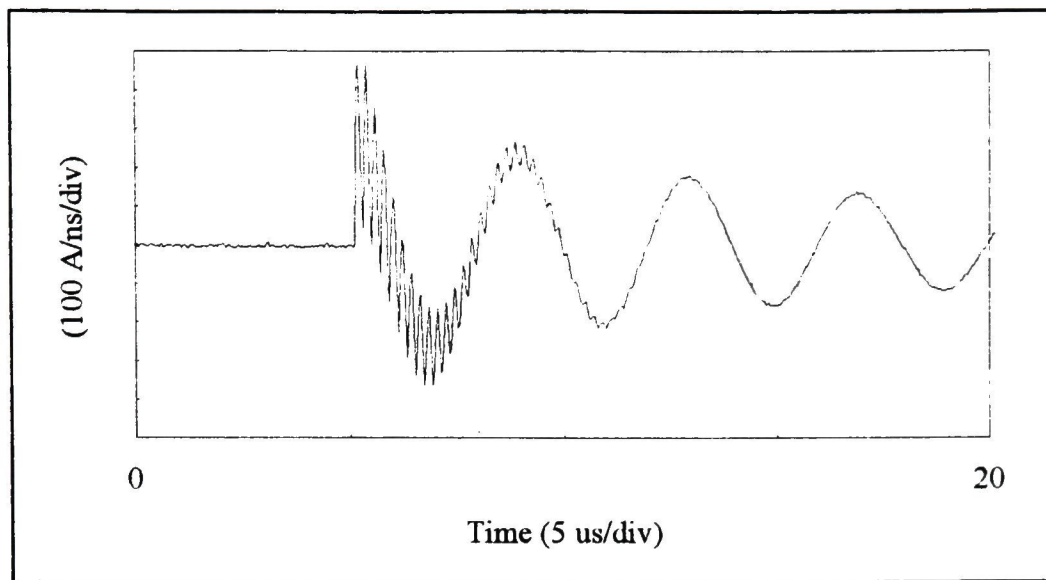
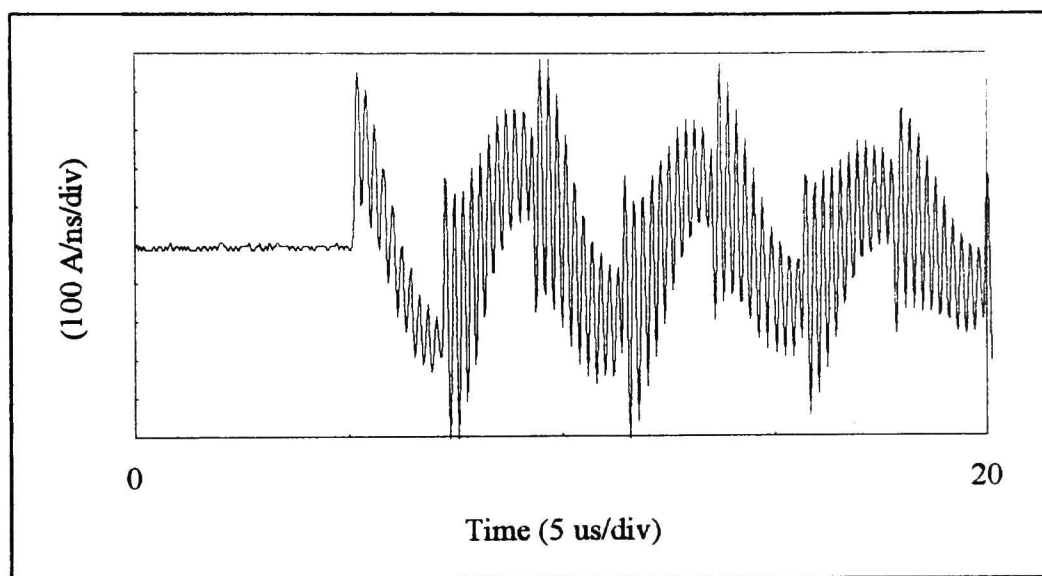


Figure 3.18 MJB Switch Modified to Incorporate the Magnetic Delay

B-dot measurements were taken to determine the amount of time delay. Although current measurements would have worked as well, there were oscilloscope triggering problems with the integrated current signal at faster time divisions. Figure 3.19 shows the B-dot signals, which are the true measurements of the current derivative, as opposed to the definition in Chapter 1. When the current returns were extended out of the switch housing, as shown in Figure 3.18, ringing appeared in the current derivative signal. The ringing did not attenuate when the ferrites were added, but became worse. The time period of the oscillations are approximately 200 ns.



(a)



(b)

Figure 3.19 B-Dot Measurements (a) without Magnetic Delay and (b) with Magnetic Delay

Figure 3.20 compares two similar shots to show that the time delay is consistent. The expanded current derivative signals are shown with and without magnetic delay in Figure 3.21. As the breakdown voltage is increased from Figure 3.21a to Figure 3.21d, the amount of time delay decreases. This corresponds to the relationship in Equation [3.14]. The estimated time delays versus the approximate measured time delays for a total of twenty-five stacked ferrites are listed in Table 3.7. The calculated values are low, but the constant used for ΔB is a rough estimate. Also, the voltage across the inductor is probably lower than the voltage dropped across the spark gap, which could account for the higher than expected values for the time delay.

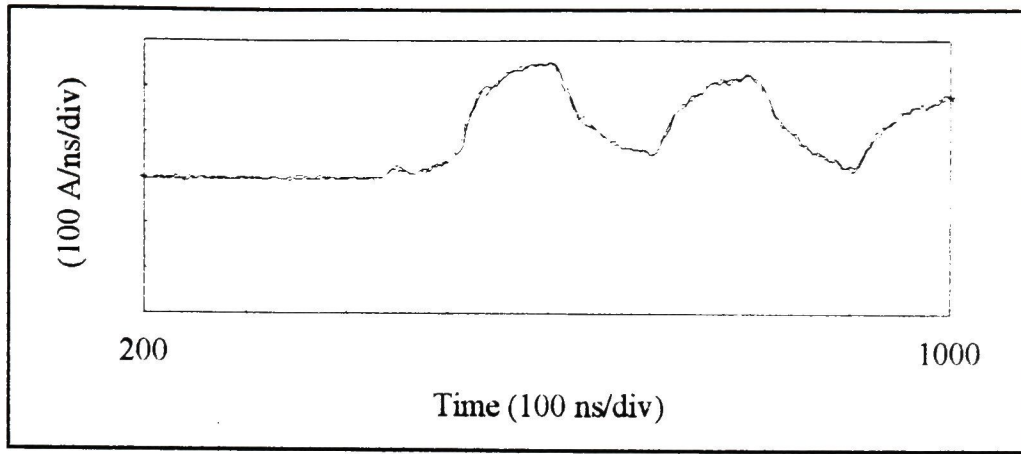
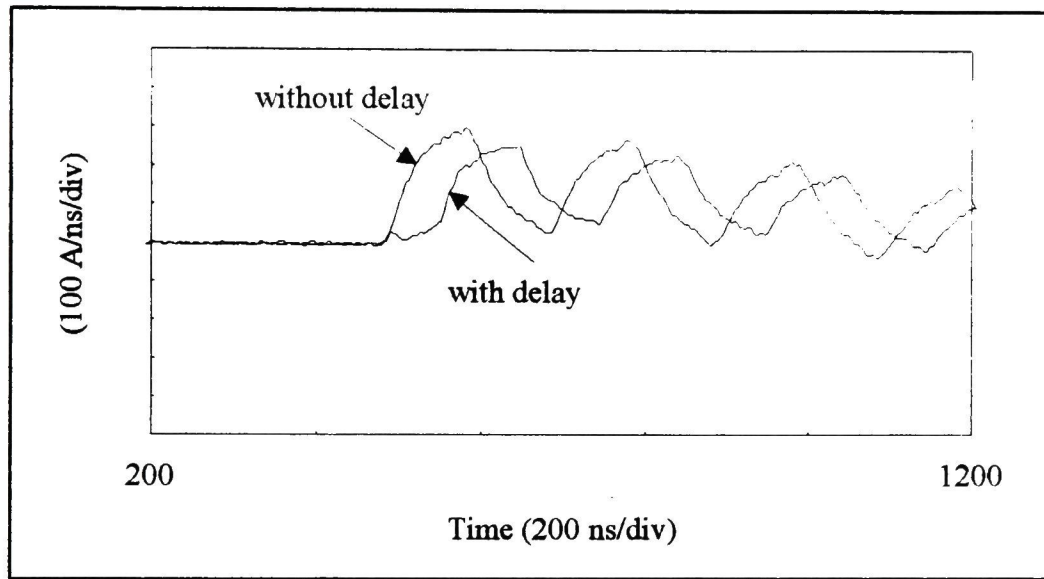
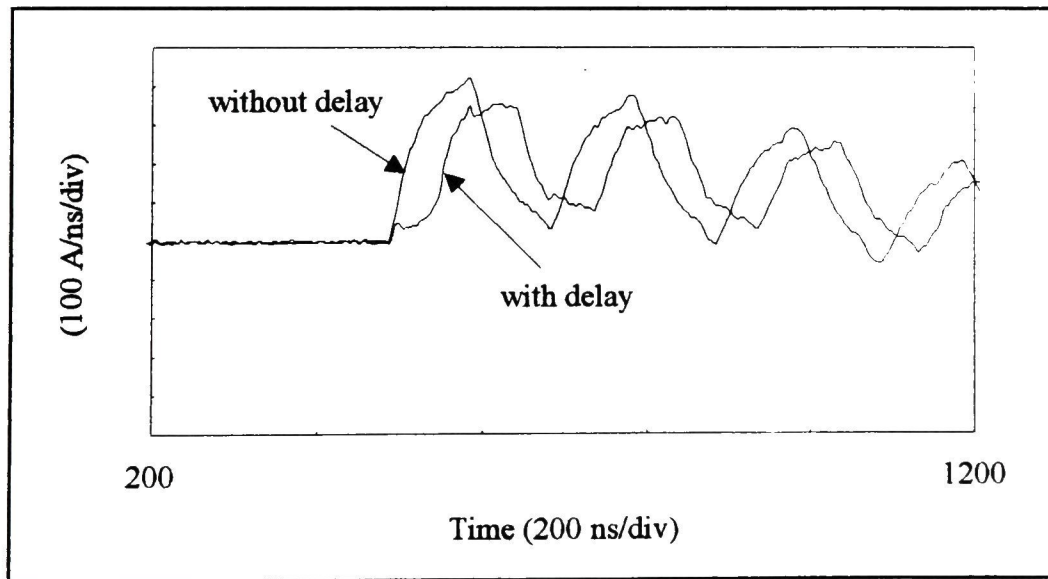


Figure 3.20 Comparison of Initial B-Dot Measurement for Similar Shots

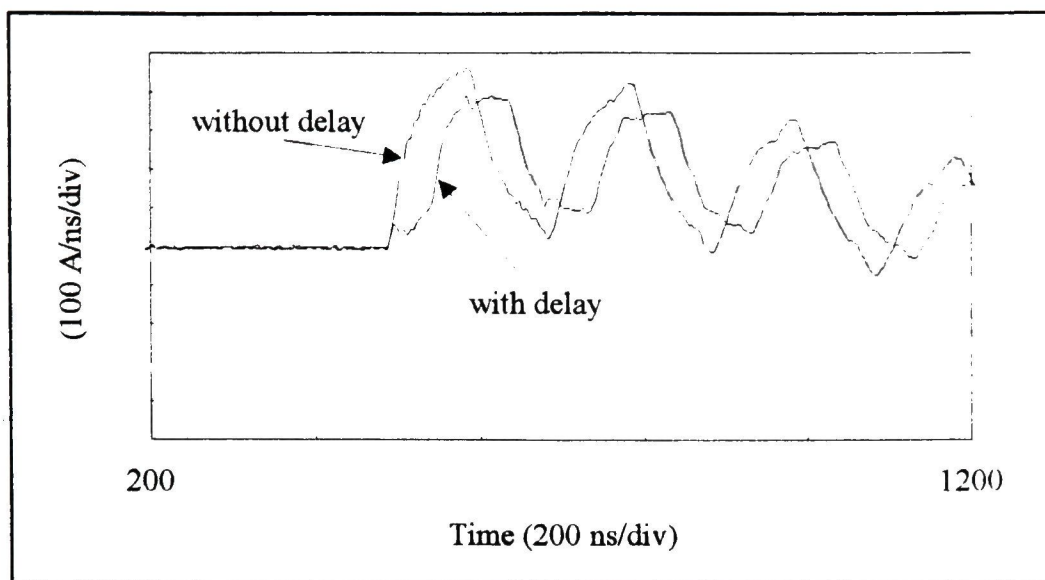


(a)

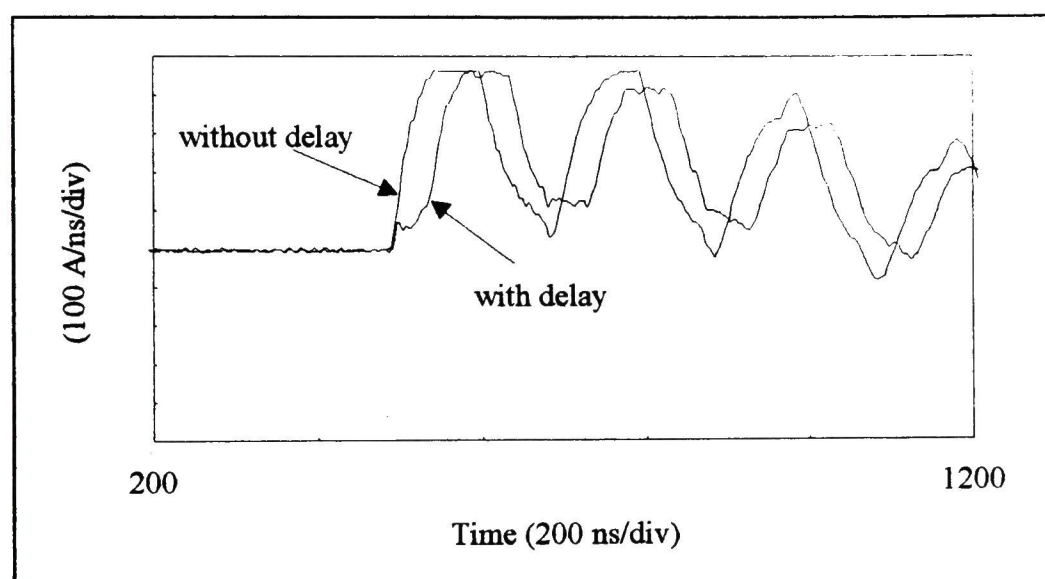


(b)

Figure 3.21 Initial B-dot Measurements with and without Magnetic Delay for Air Pressures of (a) 0 psi and (b) 6 psi



(c)



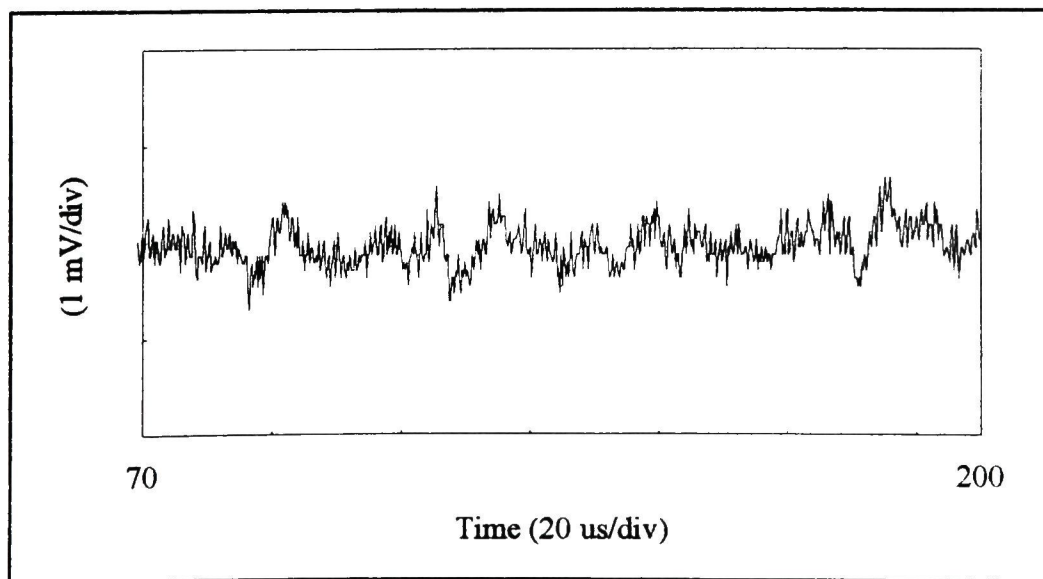
(d)

Figure 3.21 continued. Initial B-dot Measurements with and without Magnetic Delay for Air Pressures of (c) 10 psi and (d) 14 psi

Table 3.7 Estimated Time Delays versus Measured Time Delays

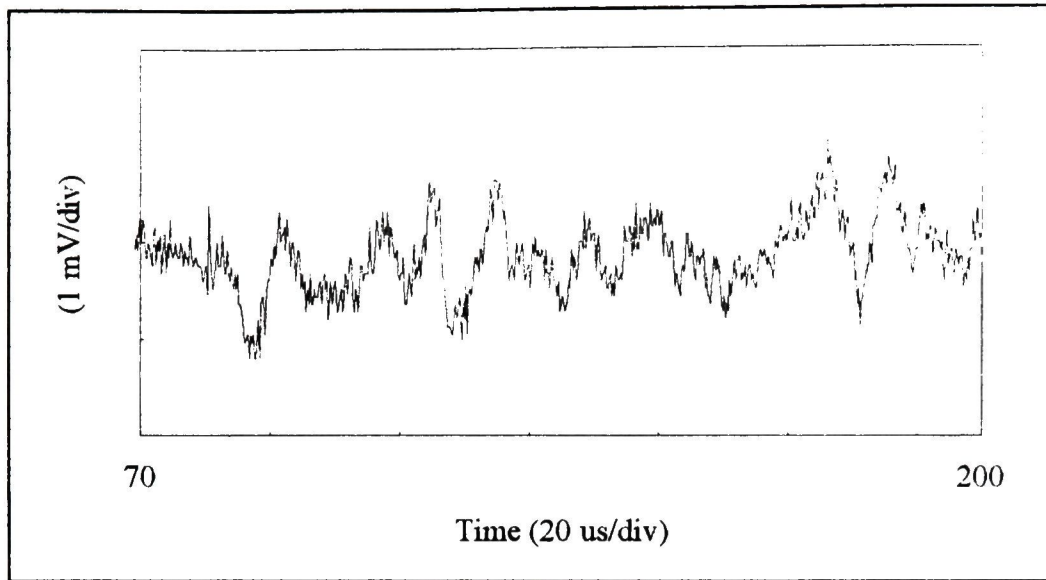
Breakdown Voltage (kV)	Estimated Delay (ns)	Measured Delay (ns)
24.2	53.6	70
33.3	39.0	50
37.1	35.0	50
44.2	29.3	40

Figure 3.22 shows the strain gage measurements corresponding to the time delayed b-dot measurements in Figure 3.21. In Figure 3.23, the initial shock fronts are expanded and compared to similar pressure shots with no delay. Surprisingly, there is virtually no difference in pressure magnitude or waveform in the delayed versus non-delayed signals. Also, there is no significant delay in the onset of the pressure signal to show that the wavefront is delayed by the amount of time as the peak current.

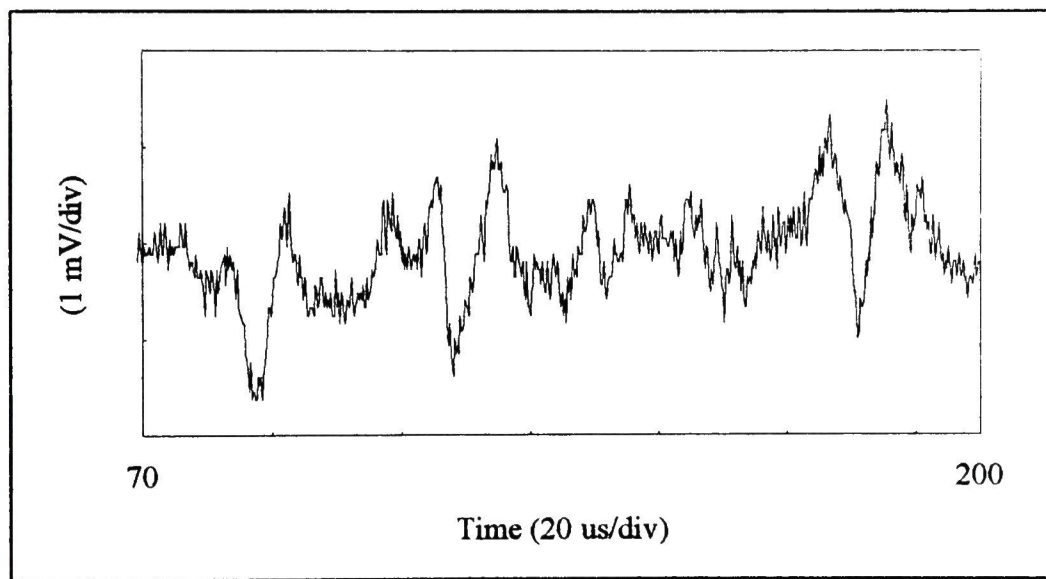


(a)

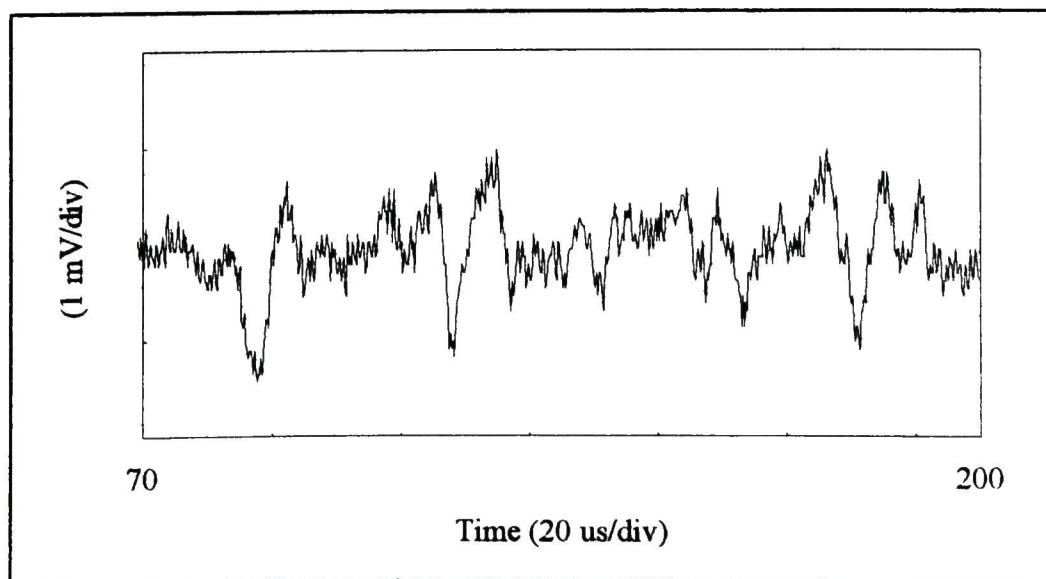
Figure 3.22 Measured Shock Pressure with Magnetic Delay and Air Pressures of (a) 0 psi



(b)

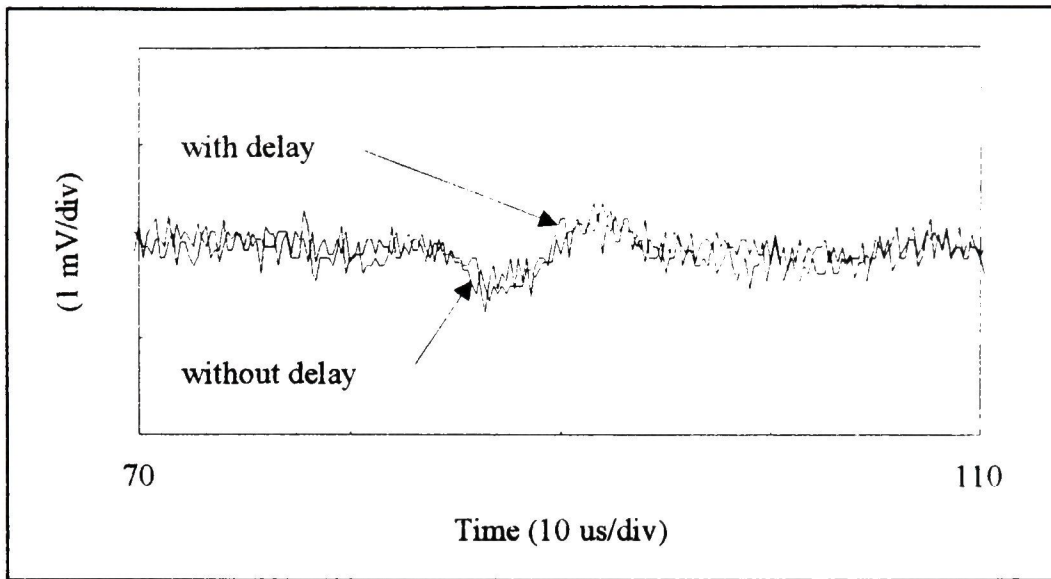


(c)

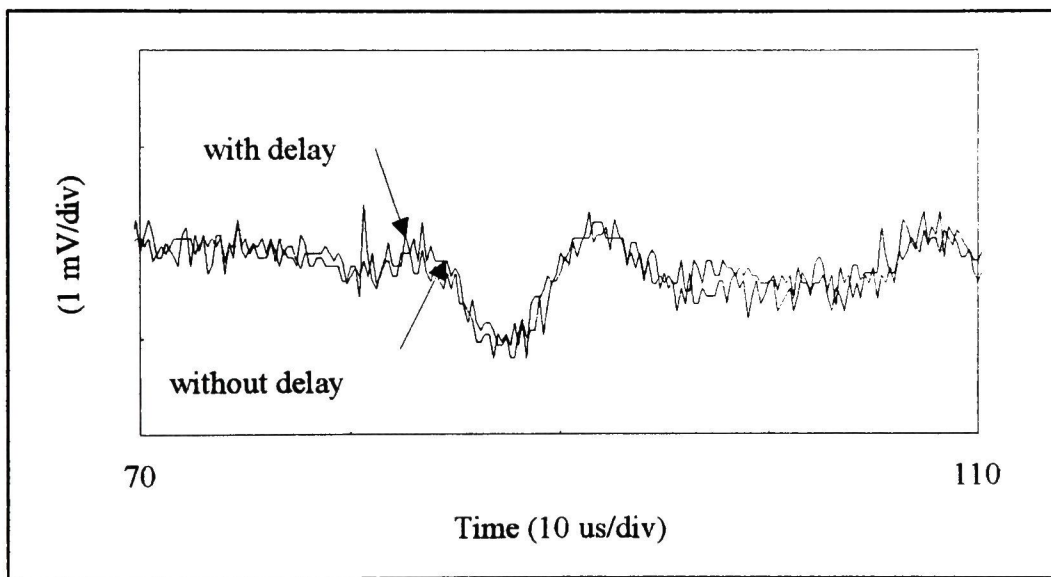


(d)

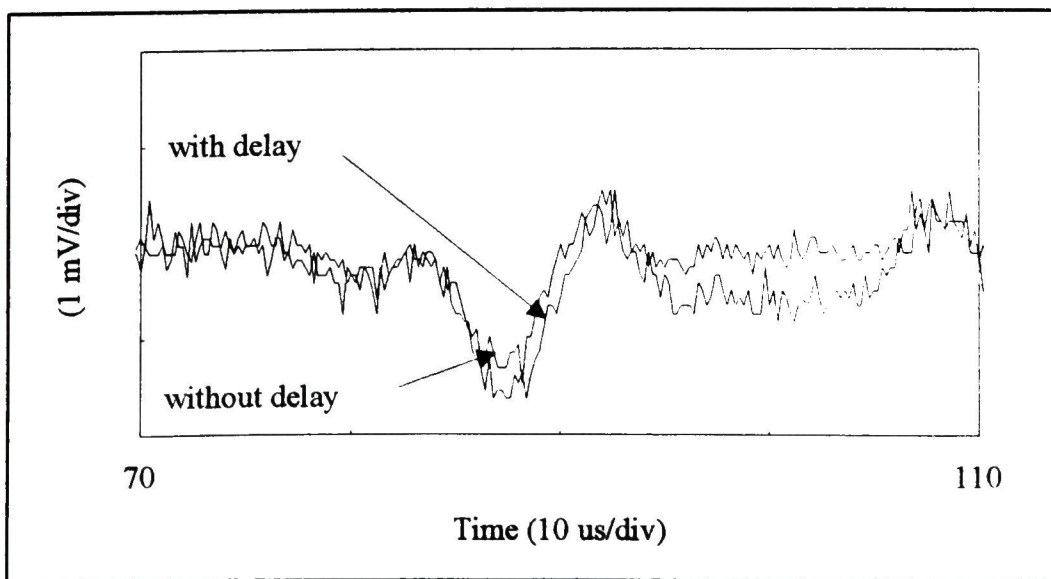
Figure 3.22 continued. Measured Shock Pressure with Magnetic Delay and Air Pressures of (b) 6 psi, (c) 10 psi, and (d) 14 psi



(a)

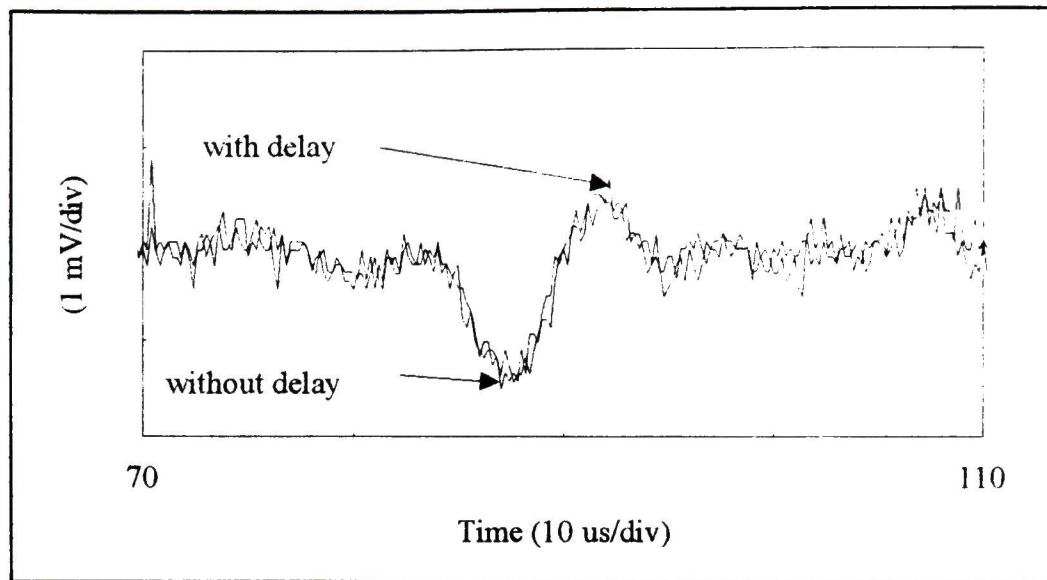


(b)



(c)

Figure 3.23 Initial Shock Pressure with and without Magnetic Delay with Air Pressures of (a) 0 psi, (b) 6 psi, and (c) 10 psi

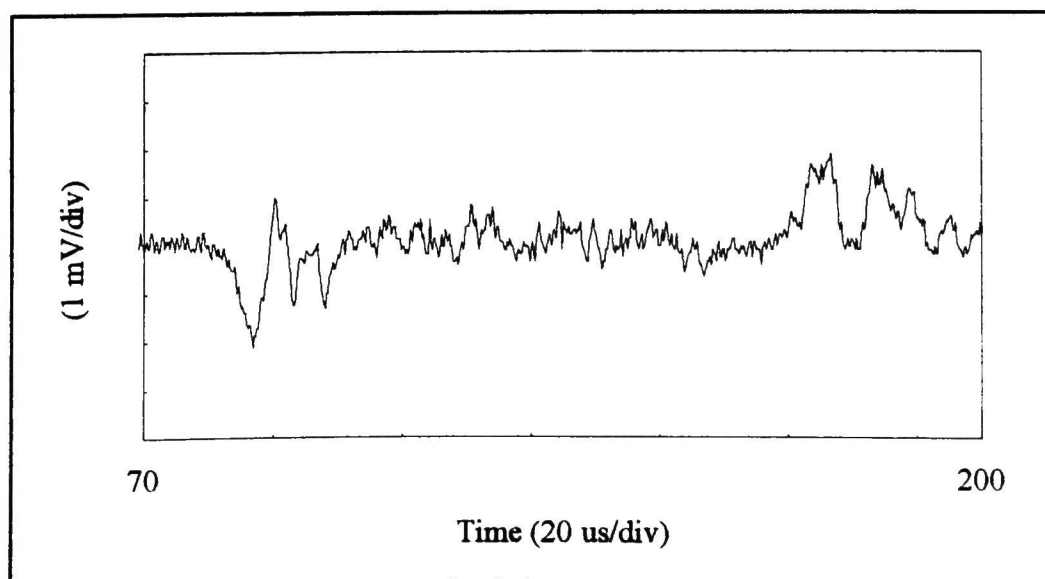


(d)

Figure 3.23 continued Initial Shock Pressures with and without Magnetic Delay with Air Pressure of (d) 14 psi

3.6.5 Graphite Electrodes versus Stainless Steel Electrodes

Pressure measurements were made for two electrode materials in the lower inductance, 5 kJ setup. Changing electrode material does not affect the initial pressure front, but it does alter the propagation through the electrode. The purpose of this part of the experiment is to see how the graphite distorts the wavefront compared to stainless steel, a common electrode material. Figure 3.24 shows the pressure measurements of graphite versus stainless steel electrodes with the gap distance set to 0.3" and the air pressure set to 14 psi. The initial pulse fronts are expanded and compared in Figure 3.25.



(a)

Figure 3.24 Measured Shock Pressure for (a) Graphite Electrode

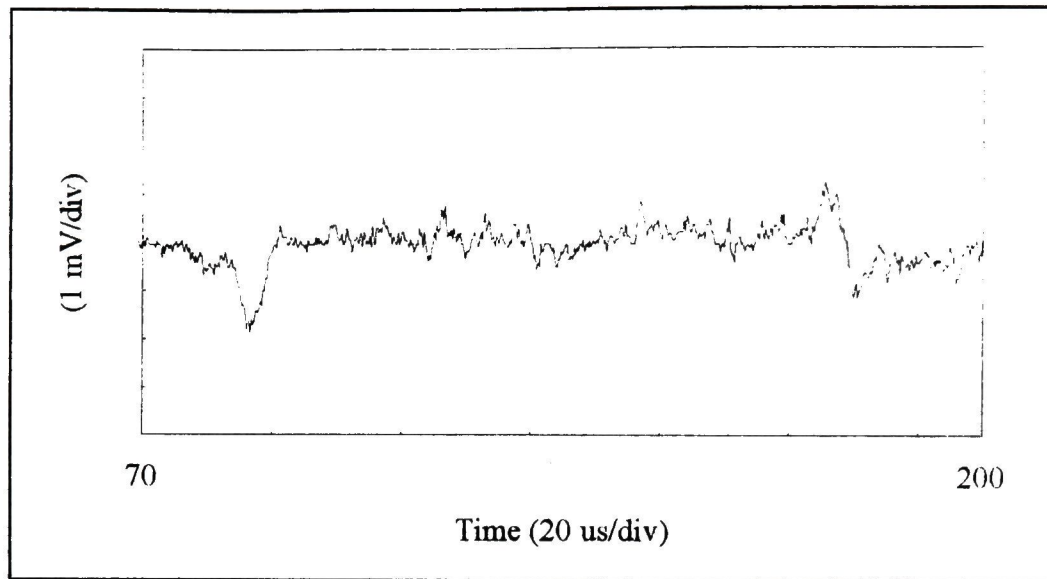


Figure 3.24 continued. Measured Shock Pressure for (b) Stainless Steel Electrode

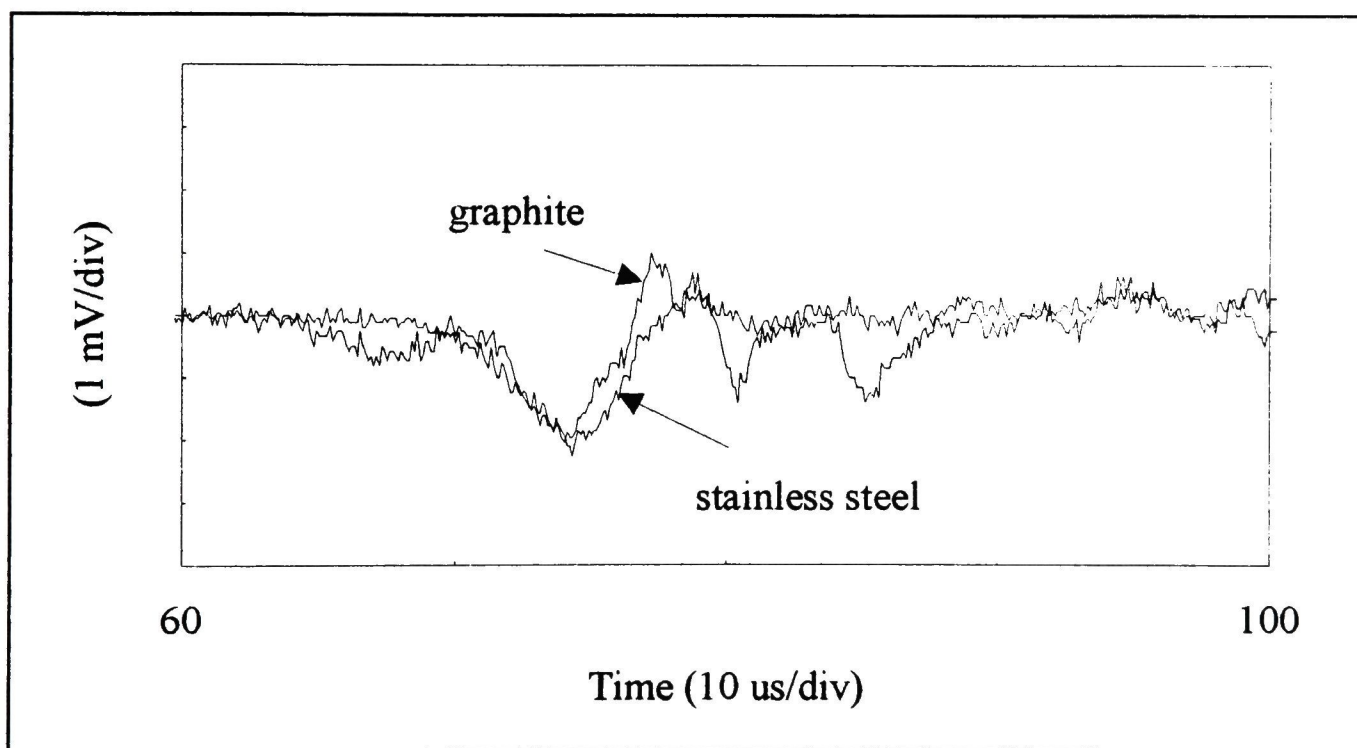


Figure 3.25 Initial Shock Pressures for Graphite and Stainless Steel

Several differences are apparent in Figure 3.25. First, the stainless steel electrode wavefront has a small initial pulse that the graphite does not have. Secondly, the pulse in stainless steel has a steeper initial slope, which probably means that it absorbs less of the energy than the graphite.

Lastly, the graphite waveform has two smaller pulses immediately following the first pulse that the stainless steel does not. It is shown in Chapter 4 that the pulse does not refract significantly in the stainless steel electrode, but does in the graphite electrode. This is due to the difference in propagation velocity in the two materials. When the wave

refracts in the graphite, the pulse is divided into longitudinal and shear waves. The shear wave travels at nearly half the speed of the longitudinal wave; however, it will not be delayed for a significant amount of time because the distances in the electrode are fairly short. Since the pressure pulse is not refracted in the stainless steel, there is no shear component.

CHAPTER 4

ANALYSIS AND THEORETICAL MODELING

This chapter will be divided into three main sections: analysis of the pressures generated in the spark gap, Mathcad analysis of stress propagation in the electrode, and PSPICE modeling of the pressure propagation through the electrode and ceramic delay bar. The first section includes calculations of the magnetic pressure on the surface of the electrode, and calculations of the shock pressure based on Engel's model of the arc channel radius in Chapter 2. In the second section, Gracewski's model of a diverging acoustical pulse propagating through a sphere is modified to fit the geometry of the electrodes in this experiment. The shock front is modeled as a diverging spherical wave and also as a cylindrical wave that propagates through the electrode. For simplicity, only the longitudinal component of the traveling wave will be shown. Because of the duality of electrical and acoustical parameters, PSPICE can be used to model an acoustic transmission line in the same way it models an electrical one. The shock pressure generated in the first section is modeled as a piecewise linear voltage source, and a voltage probe is used in place of the strain gage in the schematic. The graphite electrode and ceramic delay bar are modeled as transmission lines with characteristic impedances and one-way transmission times.

4.1 Analysis of Switch Pressures

The pressures generated by the high magnetic field and the shock wave are calculated. For both sets of calculations, the maximum pressures are determined, which corresponds to a charging voltage of 50 kV in the experimental setup. It will be shown that the shock pressure is significantly higher than the magnetic pressure, and therefore is the dominant pressure mechanism. The Mathcad file of the shock pressure analysis is listed in the Appendix.

4.1.1 J x B Force

As mentioned in Chapter 2, it is not a trivial problem to calculate the magnetic pressure on the surface of the electrode. The rough approximation given in this section will yield the highest possible value for the magnetic pressure. It will be shown that even for the "worst - case" approximation, the magnetic pressure is much lower than the shock pressure. Figure 4.1 shows how the current density in the electrode tip in the vicinity of the arc and the magnetic field of the arc combine to create a force on the electrode.

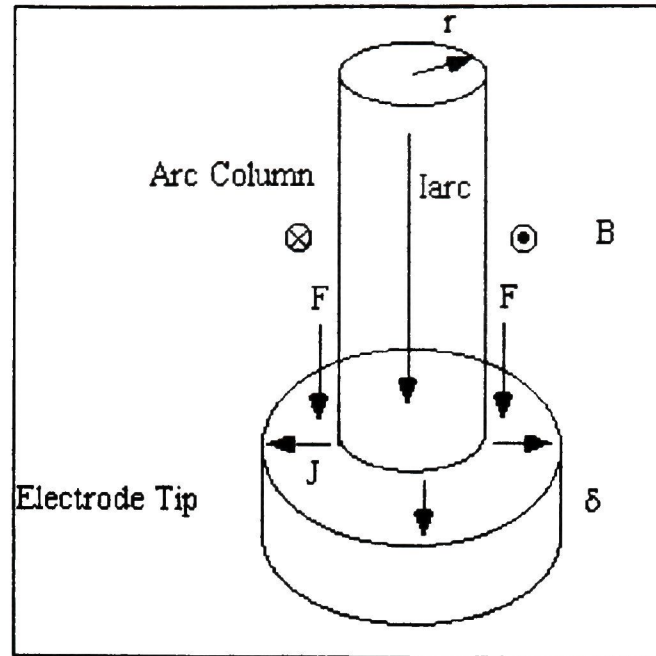


Figure 4.1 $J \times B$ Force at Electrode Tip

In the immediate vicinity of the arc, the current travels in the electrode through a cross-sectional area of

$$A = 2\pi r \delta, \quad [4.1]$$

where r = arc radius and δ = skin depth. In the next section, the arc radius is calculated to be approximately 0.004 m. From Equation [2.6], the skin depth is calculated to be 0.0045 m. Substituting these values into Equation [4.1], the cross-sectional area of current flow at the tip of the electrode is $113.1(10^{-6}) \text{ m}^2$. The current density decreases exponentially as it penetrates into the electrode, and there is no significant current flow at a depth of 2δ from the electrode surface. Taking the exponential decay into account, the current density is defined as

$$J = J_0 e^{-\frac{z}{\delta}}, \quad [4.2]$$

where J_0 = maximum current density, and the total current is defined as

$$I = \int_0^{\delta} \int_0^{2\pi} J_0 e^{-\frac{z}{\delta}} r d\Phi dz, \quad [4.3]$$

where $r d\Phi dz$ = differential cross-sectional area in cylindrical coordinates. By substituting the maximum current, $I = 320 \text{ kA}$, into Equation [4.3], the value for J_0 is calculated to be 20.2 MA/m^2 . Assuming the arc is perfectly cylindrical, the maximum magnetic flux density of the arc is

$$B = \frac{\mu_0 I}{2\pi r}, \quad [4.4]$$

where r = arc radius. Substituting $I = 320$ kA, and $r = 0.004$ m into Equation [4.4], the maximum flux density is 16 T. The maximum magnetic force density is

$$f_{mag} = J_0 \times B. \quad [4.5]$$

It can be seen from Figure 1, that the current density flows in the radial direction and the magnetic flux from the arc flows in a circumference around the arc. Addressing the problem in cylindrical geometry, the force density is pointed in the axial direction. Therefore, the magnitude of the force density from Equation [4.5] is $323.2(10^6)$ N/m³, and the direction is normal to the electrode surface. The maximum magnetic pressure, which is calculated by

$$P_{mag} = f_{mag} \delta, \quad [4.6]$$

is $1.45(10^6)$ Pa. Considering this to be a maximum value of a “worst-case” scenario, the magnetic pressure is still three orders of magnitude lower than the shock pressure calculated in the next section.

4.1.2 Shock Wave Pressure

Figures 4.2 - 4.4 show the maximum arc radius, expansion velocity, and arc pressure that were calculated in Mathcad based on Engel’s equations in Chapter 2. The arc radius, expansion velocity, and shock pressure are calculated up to 1 μ s. Figures 4.2 - 4.4 show the arc parameters for the maximum charging voltage. The analysis was run for a range of charging voltages, and the values of the corresponding peak shock magnitudes are listed in Table 4.1.

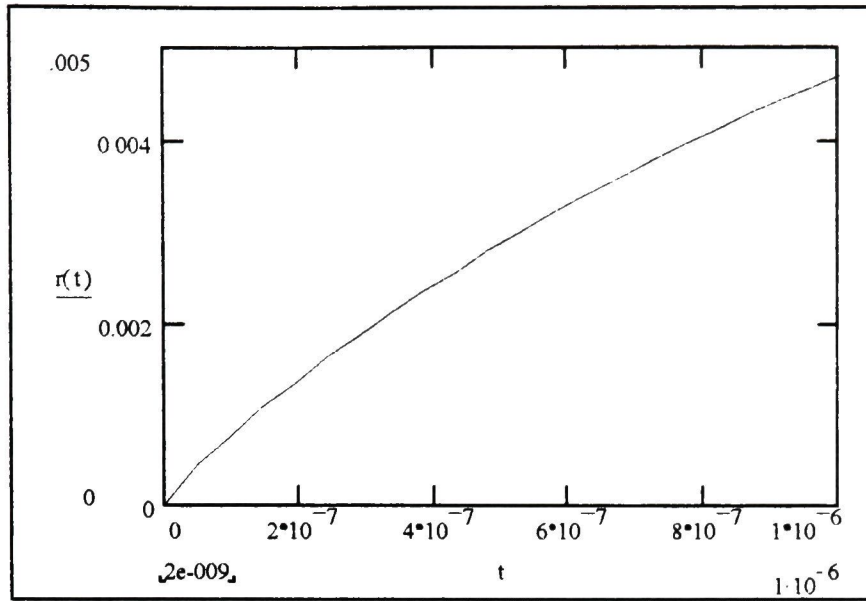


Figure 4.2 Maximum Arc Radius

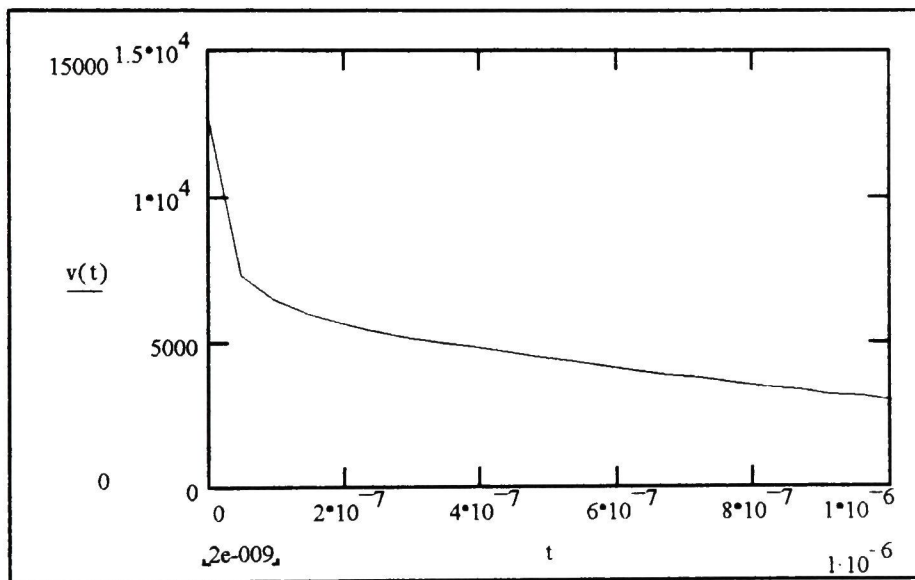


Figure 4.3 Maximum Arc Expansion Velocity

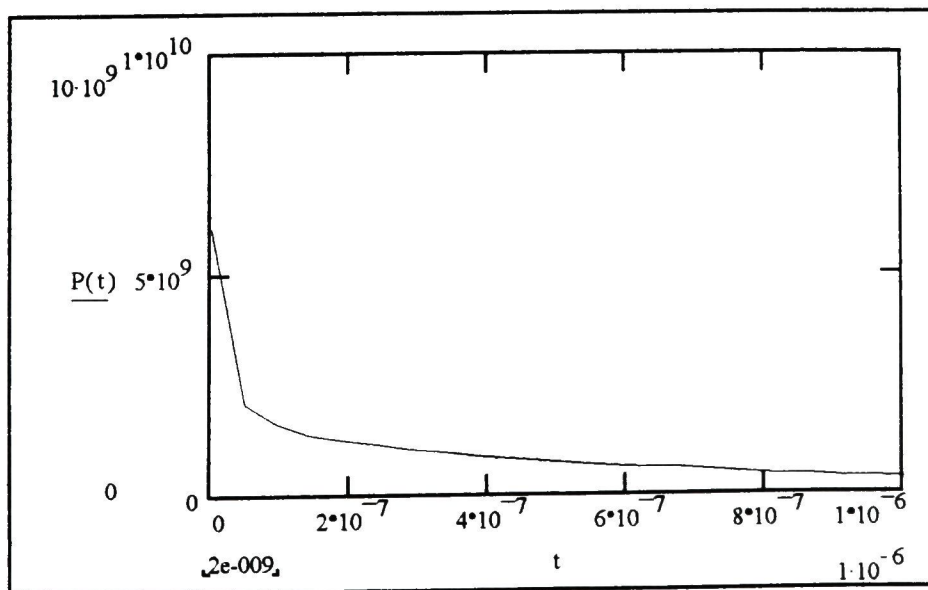


Figure 4.4 Maximum Shock Pressure

Table 4.1 Peak Shock Pressure versus Charging Voltage

Charging Voltage (kV)	Shock Pressure (GPa)
20	3.29
30	4.31
40	5.22
50	6.06

4.2 Stress Wave Propagation in the Electrodes

The propagation of the shock pulse through the electrodes is complicated by the spherical geometry of the electrode. An analysis is performed for a spherical shock front and a cylindrical shock front. The maximum shock wave radius is substantially smaller than the electrode radius. Since the shock wave contacts a small portion of the electrode surface, it seems intuitive that the curvature of the surface would be negligible. However, the following Mathcad analysis shows that the pressure propagation is highly geometry dependent.

Gracewski's model of a spherical shock propagating through a spherical solid was modified to analyze the direction of the shock propagation through the electrode. Only the direction is analyzed, and not the magnitude. It was necessary to modify the model because the electrode is not entirely spherical. Only the electrode tip is spherical, and the base is cylindrical. The electrode is a total of 1.75", or 4.45 cm, long, with the hemispherical tip being half of that length. Since the model of propagation was based on ray-tracing techniques, it was not too difficult to modify the model to account for the cylindrical base. The propagation is plotted in two dimensions, and the equations for the change in direction are given in x and y coordinates. Although the equations are listed here, the Mathcad files are included in the Appendix.

For the spherical shock front, the wavefront originates at the shock focal point, which is assumed to be the midpoint between the electrodes. As the wave diverges, it impacts the spherical electrode tip at an oblique angle, which causes the wave to refract in

the electrode. The refracted wave has longitudinal and shear components; however, only the longitudinal component is plotted.

The following equations calculate the horizontal and vertical positions of the traveling longitudinal wavefront through the geometry shown in Figure 4.5. Due to the symmetry of the problem, the propagation is determined on one side of the horizontal axis only. Likewise, since the pressure is the same in both electrodes, only one electrode is shown.

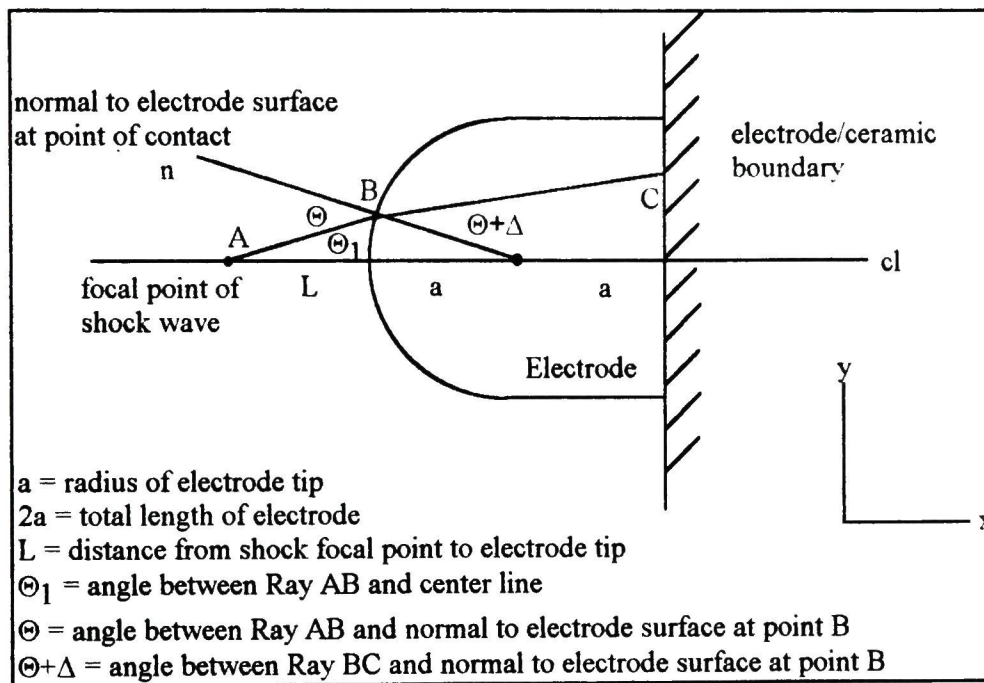


Figure 4.5 Geometry of Spherical Pressure Wave/Spherical Electrode Interaction

Point A is the focal point of the shock wave, which is assumed to be half the distance of the electrode gap spacing. The acoustic wave diverges and strikes the electrode surface at Point B. Assuming Point A is the reference point, and if the x and y coordinates of Point B are known, then Ray AB may be plotted. The angle Θ₁ between Ray AB and horizontal axis is

$$\Theta_1 = \arctan\left(\frac{y_B}{x_B}\right), \quad [4.7]$$

where $x_B = L$ and $y_B =$ vertical position of Point B. The angle between the normal to the electrode surface and the horizontal axis is $\Theta - \Theta_1$, which may be calculated from

$$\Theta - \Theta_1 = \arctan\left(\frac{y_B}{a}\right), \quad [4.8]$$

where a = electrode tip radius. From Equations [4.7] and [4.8], the angle Θ between Ray AB and the normal to the surface may be determined.

Ray AB arrives at Point B at time

$$t_B = \frac{x_B}{c_p \cos \Theta_1}, \quad [4.9]$$

where c_p = propagation velocity of the shock wave, at which point it is refracted in the electrode. The direction of propagation is altered by angle Δ , according to Snell's law. The angle Δ is calculated by

$$\frac{1}{c_s} \sin(\Theta + \Delta) = \frac{1}{c_p} \sin \Theta, \quad [4.10]$$

where c_s = velocity of propagation in the electrode. The position of the longitudinal wavefront in the electrode is now

$$x_{BC} = x_B + (t - t_B)c_s \cos(\Theta_1 + \Delta). \quad [4.11]$$

$$y_{BC} = y_B + (t - t_B)c_s \sin(\Theta_1 + \Delta). \quad [4.12]$$

It reaches the surface or the back of the electrode at time

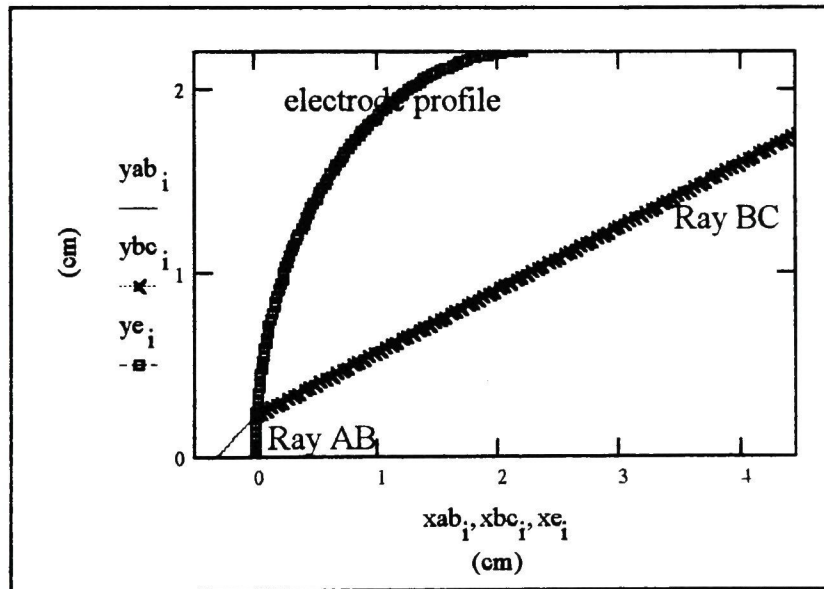
$$t_C = t_B + \frac{2a}{c_s} \cos(\Theta + \Delta), \quad [4.13]$$

where it is then reflected. In the analysis, the wavefronts reached the back surface of the electrode before it reached the side, so the analysis was concluded at this point.

Figure 4.6 shows the spherical wavefront positions in the graphite electrode as a function of gap spacing. As in the experiment, the gap distances used in the model are 0.25", 0.3", 0.4", and 0.5". Figure 4.7 shows the wavefront position in the stainless steel electrode with a gap distance of 0.5". The wavefront direction differs in graphite and stainless steel because their propagation velocities are different, and this affects the refraction in the material. The shock wave radius is assumed to be .4 cm, which is approximately the maximum radius determined from the first section and shown in Figure 4.2. For clarity, the profile of the electrode is superimposed on the plots. Table 4.2 lists the function of the variables plotted in Figures 4.6 and 4.7.

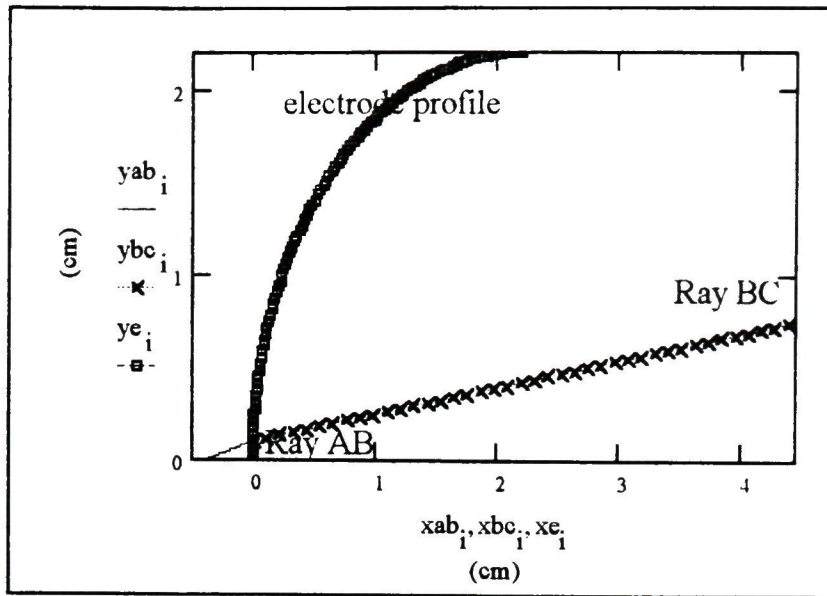
Table 4.2 List of Variables in Figures 4.6 and 4.7

Variable	Function
i	calculation increment
xab_i, yab_i	horizontal and vertical position of wavefront before it strikes the electrode surface
xbc_i, ybc_i	horizontal and vertical position of longitudinal wavefront in the electrode
xe_i, ye_i	horizontal and vertical position of the electrode profile

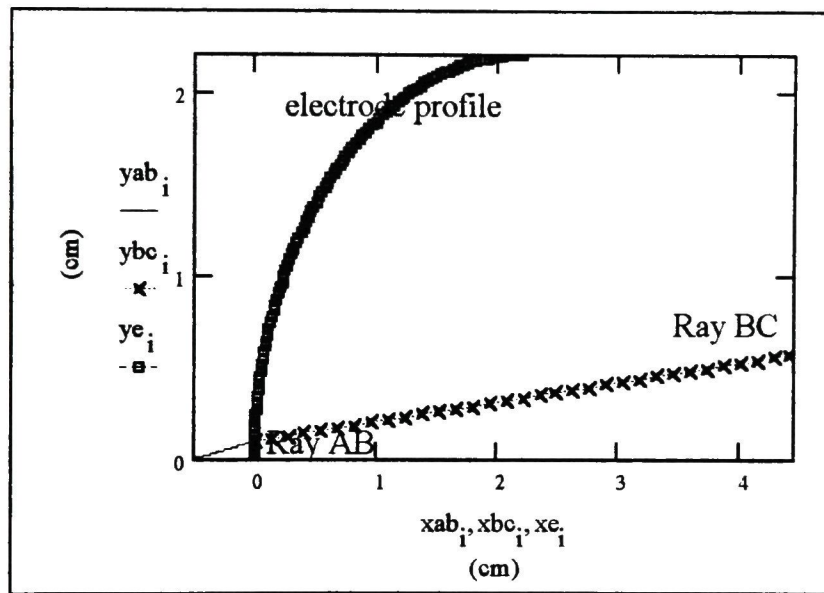


(a)

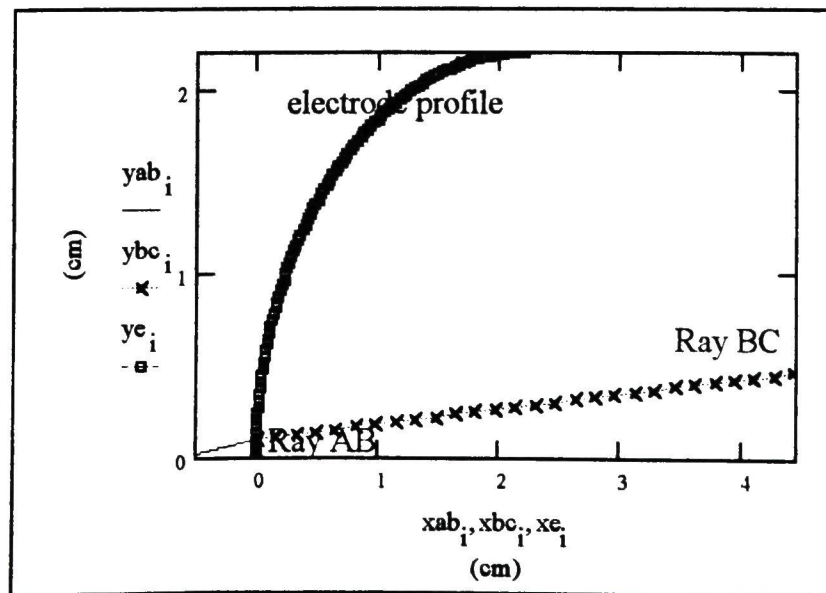
Figure 4.6 Propagation of Spherical Wavefront in Graphite Electrode for Gap Spacing of (a) 0.25"



(b)



(c)



(d)

Figure 4.6 continued. Propagation of Spherical Wavefront in Graphite Electrode for Gap Spacings of (b) 0.3" , (c) 0.4" , and (d) 0.5"

In Figures 4.6 (a) and (b), the distance between the focal point of the shock wave and the electrode tip is less than or equal to the radius of the shock wave. In Figures 4.6 (c) and (d), the distance is greater than the shock radius. As the gap spacing increases, the angle of propagation in the electrode decreases, and the longitudinal component of the propagation becomes dominant. Since the shock wave will always have a finite radius no matter how far apart the electrodes are, there will always be a shear component to the pressure propagation in a spherical electrode.

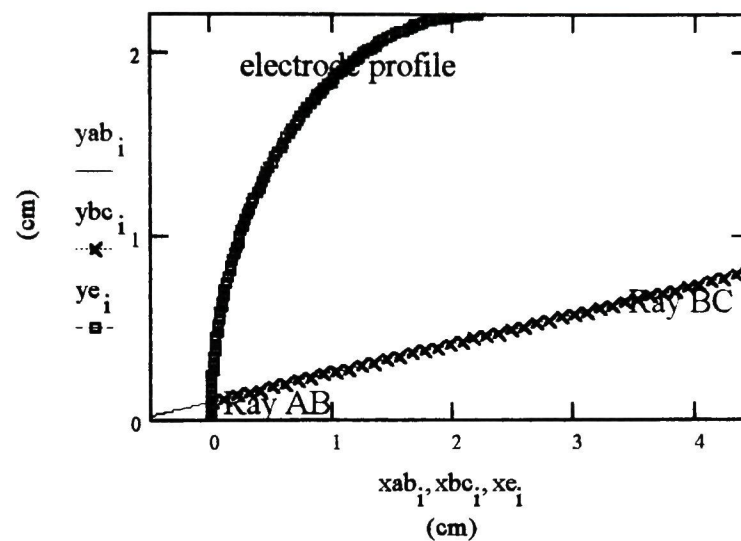


Figure 4.7 Propagation of Spherical Wavefront in Stainless Steel Electrode for Gap Spacing of 0.5"

The direction of propagation in the stainless steel does not change upon impact on the surface of the electrode. This is because the velocity of propagation for stainless steel is very close to the velocity of the shock wave in air. Although the initial shock velocity is approximately 12,000 m/s, it decreases fairly rapidly. Since it takes a finite amount of time for the shock wave to reach the electrode, a value of 5000 m/s is used in the Mathcad analysis. This is very close to the speed of sound in stainless steel, which is 4800 m/s. From Equation [4.10], if the velocities are unchanged as a wave is transmitted from one medium to another, the angle of refraction will equal the angle of incidence. This is exactly what happens in the stainless steel electrodes.

A second analysis was performed for the interaction between a cylindrical shock front and the spherical electrode. The cylindrical front has no focal point and propagates as a plane wave. Although the largest gap distance is approximately double the length of the arc radius, the shock wave probably not made the transition from a cylindrical

wavefront to a spherical one. The geometry of the cylindrical shock wave and the spherical electrode tip interaction is shown in Figure 4.8.

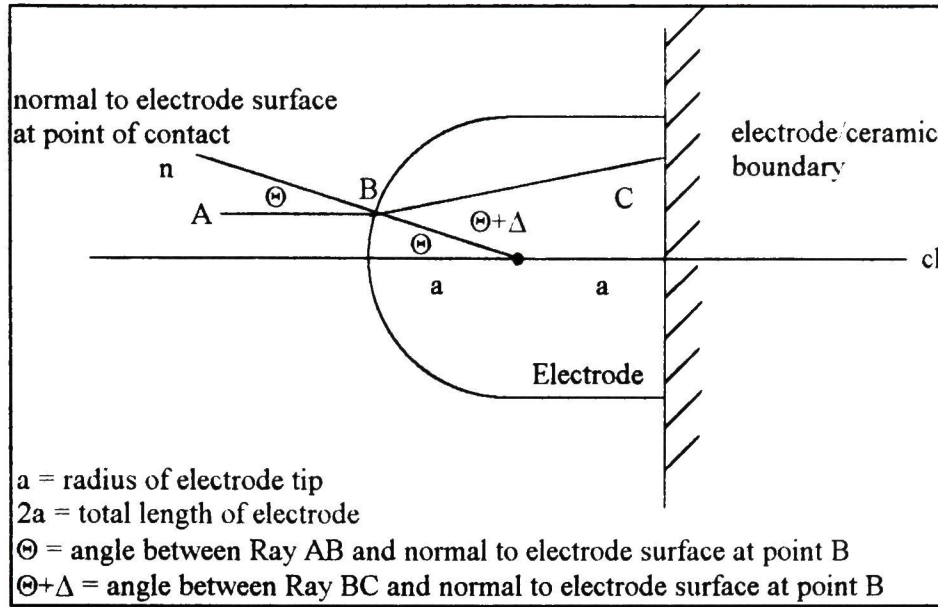


Figure 4.8 Geometry of Cylindrical Pressure Wave/Spherical Electrode Interaction

The cylindrical wave propagation through the electrode is more simple than the spherical propagation, and is determined by the following equations. The angle Θ between Ray AB and the normal to the surface is

$$\Theta = \arctan \left(\frac{y_B}{x_B} \right), \quad [4.14]$$

where y_B = arc radius and x_B = electrode tip radius (approximately). When Ray AB arrives at point B, it refracts in the electrode, and the angle of refraction is determined by Equation [4.10]. The new position of the longitudinal component of the refracted wave in the electrode is given by

$$x_{BC} = x_B + (t - t_B)c_s \cos(\Theta + \Delta), \quad [4.15]$$

and

$$y_{BC} = y_B + (t - t_B)c_s \sin(\Theta + \Delta). \quad [4.16]$$

Ray BC reaches the surface or back of the electrode at the time given in Equation [4.13]. Time t_B is just the distance that the shock travels in air divided by the shock velocity, c_p . The propagation of the cylindrical wavefront through the electrode is plotted in Figure 4.9.

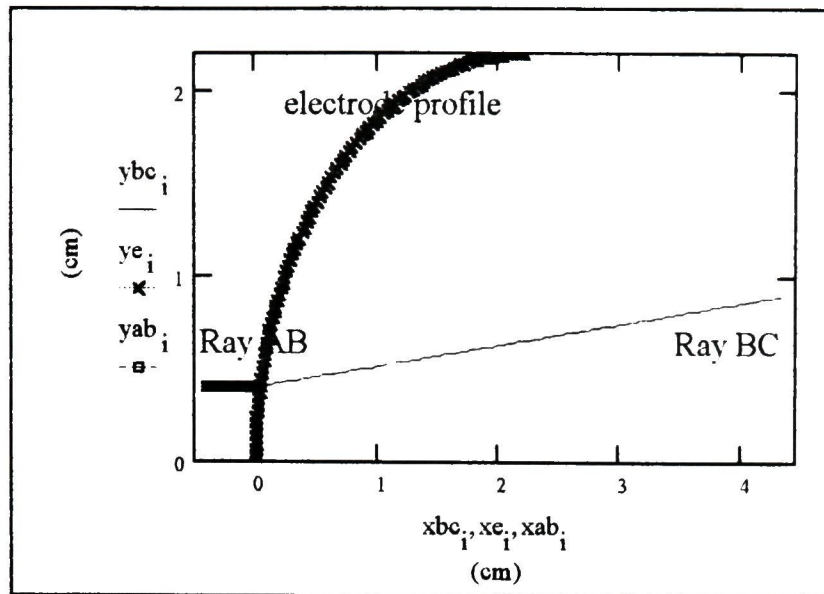


Figure 4.9 Propagation of a Cylindrical Shock Wavefront Through a Graphite Electrode for a Gap Spacing of 0.5"

If the arc radius is assumed to be constant for small changes in gap spacing, the propagation of the cylindrical wavefront through the electrode is not dependent on the gap distance. The experimental pressure measurements in Chapter 3 showed that the shock pressure was independent of gap spacing, which coincides with a cylindrical shock front rather than a spherical shock front.

4.3 PSPICE Analysis of Acoustic Transmission Lines

PSPICE is an electrical circuit analysis program. It can be used in this case because acoustic transmission lines behave similarly to electrical transmission lines. The electrode and delay bar are modeled as mismatched transmission lines, defined by their impedance and one-way transit time. Since acoustic pressure propagates through the acoustic transmission lines as voltage would through the electrical equivalent, the input voltage to the circuit is modeled after the shock wave pressure in Figure 4.4. This is done by using a piecewise linear voltage source in PSPICE. A voltage probe is placed in the middle of the ceramic line where the strain gage is in the actual system. A 0.001 Ω resistor at the end of the circuit simulates the low impedance of air at the free end of the ceramic bar. The PSPICE simulation circuit can be seen in Figure 4.10.

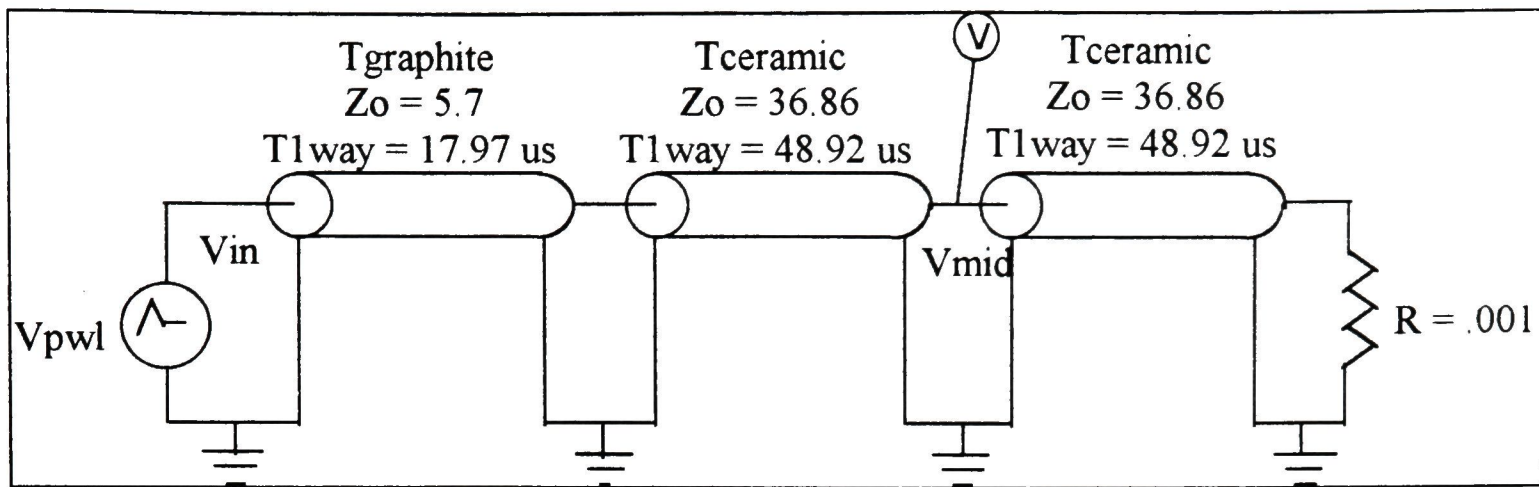


Figure 4.10 PSPICE Simulation Circuit

The PSPICE simulation of the input pressure and the strain gage output for a pressure pulse through the graphite electrode is shown in Figure 4.11. The upper graph is the maximum shock pressure from Figure 4.4 modeled as the input voltage, with one volt corresponding to 10^9 Pascal of pressure. The lower graph is the signal from the voltage probe at Vmid, which corresponds to the strain gage in the middle of the ceramic bar. Due to difficulties importing the Mathcad values directly into PSPICE, a separate text file was created with the shock pressure values and imported into PSPICE as a piecewise linear voltage source. The circuit behavior was simulated for the first 200 μs , which corresponds to the time frame of the experimental measurements. The voltage probe signal in Figure 4.11 may be compared to an experimental shot in Figure 4.12.

As expected, the simulation shows a delay time corresponding to the transit time of the graphite and ceramic bar. The reflections at approximately 100 μs , 140 μs , and 180 μs are from the portion of the original signal that is reflected back into the graphite. This signal bounces back from the electrode surface and travels to the ceramic boundary in 36 μs , the two-way transit time of the graphite. The reflection from the open end of the ceramic line occurs 100 μs after the initial pulse.

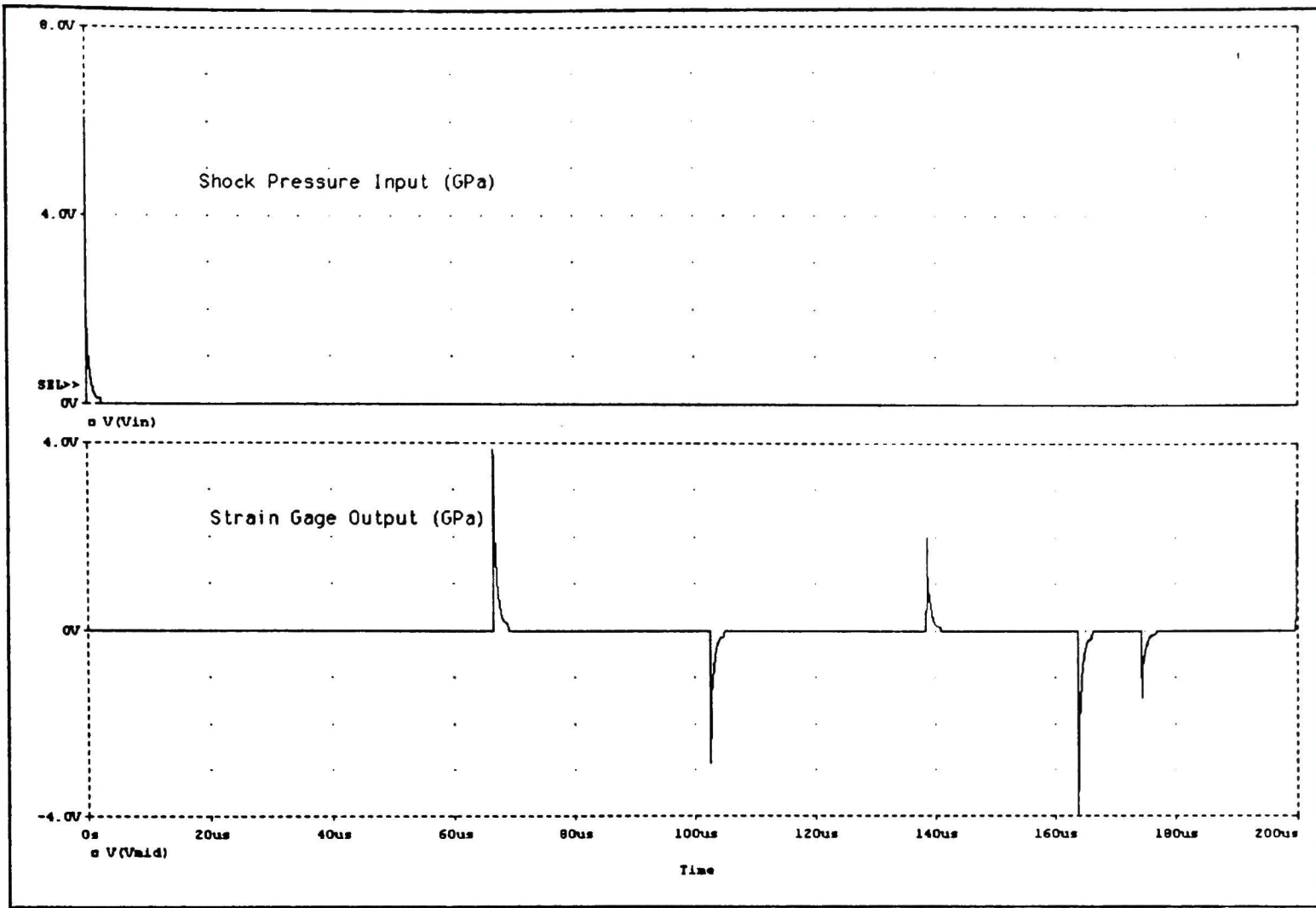


Figure 4.11 PSPICE Simulation of Pressure Input and Strain Gage Output

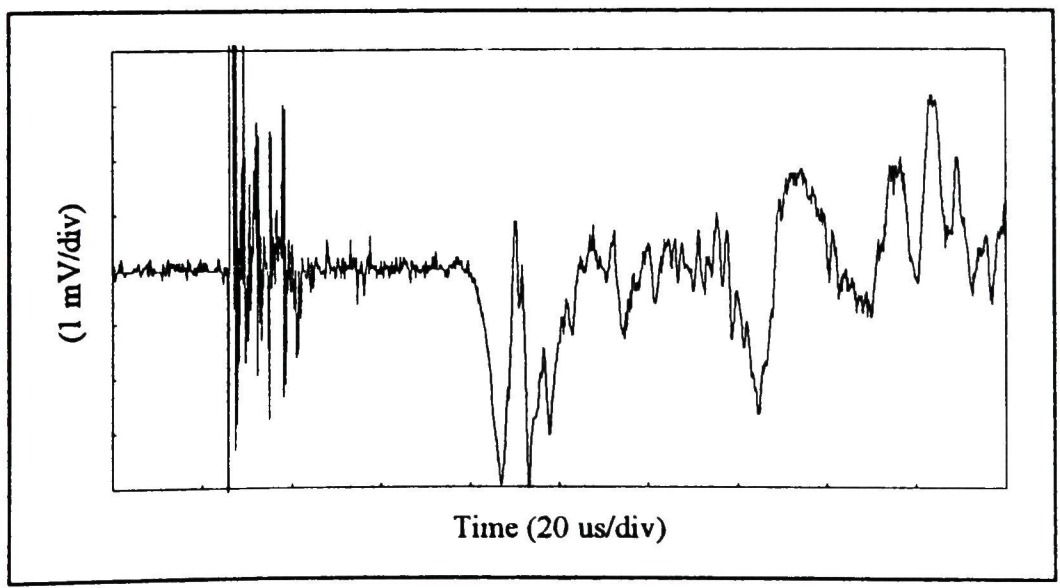


Figure 4.12 Comparative Experimental Shot

The PSPICE simulation and the experimental data are similar in several respects. The experimental shot has a time delay corresponding to the transit time of the graphite and ceramic, as does the simulation. In both the experimental result and the PSPICE simulation, there are multiple reflections due to the impedance mismatch at the

graphite/ceramic boundary and at the free end of the ceramic bar. However, due to nonideal conditions in the experimental setup, the pressure pulse that strikes the electrode tip is not accurately represented by the strain gage, as it is by the voltage probe in the PSPICE simulation. Unfortunately, the shock pulse may not be resolved from the experimental strain gage data because of the limited frequency response of the gage.

CHAPTER 5

CONCLUSIONS

The initial goal of this project was to determine the operating parameters that limited graphite electrode performance. An experimental setup was used to recreate the conditions under which electrode failure occurred at Physics International. At PI, it was theorized that the graphite would spall in a single shot if the di/dt exceeded 350 A/ns, independent of other parameters. The maximum di/dt achieved with this experiment was 460 A/ns and no electrode failure occurred.

When the electrode damage could not be repeated, the focus shifted to measuring the shock impact due to the high current arc on the electrode surface. Parameters such as charging voltage, inductance, gap spacing, and gas pressure were varied to measure the relative differences of the shock wave. Magnetic pulse shaping was included in the circuit to see if the delay in current affected the shock wave. Two different electrode materials, graphite and stainless steel, were used to see if the pressure propagation through the electrode was dependent on the type of material.

It was determined from the experimental measurements that increasing the energy had the greatest impact on the shock pressure magnitude. Table 3.4 showed that the pressure amplitude increases by a factor of 4, while the voltage increased by a factor of 1.83 and the energy by a factor of 3.38. The increase in peak pressure followed the increase in energy more so than the increase in voltage.

The measured pressure did not significantly change as the gap spacing increased and the energy was held constant. Although the plasma jet pressure is a significant factor for electrode erosion as the gap distance is decreased, it does not seem to be the dominant high pressure mechanism. Also, since the pressure measurements were unaffected by the gap spacing, it is likely that the shock wave is still expanding in a cylindrical mode, instead of a spherical one. Likewise, the shock pressure was unaffected by the ambient air pressure in the switch. Since the air pressure was many orders of magnitude lower than the shock pressure, it was not expected to have any effect.

Increasing the inductance decreased the peak current and slowed the ringing time period of the pulse. It is interesting to note that the amplitude of the pressure pulse was unaffected by the difference in current in the two measurements. It can be concluded that magnitude of the shock pressure is dependent on energy, and not peak current. A slight increase in the initial slope of the pressure pulse was detected as the inductance of the system was lowered. The difference was not significant enough to make a correlation

between the risetime of the shock pulse and the risetime of the current pulse. A larger difference in the inductance of the circuit may provide more insight.

Adding the ferrite lines for the magnetic pulse shaping delayed the current by as much as 70 ns. As expected, the amount of time delay decreased as the breakdown voltage increased. There is virtually no difference between the pressure shots taken with and without the magnetic delay lines. Neither the magnitude or waveform was affected. The magnetic delay was expected to have some sort of impact on the shock pressure wave, either by delaying the onset of the pressure pulse or reducing the amplitude of pulse. This reinforces the hypothesis that the shock wave was dependent on the energy and not the peak current or di/dt .

The comparison of pressure pulses in the graphite and stainless steel electrodes showed several differences. The stainless steel shot had a small pre-pulse and a steeper wavefront than the graphite shot. The graphite had two smaller pulses that immediately followed the initial pulse that the stainless steel did not have.

It should be restated at this point that the pressure measurements were relative. Due to the frequency response of the gage, the spherical geometry of the electrode, the material discontinuity between the electrode and ceramic delay bar, and dispersion, the actual shock pressure and magnitude could not be determined accurately. Although the experimental measurements gave an impression of which operating parameters significantly affect the shock pulse, the exact nature of the shock pressure interaction at the electrode surface is still unknown.

Theoretical modeling included a Mathcad analysis of the shock pressure in the switch, PSPICE simulation of the acoustic pulse propagation, and a Mathcad analysis of the reflection and refraction of the diverging wavefront through the electrode. The first Mathcad analysis showed that the shock pressure generated in the switch was three orders of magnitude higher than the magnetic pressure. In Chapter 2, it was shown that the arc radius was proportional to the double integral of the squared current. The expansion velocity was the derivative of the arc radius and was proportional to the quantity

$$u_1(t) \approx \left(\int I^2(t) dt \right)^{.5} \quad [5.1]$$

The shock pressure was proportional to the velocity squared; therefore, it was proportional to the energy. Likewise, the experimental shock measurements in Chapter 3 showed a strong dependence on energy.

The PSPICE simulations modeled the graphite and ceramic as transmission lines, and the shock wave pressure as a piecewise linear voltage source. The deviations due to the geometrical nature of the problem cannot be included in the simulation; however, the delay times and pulse lengths in the simulation corresponded to the measured data.

The wavefront propagation in the graphite and stainless steel electrodes was simulated in Mathcad. Since the shock wave in the material was assumed to be weak, it was treated as an acoustical wave. The propagation in the electrode was analyzed using the ray-tracing technique. For the analysis, Gracewski's model was modified to accommodate the geometry of the electrode. Due to the spherical geometry of the electrode tip, the shock pressure was refracted in the graphite. At the point of refraction, longitudinal and shear waves propagated normal and transverse to the direction of propagation.

From the modeling of the spherical wavefront propagation through the electrode in Chapter 4, it can be seen that the angle of refraction in graphite is highly dependent on the gap spacing between the electrodes. As the gap distance increased, the angle of propagation of the refracted wave with respect to the horizontal axis decreased. This angle will never completely drop to zero because there will always be a finite radius of curvature of the shock wave. The shock wave was not refracted as it transmitted through the stainless steel electrode, because the velocity of propagation of the shock pulse was nearly equal to the velocity of propagation in the stainless steel. If the shock pulse was modeled as a cylindrical wavefront, the propagation through the electrode was not dependent on gap spacing.

The electrode failure at Physics International occurred under conditions of high energy, high current and di/dt , and relatively short gap spacing. However, in this experiment, the graphite electrodes did not fail when subjected to a high current pulse that exceeded 350 A/ns. It was shown in the relative pressure measurements in Chapter 3 that the shock wave pressure that impacted the electrodes was dependent on energy, and not current or di/dt . It was also shown in Chapter 4 that shock pressure dominated the magnetic pressure due to the magnetic field.

The fact that the graphite electrode damage could not be duplicated probably stems from differences in the experiments at Texas Tech and Physics International. The biggest difference is the fact that PI was using a 100 kV, 18 kJ storage capacitor as opposed to the 60 kV, 5 kJ capacitor used at Tech. Although the current levels and risetimes of the two systems were comparable, the breakdown voltage and energy were not. Also, the trigger plane was removed from the Texas Tech experiment. There were probably some

other minor differences that we will never know about. It can be concluded that while high di/dt may contribute to the electrode failure, it is not the sole cause. It is entirely possible that the failure at PI was due to thermal pressure in the electrode tip. Although Joule heating in the electrode is negligible, heating due to the high temperatures associated with the arc is not. If the thermal energy is transferred to the electrode faster than the graphite can disperse the heat, the electrode may fracture. The rate of heating could very well be dependent on the di/dt of the electrical circuit. The theoretical analysis and experimental measurements of the transient electrode heat transfer would be an excellent topic for future research.

REFERENCES

- [1] Donaldson, A.L. and Kristiansen, M. "The Erosion Performance of Graphite Electrodes in High Current, High Coulomb Spark Gaps." 8th IEEE Pulsed Power Conference, 1991, pp. 874-877.
- [2] Engel, T. G.. "Insulator Degradation by High Current Discharges." Ph.D. Dissertation, Texas Tech University, 1990.
- [3] Braginskii, S.I. "Theory of the Development of a Spark Channel." Journal of Experimental and Theoretical Physics, Vol. 34, June 1958, pp. 1068 - 1074.
- [4] Engel, T.G., Kristiansen, M., and Krompholz, H. "Expansion of Hydrogen Arcs Driven by Oscillating Currents". IEEE Transactions of Plasma Science, Vol. 19, No. 5, Oct. 1991.
- [5] Donaldson, A.L. "Electrode Erosion in High Current, High Energy Transient Arcs." Ph.D. Dissertation, Texas Tech University, 1990.
- [6] Zeldovich, Y.B. and Raizer, Y.P. Physics of Shock Waves and High-Temperature Hydrodynamic Phenomena. New York, New York: Academic Press, 1966, p 636.
- [7] Haley, R.F. and Smy, P.R. "Electrically Induced Turbulence - the Short Duration Spark." Journal of Physics D, Vol. 22, February 1989, pp 258 - 265.
- [8] Akiyama, H., Kristiansen, M., Krompholz, H., and Maas, B. "Current - Voltage Characteristics of a High-Current Pulsed Discharge in Air." IEEE Transactions on Plasma Science, Vol. 16, No.2, April 1988, pp. 312 - 316.
- [9] Lehr, F. Mark and Kristiansen, M. "Electrode Erosion from High Current Moving Arcs." IEEE Transactions on Plasma Science, Vol. 17, No. 5, October 1989, pp. 811 - 817.
- [10] Donaldson, A.L., Kristiansen, M., Watson, A., Zinsmeyer, K., and Kristiansen, E. "Electrode Erosion in High Current, High Energy Transient Arcs." IEEE Transactions on Magnetics, Vol MAG-22, No. 6, Nov. 1986. pp. 1441-1147.
- [11] Welty, J.R., Wicks, C.E., and Wilson, R.E. Fundamentals of Momentum, Heat, and Mass Transfer. New York, New York: Wiley Publishers, 1976, pp 247.
- [12] Engel, T.G. "Selection Criteria for Insulator Materials in High Current Arc Environments." Master's Thesis, Texas Tech University, 1987, pp. 8 - 9.

- [13] Rinehart, J.S. and Pearson, J. Behavior of Metals Under Impulsive Loads. Cleveland, Ohio: American Society for Metals, 1954. p. 52.
- [14] Duffy, T.S. and Ahrens, T.J. "Dynamic Response of Molybdenum Shock Compressed at 1400 °C." Journal of Applied Physics, Vol. 76, No. 2, July 1994, pp. 835 - 842.
- [15] Stephens, R.W.B. and Bate, A.E. Acoustics and Vibrational Physics. London: Edward Arnold Ltd., 1966, p 411.
- [16] Kolsky, H. Stress Waves in Solids. London: Oxford University Press, 1953, p 10.
- [17] Zhong, P., Chuong, C.J., and Preminger, G.M. "Propagation of Shock Waves in Elastic Solids Caused by Cavitation Microjet Impact. Part II." Journal of Acoustical Society of America, Vol 94, No.1, July 1993, pp. 29 -36.
- [18] Gracewski, S.M., Dahake, G., Ding, Z. "Internal Stress Wave Measurements in Solids Subjected to Lithotriper Pulses." Journal of the Acoustical Society of America, Vol 94, No 2, August 1993. pp. 652-661.
- [19] Affinito, D., Bar-Avraham, E., and Fisher, A. "Design and Structure of an Extended Life High Current Spark Gap." UCI Technical Report #79-13. February 1979.
- [20] CRC Handbook of Chemistry and Physics, 72nd Edition, Boca Raton, Florida: CRC Press, 1991 - 1992. pp 4-7.
- [21] POCO Graphite Data Sheet, POCO Graphite, Decatur, Texas. November 1993.
- [22] Davids, Norman (ed.). International Symposium on Stress Wave Propagation in Materials. New York, New York: Interscience Publishers, Inc, 1960, pp 247 - 270.
- [23] Advanced Pulsed Power Program. Technical Report, Physics International Company, San Leandro, California, June 1989.
- [24] Link Pulser Operations, 1985 - 1989. Technical Report, Physics International Company, San Leandro, California, February 1990.
- [25] Naff, Tom. Personal correspondence. Physics International, San Leandro, California, 1992.

- [26] Huddleston, Richard H. Plasma Diagnostic Techniques. New York, New York: Academic Press, 1965, pp. 7 - 11.
- [27] Asay, J.R. and Barker, L.M. "Interferometric Measurement of Shock-Induced Internal Particle Velocity and Spatial Variations of Particle Velocity." Journal of Applied Physics, Vol. 45, 1974, pp 2540 - .
- [28] Kanel, G.I., Razorenov, S.V., Utkin, A.V., Fortov, V.E., Baumung, K., Karow, H.U., and Rusch, D. "Spall Strength of Molybdenum Single Crystals." Journal of Applied Physics, Vol. 74, No. 12, December 1993, pp. 7162 - 7165.
- [29] Ueda, K. and Umeda, A. "Characterization of Shock Accelerometers Usng Davies Bar and Strain Gages." Experimental Mechanics, Vol. 33, September, 1993, pp 228 - 233.
- [30] Ceramic Data Sheet, Coors Ceramics Company, Golden, Colorado. December 1994.
- [31] Lexan Properties Guide, GE Plastics, Pittsfield, Maryland. December 1994.
- [32] Black, S.E. Nonlinear Magnetic Switches for Pulse Generation. Master' Thesis, Texas Tech University, 1980.
- [33] Levy, S. "Spark Gap Studies," U.S. Army Electronics Research and Development Laboratories, Fort Monmouth, New Jersey, 1964.
- [34] Dougal, R.A., Volakakis, G.D., and Abdalla, M.D. "Magnetically Delayed Vacuum Switching." 6th IEEE Pulsed Power Conference, 1987.
- [35] McDuff, G. and Rust, K. "Life Extension of Thyratrons in Short-Pulse Circuits with Use of Saturable Magnetic Switches." 19th IEEE Power Modulator Symposium, 1990.
- [36] Zentler, J.M. "Magnetic Switch Modeling," Microwave and Pulsed Power, Thrust Area Report, 1990, pp. 6-1 - 6-6.

APPENDIX

Spherical Stress Propagation in Graphite Electrode

dimensions are in cm

$a = 2.2$ electrode radius

$L = .3175$ distance between shock focal point and electrode surface,
equals half the gap spacing

$x_b = 0$

Coordinates of Position B

$y_b = .225$

$$\Theta_1 := \text{atan}\left[\frac{y_b}{(L + x_b)}\right]$$

$$\Theta_{1d} := \Theta_1 \cdot \left(\frac{180}{\pi}\right)$$

$$\Delta\Theta := \text{atan}\left[\frac{y_b}{(a - x_b)}\right]$$

$$\Theta := \Theta_1 + \Delta\Theta$$

$$\Theta_d := \Theta \cdot \left(\frac{180}{\pi}\right)$$

$c_l = 500000$ average velocity of shock wave in cm/s

$c_{gl} = 318000$ longitudinal velocity of graphite in cm/s

$$\delta := \text{asin}\left(\frac{c_{gl}}{c_l} \cdot \sin(\Theta)\right) - \Theta$$

$\Theta_{1d} = 35.324$ degrees

$$\delta_d := \delta \cdot \left(\frac{180}{\pi}\right)$$

$\Theta_d = 41.163$ degrees

$\delta_d = -16.416$ degrees

Time factors

$$t_b := \frac{L + x_b}{c_l \cdot \cos(\Theta_1)}$$

$$t_c := \frac{2.2 - y_b}{c_{gl} \sin(\Theta + \delta)}$$

$$t_b = 7.783 \cdot 10^{-7}$$

$$t_c = 1.484 \cdot 10^{-5}$$

$$i := 0..100$$

$$j_i := i \cdot \frac{tc}{100}$$

$$x_{bc_i} := x_b + (j_i) \cdot cgl \cdot \cos(\Theta 1 + \delta)$$

Position of Ray BC

$$y_{bc_i} := y_b + (j_i) \cdot cgl \cdot \sin(\Theta 1 + \delta)$$

$$x_c := x_{bc_{100}} \quad y_c := y_{bc_{100}}$$

Coordinates of Position C

$$\gamma := \text{atan} \left[\left[\frac{x_{bc_{100}} - x_{bc_0}}{(y_{bc_{100}} - y_{bc_0})} \right] \right]$$

$$\gamma_d := \gamma \cdot \left(\frac{180}{\pi} \right)$$

$\gamma_d = 71.092$ degrees

$$td := \frac{y_{bc_{100}} - y_{bc_0}}{cgl \cdot \sin \left(\frac{\pi}{2} - \gamma \right)}$$

$$td = 1.484 \cdot 10^{-5}$$

$$l_i := tc + i \cdot \frac{td}{100}$$

$$x_{cd_i} := x_c + (l_i - tc) \cdot cgl \cdot \sin(\gamma)$$

Position of Ray

$$y_{cd_i} := y_c - (l_i - tc) \cdot cgl \cdot \cos(\gamma)$$

CD

$$x_{ab_i} := x_{bc_0} - \frac{i}{100} \cdot L$$

Position of Ray AB

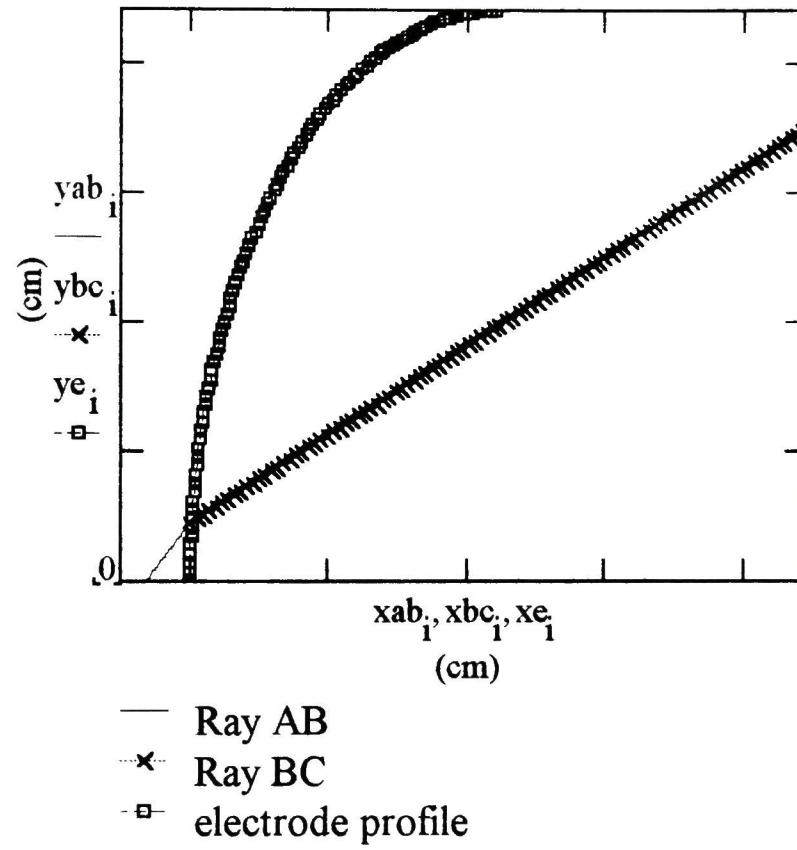
$$y_{ab_i} := y_b + x_{ab_i} \cdot \tan(\Theta 1)$$

Electrode Profile

$$\Phi_i = \left(.01 \cdot \frac{\pi}{2} \right) \cdot i$$

$$xe_i = 2.2 - a \cdot \cos(\Phi_i)$$

$$ye_i = a \cdot \sin(\Phi_i)$$



Cylindrical Stress Propagation in Graphite Electrode

dimensions are in cm

$a = 2.2$ electrode radius

$r = .4$ arc radius

$x_b := 0$

Coordinates of Position B

$y_b := r$

$$\Theta := \text{atan}\left(\frac{y_b}{a}\right)$$

$$\Theta_d := \Theta \cdot \left(\frac{180}{\pi}\right)$$

$c_l := 500000$ average velocity of shock wave in cm/s

$c_{gl} := 318000$ longitudinal velocity of graphite in cm/s

$$\delta := \text{asin}\left(\frac{c_{gl}}{c_l} \cdot \sin(\Theta)\right) - \Theta$$

$$\delta_d := \delta \cdot \left(\frac{180}{\pi}\right)$$

$\Theta_d = 10.305$ degrees

$\delta_d = -3.772$ degrees

Time factors

$$t_b := \frac{r}{c_l} \quad t_c := \frac{2 \cdot a}{c_{gl}} \cdot \cos(\Theta + \delta)$$

$$t_b = 8 \cdot 10^{-7} \quad t_c = 1.375 \cdot 10^{-5}$$

$i := 0..100$

$$j_i := i \cdot \frac{t_c}{100}$$

$$x_{bc_1} := x_b + (j_1) \cdot cgl \cdot \cos(\Theta + \delta)$$

$$y_{bc_1} := y_b + (j_1) \cdot cgl \cdot \sin(\Theta + \delta)$$

Position of Ray BC

$$x_c := x_{bc_{100}} \quad y_c := y_{bc_{100}}$$

Coordinates of Position C

$$\gamma := \text{atan} \left[\left[\frac{x_{bc_{100}} - x_{bc_0}}{(y_{bc_{100}} - y_{bc_0})} \right] \right]$$

$$\gamma d := \gamma \cdot \left(\frac{180}{\pi} \right)$$

$$\gamma d = 83.467 \quad \text{degrees}$$

$$td := \frac{y_{bc_{100}} - y_{bc_0}}{cgl \cdot \sin\left(\frac{\pi}{2} - \gamma\right)}$$

$$td = 1.375 \cdot 10^{-5}$$

$$l_1 := tc + i \cdot \frac{td}{100}$$

$$x_{cd_1} := x_c + (l_1 - tc) \cdot cgl \cdot \sin(\gamma)$$

$$y_{cd_1} := y_c - (l_1 - tc) \cdot cgl \cdot \cos(\gamma)$$

Position of Ray
CD

$$x_{ab_1} := x_{bc_0} - \frac{i}{100} \cdot r$$

Position of Ray AB

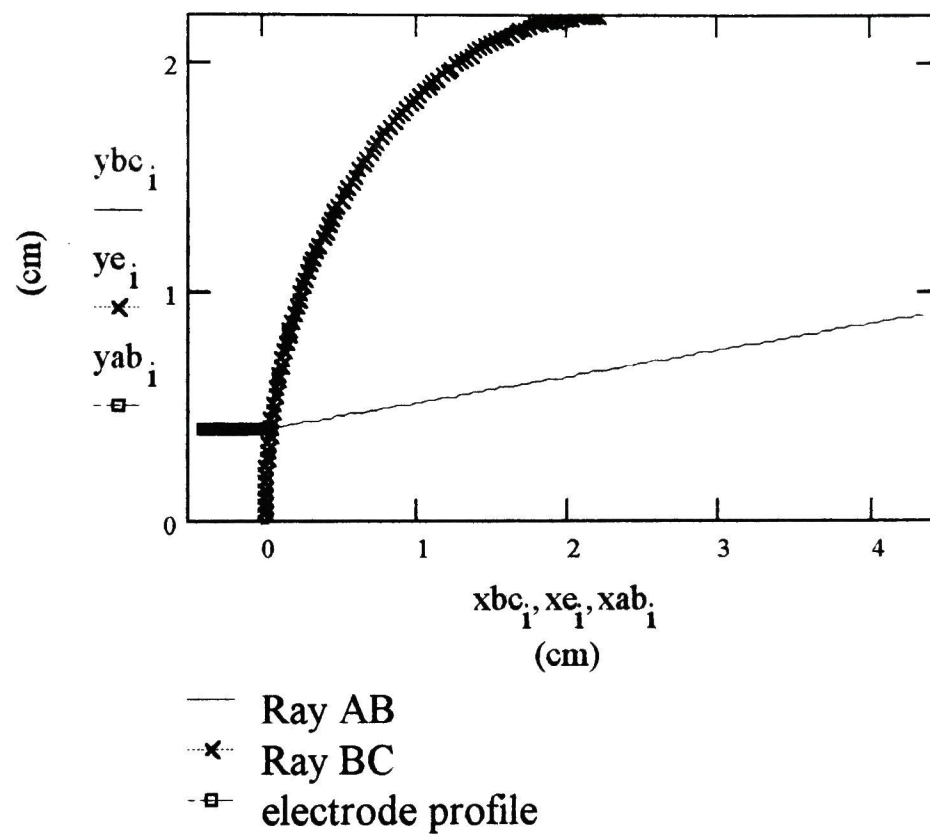
$$y_{ab_1} := r$$

Electrode Profile

$$\Phi_i = \left(.01 \cdot \frac{\pi}{2} \right) \cdot i$$

$$x_{e_i} = 2.2 - a \cdot \cos(\Phi_i)$$

$$y_{e_i} = a \cdot \sin(\Phi_i)$$



Arc radius, velocity, and shock pressure analysis
 Michele Wofford
 6/5/95

Arc Radius Constants

$\gamma := \frac{7}{5}$ ratio of specific heat for air (diatomic gas)

$K := 2 \cdot \frac{\gamma + 1}{(\gamma - 1)^2}$ resistance coefficient

$K = 30$

$\rho_0 := 1.29$ undisturbed density of air (kg/m³)

$\sigma := 30000$ normal arc conductivity (Qm)⁻¹

$c := \left(\frac{9}{\pi^2 \cdot \rho_0 \cdot K \cdot \sigma} \right)^{\frac{1}{6}}$ integration constant

$c = 0.096$

Circuit Parameters

$L := 69 \cdot 10^{-9}$ inductance

$C := 2.85 \cdot 10^{-6}$ capacitance

$R := .030$ resistance

$\alpha := \frac{R}{2L}$ damping factor

$\alpha = 2.174 \cdot 10^5$

$w := \frac{1}{\sqrt{LC}}$ frequency (rad/s)

$w = 2.255 \cdot 10^6$

$Z := \sqrt{\frac{L}{C}}$ impedance

$Z = 0.156$

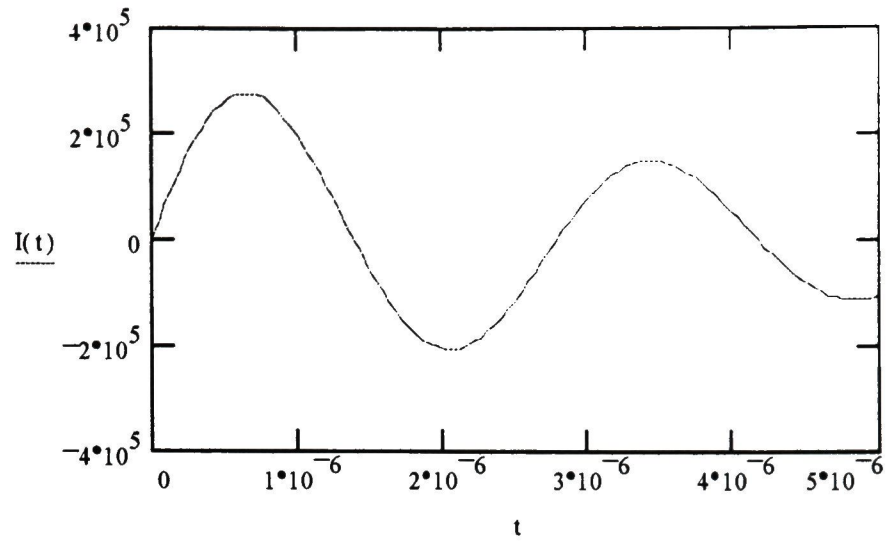
$V := 50000$ maximum charging voltage (V)

$t := 2 \cdot 10^{-9}, 50 \cdot 10^{-9} .. 5 \cdot 10^{-6}$ time period for one-half oscillation

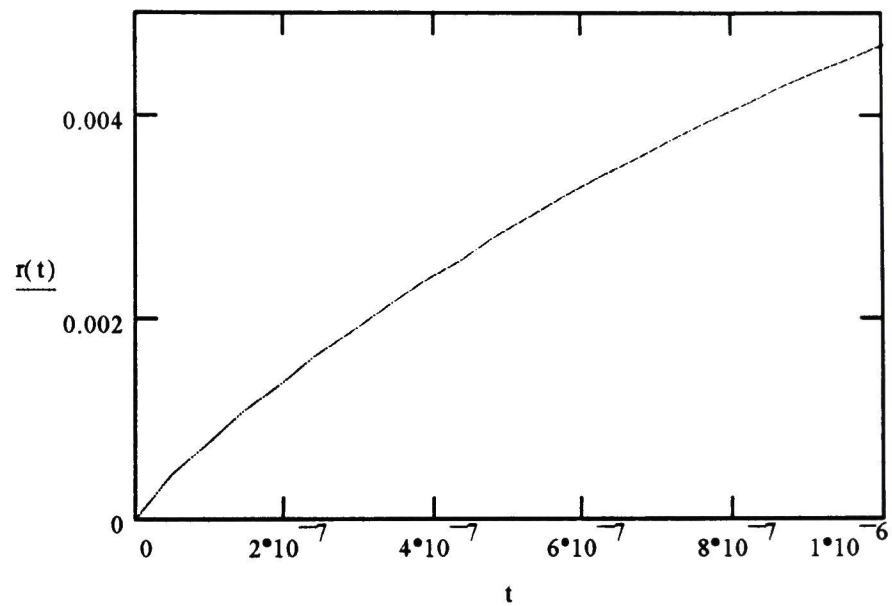
$I(t) := \frac{V}{Z} \sin(w \cdot t) \cdot e^{-\alpha \cdot t}$ circuit current

$r(t) := c \cdot \left[\int_0^t \left(\int_0^t I(t)^2 dt \right)^{.5} dt \right]^{.333}$ arc radius, as defined by Equation 13, Ref II.

Output Current for 50 kV,
5kJ System



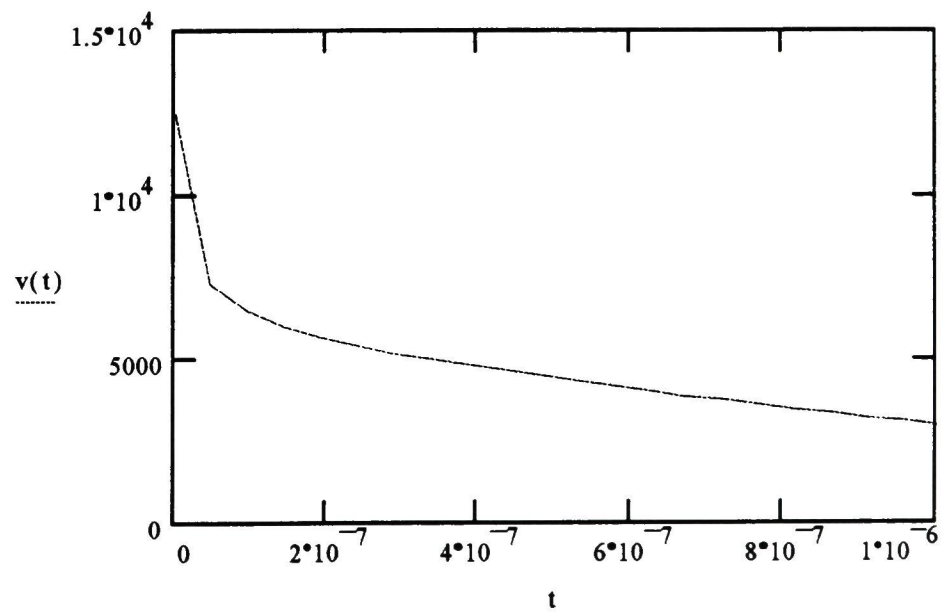
Arc Radius



$$v(t) := \frac{d}{dt}r(t)$$

arc channel expansion velocity = shock velocity

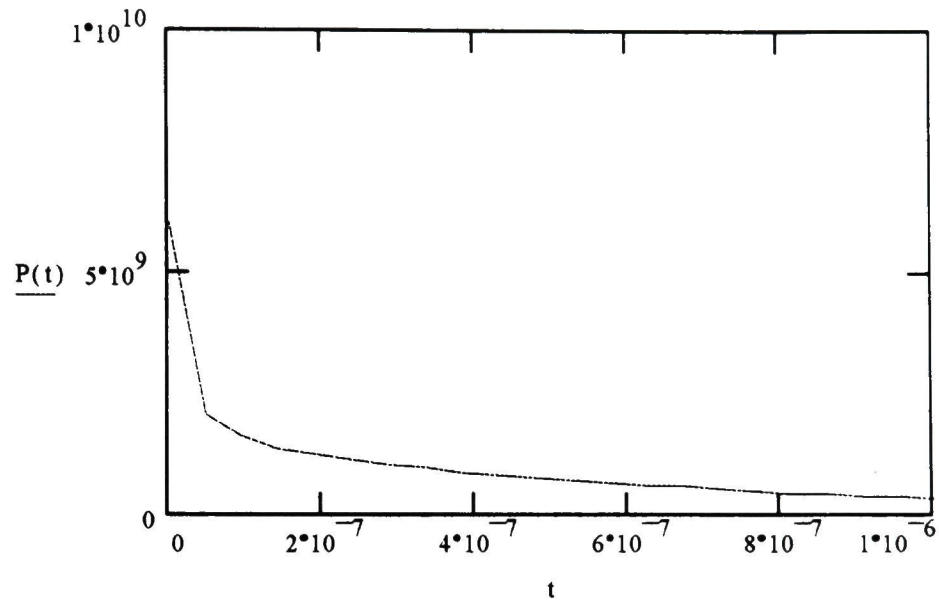
Arc Expansion Velocity



Shock Pressure Calculation

$$P(t) = K \cdot \rho_0 \cdot v(t)^2$$

Shock Pressure



Initial Velocity Calculation based on dI/dt from Equation 10, Ref II-1

$$L := 69 \cdot 10^{-9} \quad \text{circuit inductance}$$

$$A := .16 \quad \text{gas constant}$$

$$v_0 := A \cdot \left(\frac{V}{L} \right)^{\frac{2}{5}}$$

$$v_0 = 8.875 \cdot 10^3 \quad \text{m/s}$$

Arc Pressure Calculations based on Equation 8b, Ref II-1

Based on Initial Velocity

$$P_1 := K \cdot \rho_0 \cdot v_0^2$$

$$P_1 = 3.049 \cdot 10^9 \quad \text{Pa}$$

$$P_{1\text{atm}} := \frac{P_1}{1.013 \cdot 10^5}$$

$$P_{1\text{atm}} = 3.009 \cdot 10^4 \quad \text{atm}$$